Advances in performance and automation of a single ytterbium ion optical clock

Alexandra Tofful

Imperial College London
Department of Physics

Supervisors: Dr. Rachel M. Godun & Prof. Richard C. Thompson

Thesis submitted in Partial Fulfillment of the Requirements for the Degree of Doctor of Philosophy

Abstract

While the SI second is currently defined in terms of a microwave transition frequency in caesium, atomic clocks based on an optical transition are currently outperforming caesium clocks by up to two orders of magnitude. In order to fully exploit the potential accuracy achievable by optical clocks, the SI second needs to be redefined in terms of an optical frequency standard. The $^{171}\mathrm{Yb}^{+}$ ion is an excellent candidate thanks to the extremely narrow linewidth of its electric octupole (E3) transition and its particular insensitivity to external perturbations.

This thesis is focused on the ytterbium ion optical clock at the National Physical Laboratory (NPL), consisting of a single $^{171}\mathrm{Yb}^{+}$ ion trapped in a radio frequency (RF) Paul trap and probed by ultrastable 467-nm light to excite the E3 transition. Improved measurement methods were developed for the evaluation of several systematic frequency shifts. In particular, the electric quadrupole shift, which used to be the leading source of uncertainty, can now be directly measured with an accuracy in the low parts in 10^{18}.

A great focus was put on the automation of several aspects of the experiment. Because all optical clocks generally require a lot of maintenance and attention during their operation, many experimental routines were automated in order to minimise the requirement for human intervention. Furthermore, the analysis of almost all systematic shifts was automated, requiring minimal manual input so that shifts could be evaluated on the fly. Finally, a generalised framework was developed for the automatic evaluation of the absolute frequency of the optical clock via the International Atomic Time (TAI).

In order to increase the confidence in the level of performance of the ytterbium ion optical clock, international clock comparison campaigns are regularly carried out. Between 2019 and 2022, several results were produced: two absolute frequency measurements via TAI with an uncertainty at the 1×10^{-15} level; two local frequency ratio measurements between $^{171}\mathrm{Yb}^{+}$ (E3) and $^{87}\mathrm{Sr}$ with an uncertainty in the low parts in 10^{17}; three uncertainty budgets at the parts in 10^{18} level; and one measurement of the ratio of the octupole and quadrupole optical clock transitions in $^{171}\mathrm{Yb}^{+}$ with an uncertainty of 1.5×10^{-16}. All of these results are shown to be consistent with each other and in good agreement with the literature. Furthermore, a prototype optically-steered time scale was successfully demonstrated for the first time at NPL with the contribution of both the $^{171}\mathrm{Yb}^{+}$ and $^{87}\mathrm{Sr}$ optical clocks.

Declaration

I declare that all the material in this thesis is my own, unless otherwise stated and referenced.

Acknowledgements

First of all, I am extremely grateful to my NPL supervisor Rachel Godun − your exceptional guidance and continuous support throughout the years has allowed my PhD experience to be really enjoyable. A big acknowledgement also goes to Richard Thompson, my Imperial College supervisor − you have regularly provided me with useful perspective and valuable feedback. I must also thank you both for being such excellent proofreaders!

Thank you to my colleagues at NPL that I worked together with on the project: to Charles, for spreading your passion for innovation and for teaching me your programming practices; to Billy, for inspiring creative solutions to intricate problems and for helping me keep the lab tidy; to Adam, for many stimulating discussions and brain teasers; to Anne, for your contagious positivity. Thank you to everyone else at NPL who I have collaborated with.

Thank you to my CQD cohort at Imperial, and in particular Dominika, Nick and Jacopo, for sharing our PhD journey together and for all the fun we have had in countless board games sessions. Thank you also to Miranda for being the most helpful and efficient admin I have ever dealt with.

Thank you to my parents for helping me pursue my dreams and for supporting me every step of the way. I would not be doing what I am doing if it were not for you. And finally, thank you Tsetsi, for being my constant source of motivation, for always being there for me, and for filling my life with happiness and excitement.

Contents

List of Figures

List of Tables

List of Acronyms

AC	alternating current
AOM	acousto-optic modulator
ARTIQ	Advanced Real-Time Infrastructure for Quantum physics
BBR	black-body radiation
BIPM	International Bureau of Weights and Measures
BS	beam-splitter
CCTF	Consultative Committee for Time and Frequency
CIPM	International Committee for Weights and Measures
CTE	coefficient of thermal expansion
DC	direct current
DDS	direct digital synthesis
DL	diode laser
E2	electric quadrupole transition
E3	electric octupole transition
EAL	Échelle Atomique Libre / Free Atomic Time
ECDL	external-cavity diode laser
EMCCD	electron-multiplying charge-coupled device
EOM	electro-optic modulator
FWHM	full-width half-maximum
FPGA	field-programmable gate array
GNSS	Global Navigation Satellite System
GUI	graphical user interface
HCI	highly-charged ion
H, U, D	Horizontal, Up, Down (beams)
IERS	International Earth Rotation and Reference Systems Service

INRIM	Istituto Nazionale di Ricerca Metrologica
IR	infrared
LO	local oscillator
MJD	Modified Julian Date
MOT	magneto-optical trap
NDF	neutral-density filter
NEG	non-evaporable getter
NMI	national measurement/metrology institute
NMIJ	National Metrology Institute of Japan
NPL	National Physical Laboratory
OOL	out of loop
PBS	polarising beam-splitter
PCF	photonic-crystal fibre
PDH	Pound-Drever-Hall
PhD	Doctor of Philosophy
PID	Proportional Integral Differential
PM	polarisation-maintaining
PMT	photomultiplier tube
PSD	power spectral density
PTB	Physikalisch-Technische Bundesanstalt
QPN	Quantum Projection Noise
RF	radio frequency
RMS	root mean square
SI	International System of Units
SHG	second harmonic generation
SNR	signal-to-noise ratio
SRS	Stanford Research Systems
SYRTE	Systèmes de Référence Temps-Espace

TA	tapered amplifier
TAI	International Atomic Time
TT	Terrestrial Time
TTL	transistor-transistor logic
UHV	ultra-high vacuum
ULE	ultra-low expansivity
UMK	Uniwersytet Mikołaja Kopernika / Nicolaus Copernicus University
UTC	Coordinated Universal Time
UV	ultraviolet

1 Introduction

For centuries, the second was measured as a fraction of the time it takes the Earth to make a full rotation about its own axis. In 1884, the definition of the second as 1/86,400 of a mean solar day was adopted internationally as the unit of time. Only in the 1950s was it recognised that the revolution of the Earth around the sun was a more stable reference than the rotation of the Earth, leading to a new definition of the second in terms of a fraction of the solar year.

In 1955, Louis Essen and John Parry developed at the National Physical Laboratory (NPL) the world's first accurate atomic clock based on the interrogation of a thermal beam of caesium atoms [1]. The advantages of using an atomic transition as a frequency standard soon became clear, leading to a redefinition of the second in 1967 within the International System of Units (SI) as "the duration of 9,192,631,770 periods of the radiation corresponding to the transition between the two hyperfine levels of the ground state of the caesium-133 atom" [2].

Over the next few decades, advancements in laser cooling and atom trapping played an important role in the progress of atomic clock technologies, leading to an improvement in the accuracy of the frequency measurement by several orders of magnitude. This progress was also aided by the development of caesium fountain clocks [3, 4], in which a thermal vapour of atoms is captured and cooled down to a dense cloud, allowing for a longer interrogation time and also better control over the systematic offsets.

The advent of these new technologies inspired in the 1970s the suggestion of optical clocks, based on the spectroscopy of a narrow optical transition in a trapped ion [5]. Since then, the development of optical clocks has progressed at a much faster pace than caesium microwave clocks, and they have started outperforming caesium in the level of systematic uncertainty in the frequency measurement (see Fig. 1.1). The lowest fractional systematic

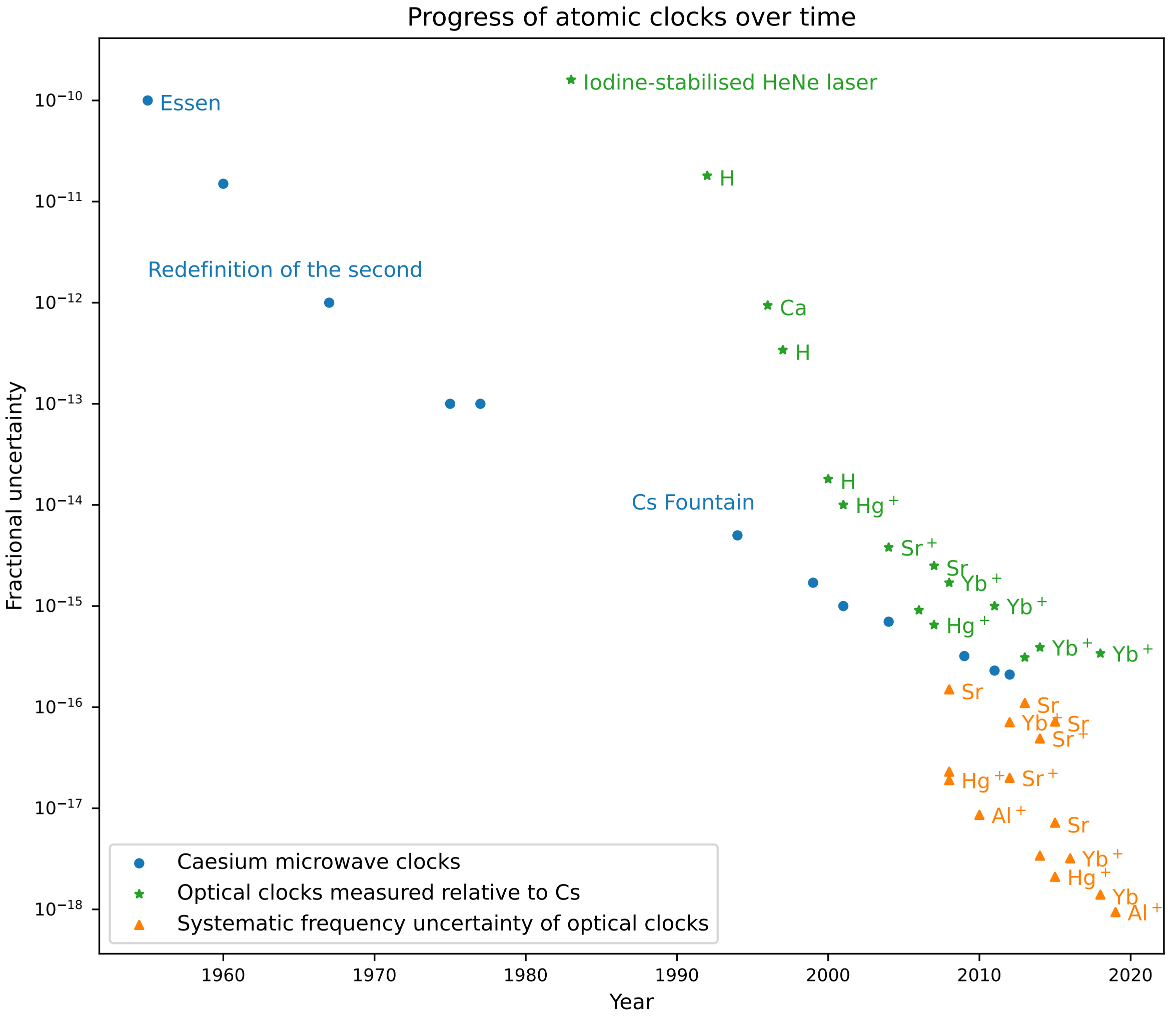

Figure 1.1: Progress over the years of the development of atomic clocks in the microwave and optical range.

uncertainty on an optical frequency has been recorded to be at the level of 9×10^{-19} [6], which is more than two orders of magnitude lower than the best caesium clock.

1.1 Principles of atomic clocks

An atomic clock is made up of three fundamental components, namely an atomic reference, a local oscillator and a frequency counter. A stable frequency *reference* is provided by the transition between two energy levels in an atom, which occurs at a specific frequency ν_0 that is constant in nature. The advantage of building a device upon an atomic frequency reference is that all atoms of the same species are identical, meaning that such a device would be perfectly reproducible: all atomic clocks based on the same atomic transition would tick at the same exact frequency in ideal conditions.

In order to produce a measurable frequency, a local *oscillator* is employed to probe the atom at a frequency ν, which is steered to match the reference transition frequency ν_0 via a feedback loop. Finally, the frequency of the oscillator is measured by a *counter*, which evaluates the "ticking" rate of the clock. Whereas the frequency of a microwave transition can be measured electronically, this is not appropriate for the measurement of optical frequencies, as these oscillations are too fast to be resolved by an electronic device. This challenge was overcome with the invention of femtosecond optical frequency combs (see section 1.3.3).

Atomic clocks can be distinguished in two categories: in an *active* clock, the measured signal comes directly from the radiation of the atomic reference, meaning that the reference and the oscillator are combined. Hydrogen masers, which are typically used at the basis of many local time scales, are an example of an active clock. In *passive* clocks, the atomic reference is probed by a separate oscillator, which is externally controlled to match the frequency of the reference. This is at the basis of the most accurate frequency standards.

1.2 Accuracy and stability of optical clocks

In order to characterise the performance of an atomic clock, it is important to distinguish two sources of measurement noise: systematic effects and statistical noise. Optical clocks carry an improvement in the systematic uncertainty that can be achieved. The various environmental perturbations and relativistic effects that the atom experiences cause a shift in the transition frequency. For optical clocks, the atom's energy levels are separated by a frequency gap in the optical range, meaning that the lower fractional effect of the systematic shifts would lead to a higher accuracy in the measurement [7]. On the other hand, the most significant improvement that sets optical clocks apart from any other type of atomic clock is the increased frequency stability, leading to lower statistical noise.

1.2.1 Allan variance

The Allan variance [8] is the most basic measure of frequency stability, which assesses the level of fractional frequency fluctuations caused by statistical noise in the clock system. The Allan variance is defined as:

$$\sigma_y^2(\tau) = \frac{1}{2(M-1)} \sum_{i=1}^{M-1} \left(y_{i+1} - y_i\right)^2 \ , \tag{1.1}$$

where y_i is the i^{th} fractional frequency out of M values averaged over a time period τ.

The overlapping Allan variance, defined in Eq. (1.2), is the most commonly used form of the normal Allan variance, as it gives a higher confidence in the estimate of the frequency stability by considering overlapping samples [9].

$$\sigma_y^2(\tau) = \frac{1}{2m^2(M-2m+1)} \sum_{j=1}^{M-2m+1} \left[\sum_{i=j}^{j+m-1} \left(y_{i+m} - y_i\right)^2 \right] \ , \tag{1.2}$$

where m represents the averaging factor, and $\tau = m\tau_0$, where τ_0 is the basic measurement interval. The resulting fractional frequency instability is typically reported as the square root of $\sigma_y^2(\tau)$, i.e. the Allan deviation. From the slope of the Allan deviation in a log-log plot, it is possible to identify the type of noise source affecting the system over time, which could be for example white noise, flicker noise, or random walk.

1.2.2 Quantum projection noise

For an atomic clock, the statistical noise is limited by the quantum projection noise (QPN) [10], which is a form of white frequency noise caused by the random nature of the wavefunction collapse (*projection* of the state vector) onto the measured energy state. The QPN-limited stability is given by:

$$\sigma_y(\tau) = \frac{1}{K}\,\frac{1}{\mathrm{SNR}}\,\frac{\Delta\nu}{\nu_0}\sqrt{\frac{t_m}{\tau}}\,. \tag{1.3}$$

In this equation, K is a constant of order unity, SNR is the signal-to-noise ratio, $\Delta\nu$ is the linewidth of the transition, ν_0 is the unperturbed transition frequency, $t_m = t_p + t_d$ is the duration of a single clock cycle, including both the probe time and the dead time, and τ is the total averaging time of the measurement. From the equation, it is clear that a high ν_0 is desirable for achieving low instability. In fact, the ratio $\nu_0/\Delta\nu$ represents the quality factor Q of the clock, and it is several orders of magnitude larger when ν_0 is an optical frequency as opposed to a microwave frequency.

The signal-to-noise ratio (SNR) is given by the following equation:

$$\mathrm{SNR} = \frac{\sqrt{N}p}{\sqrt{p(1-p)}}\,, \tag{1.4}$$

where N is the number of atoms in the system, and p is the probability of excitation of the transition at the probe frequency. Fig. 1.2 shows an example of a Rabi resonance and illustrates the meaning of the parameters that make up Eq. (1.3). The factor K is calculated from the gradient of the peak at the full width at half maximum (FWHM). In the case of Rabi spectroscopy, $K \approx \pi/2$.

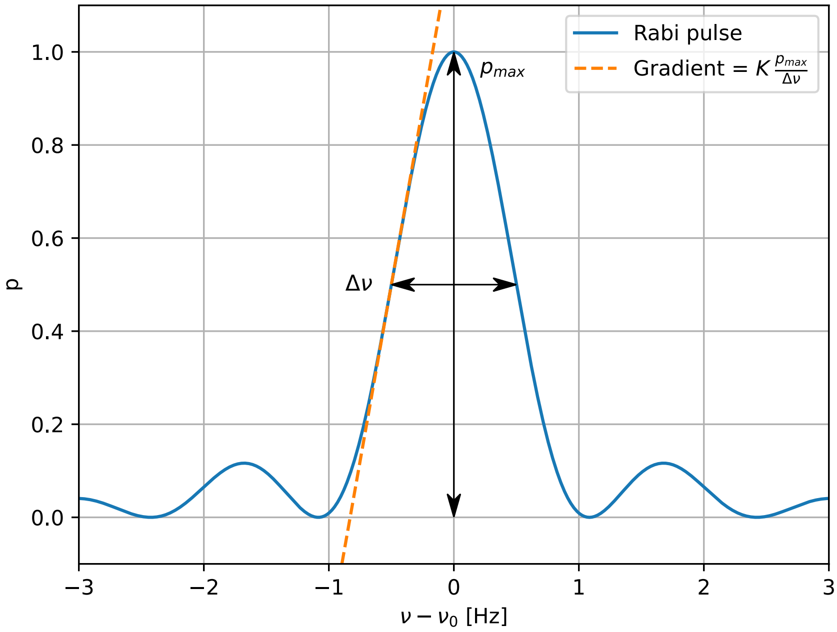

Figure 1.2: Plot of a simulated Rabi line shape as a function of the frequency detuning from the line centre.

1.3 Building blocks of optical clocks

To draw a parallel with the atomic clock components described in section 1.1, it will now be considered in more detail what these components are in optical clocks.

1.3.1 Reference: optical transition

At the basis of an optical clock lies an atomic hyperfine transition in the optical frequency range. Some transitions between hyperfine levels are forbidden by angular momentum selection rules. “Forbidden” in this case actually means electric-dipole forbidden, meaning that the transitions can still be driven, but they have a significantly narrower linewidth. This is an excellent characteristic for an optical clock, since the narrower the linewidth the higher the quality factor Q of the clock. Most ion optical clocks are based on quadrupole

(E2) transitions, with the ytterbium ion being the only frequency standard known to offer also an octupole (E3) transition.

The natural linewidth of the transition is directly related to the lifetime of the excited state. In order to increase the Q factor, it is therefore important to select an atomic reference whose excited clock state lifetime is relatively long. However, the effective linewidth of the transition depends on the time spent probing it. The excitation probability for Rabi spectroscopy is generally given by [11]:

$$p = \frac{\Omega_0^2}{\Omega^2} \sin^2\left(\frac{\Omega t}{2}\right) , \tag{1.5}$$

where Ω_0 is the Rabi frequency and $\Omega^2 = \Omega_0^2 + (\omega - \omega_0)^2$ is the generalised Rabi frequency, which is a function of the frequency detuning from the resonance ω_0. The Rabi line shape is shown in Fig. 1.2. From Eq. (1.5), it can be seen that the excitation probability is maximised with $\Omega t = \pi$, which is referred to as a π-pulse. For a π-pulse of duration t, the FWHM, i.e. the transition linewidth, is equal to $\Delta\nu = 0.7987/t$.

The choice of a reference for an optical clock is also largely driven by insensitivity to external fields that would cause a systematic shift to the clock transition frequency. If the system is resilient against such perturbations, the frequency measurement has the potential of being very accurate. Section 1.4 will discuss in more detail how different frequency standards are affected by systematic perturbations.

1.3.2 Oscillator: ultrastable laser

For optical clocks, the *oscillator* component consists of an ultrastable laser of the same frequency as that of the optical clock transition. This laser is referred to as the local oscillator (LO). The short-term stability of the LO is extremely important for a number of reasons. First of all, as explained in the previous section, the duration of the probe is inversely proportional to the linewidth. In order to improve the Q factor of the clock, long probe times must be used; however, one of the limits on the probe duration lies in the coherence time of the probe light.

Furthermore, during a clock cycle there is a certain amount of dead time during which the clock transition is not being probed. This causes a degradation of the stability of the clock which depends on the frequency noise of the LO during the dead time between two probes. This is known as the Dick effect [12], and is more prominent in systems with a low duty cycle (i.e. the proportion of probe time to dead time), and can be reduced by improving the stability of the clock laser.

1.3.3 Counter: femtosecond frequency comb

Femtosecond optical frequency combs are required in order to count the "ticks" of an optical clock. Frequency combs are based on a train of periodic pulses at a repetition frequency f_{rep} from a mode-locked femtosecond laser [13, 14]. Fig. 1.3 shows a schematic that illustrates the principles of a frequency comb. The frequency of the n^{th} mode of the comb is given by:

$$f_n = n f_{\text{rep}} + f_0 \; , \tag{1.6}$$

where $f_0 = f_{\text{rep}} \frac{\Delta\phi}{2\pi}$ is the carrier-envelope offset (CEO) frequency, with $\Delta\phi$ being the shift in the carrier-envelope phase from the peak of the pulse envelope. The repetition frequency f_{rep} is determined by measuring the beat frequency between two adjacent comb modes. In order to measure f_0, the frequency comb must span at least an octave, such that it can be determined using a $f - 2f$ self referencing scheme [15, 16].

$$2f_n - f_{2n} = 2(n f_{\text{rep}} + f_0) - (2n f_{\text{rep}} + f_0) = f_0 \; . \tag{1.7}$$

Finally, the optical frequency f_{opt} is found by measuring the signal of its beat with the nearest comb mode. Note that both f_{rep} and f_0 are expressed in SI Hz, meaning that

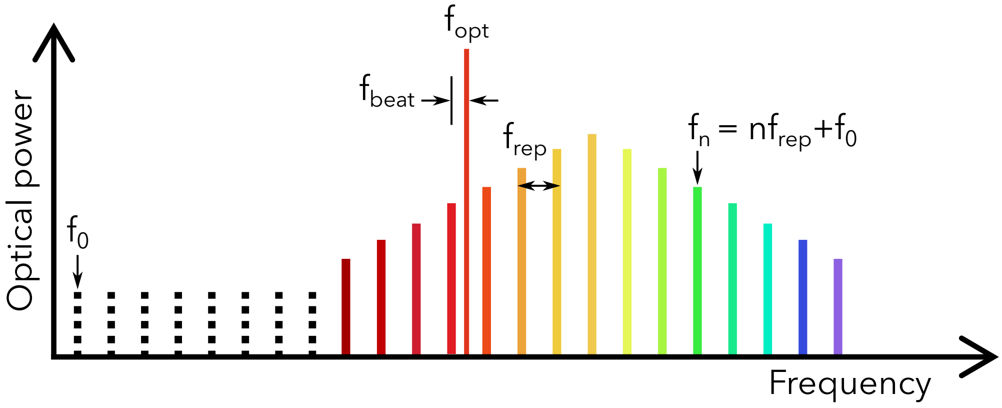

Figure 1.3: Schematic of a femtosecond optical frequency comb.

they must be referenced to the microwave standard, such as a 10 MHz signal from a H maser steered by a Cs fountain clock. The accuracy of an *absolute* measurement of the optical frequency is thus limited by Cs.

1.4 Optical frequency standards

The two most common types of system at the basis of optical clocks are an optical lattice of neutral atoms and a single trapped ion. One of the main differences between the two lies in how the number of atoms N affects the measurement, and can be easily identified by referring back to Eq. (1.3). In the case of an optical lattice clock, the large number of atoms lead to a high SNR, giving rise to low statistical uncertainties. However, larger systematic shifts must be traded for this lower instability. On the other hand, while a single trapped ion is a good approximation of an isolated particle at rest, and its low sensitivity to external perturbations means that a very high measurement accuracy can be achieved [17], the low SNR poses a limit on the clock's stability.

1.4.1 Single-ion clocks

The most common choice of ion trap at the basis of single-ion optical clocks is the Paul trap [18], which confines the ion in a time varying quadrupole potential (see Fig. 1.4) produced by the electrodes. Compared to the Penning trap, which requires strong electric and magnetic fields that would cause high levels of perturbation to the ion, the Paul trap is a more appropriate choice for precision metrology, as it is relatively simple to minimise the environmental effects.

There are various species of ion that are suitable for an optical frequency standard. The $^{171}\text{Yb}^+$ ion [7, 19] is an excellent candidate thanks to the extremely narrow linewidth of its E3 transition, of the order of nHz [20, 21], and whose excited state $^2\text{F}_{7/2}$ has a lifetime of around 1.6 years [22]. One of the advantages of $^{171}\text{Yb}^+$ is the presence of a second optical transition, the E2 transition [23], with a narrow enough natural linewidth suitable to be a frequency standard. Furthermore, the exceptional sensitivity of the octupole transition to the variation of the fine structure constant (see section 1.6.1) makes $^{171}\text{Yb}^+$ ideal for testing fundamental physics [24, 25]. The best ion-ion clock comparison so far has been performed between two $^{171}\text{Yb}^+$ clocks, which demonstrated agreement within

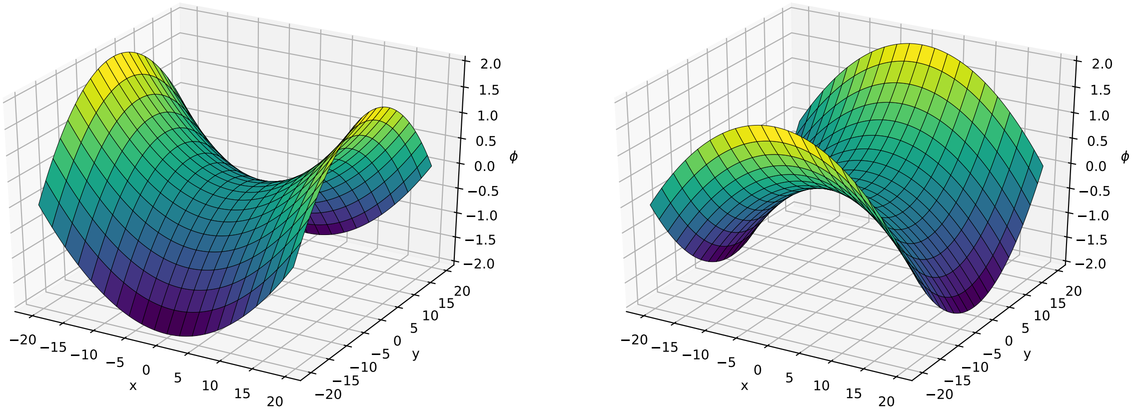

(a) $t = 0$ **(b)** $t = T/2$

Figure 1.4: Time-varying quadrupole trapping potential ϕ with period T in a Paul-style trap.

the measured combined uncertainties of 4×10^{-18} [26].

Another example is the ^{88}Sr^{+} ion [27–30], which has no hyperfine structure, and whose quadrupole transition ^{2}S$_{1/2}$ − ^{2}D$_{5/2}$ has a linewidth of 0.4 Hz. It was also identified as advantageous since readily available solid-state laser sources were suitable for both the cooling and the interrogation of the ion [31]. Dubé *et al.* were able to achieve clock stability approaching the QPN limit [29], and measured a fractional uncertainty of 1.1×10^{-17}, dominated by the Black Body Radiation (BBR) shift.

The ^{40}Ca^{+} ion [32, 33], mostly used in the context of quantum information, is similar to ^{88}Sr^{+} in lacking a hyperfine structure, allowing once again for simple laser systems [34]. The commercial availability of the solid-state and diode lasers required for the operation of a ^{40}Ca^{+} optical clock make it feasible to construct practical setups [35], motivating Cao *et al.* to develop a compact and robust transportable optical clock based on ^{40}Ca^{+} [36].

The ^{199}Hg^{+} ion has also been investigated, specifically by the National Institute of Standards and Technology (NIST) in Colorado [14, 37–39]. The ion is confined in a cryogenic RF Paul trap, and the wavelengths in the setup are particularly low, in the ultraviolet (UV) region (194 nm for Doppler cooling and a 282 nm for probing the quadrupole clock transition). ^{199}Hg^{+} was the first ion on which the method of averaging the measured clock frequency over three orthogonal magnetic fields for suppressing the electric quadrupole shift was used [38, 40], a method which has since been adopted by various other groups for the elimination of this systematic shift.

While the aforementioned ions had an alkali-like or quasi-alkali-like atomic structure, the ^{27}Al^{+} and ^{115}In^{+} ions have two valence electrons, with an alkaline earth-like structure [41]. Both these ions are highly immune to environmental perturbations [42, 43]. ^{27}Al^{+} is a particularly interesting example, as the readout of the clock state is enabled by the use of quantum logic spectroscopy [44]. Since both laser cooling and direct state detection are not feasible in ^{27}Al^{+}, the ion must be trapped together with another ion which is able to provide sympathetic cooling, and can be coupled with the clock state of ^{27}Al^{+}

[39]. In the first experimental realisation, $^{9}\mathrm{Be}^{+}$ was used as the logic ion by Rosenband *et al.* [43], however since then the $^{25}\mathrm{Mg}^{+}$ ion has been implemented instead by the same group, as it requires fewer cooling lasers [45]. Others use a $^{40}\mathrm{Ca}^{+}$ logic ion [46] not only thanks to the simplicity of the laser setup, but also because of its well known features in quantum information processing [47]. In 2019, an $^{27}\mathrm{Al}^{+}$ based clock became the first optical clock to achieve a sub-10^{-18} estimated fractional systematic frequency uncertainty [6]. On the other hand, for $^{115}\mathrm{In}^{+}$, while it is possible to perform direct state detection, it is not feasible to directly cool the ion. For this reason, the ion is trapped together with a $^{40}\mathrm{Ca}^{+}$ ion that provides sympathetic cooling [48, 49].

1.4.2 Optical lattice clocks

The optical lattice clock, first proposed by Katori in 2002 [50], is based on a multitude of cold neutral atoms trapped in an optical lattice [51], which consists of an optical standing wave potential, as shown in Fig. 1.5. The atoms are first cooled in a magneto-optical trap (MOT) before being loaded into the lattice. The light fields which are then used to confine the atoms cause a strong perturbation to their energy levels. However, if the light of the lattice laser is tuned to a particular wavelength (*magic wavelength*), then the ground and excited clock states are shifted by the same amount, resulting in zero light shift on the clock transition to first order [52]. This effect was first demonstrated experimentally by Takamoto *et al.* [53] using $^{87}\mathrm{Sr}$ atoms.

The most commonly used candidates for neutral atom frequency standards are the

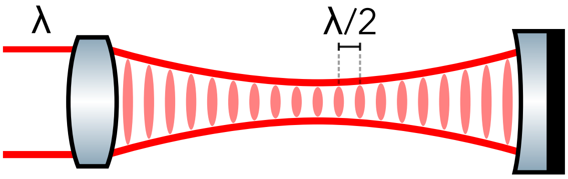

Figure 1.5: Diagram of a 1D optical lattice, in which each lattice site is separated by $\lambda/2$, where λ is the wavelength of the light forming the standing wave.

Sr and Yb atoms. Both atoms present a $^1\mathrm{S}_0 - {}^3\mathrm{P}_0$ transition, which for the fermionic isotopes ^{87}Sr and ^{171}Yb is only weakly allowed, leading to mHz linewidths. Furthermore, for these fermionic isotopes, the collisional shifts between atoms in the lattice would ideally be suppressed by the Pauli exclusion principle [17]. The ^{87}Sr atom, with its 1-mHz natural linewidth and high Q factor, has been employed for optical lattice clocks by various national measurement institutes (NMI) [54–58]. Moreover, optical clocks based on ^{171}Yb [59–63] are of particular interest due to the atom's simpler atomic structure determined by the nuclear spin $I = 1/2$, as opposed to ^{87}Sr with spin $I = 9/2$ [59], allowing for a simpler laser setup for cooling and probing the atoms. Aside from the fermionic isotopes of Sr and Yb, the ^{199}Hg atom has also been used for optical lattice clocks [64–66]. Although the operating wavelengths are less convenient, being in the UV range, the BBR shift, which usually dominates an optical lattice clock's uncertainty budget, is lower in ^{199}Hg by an order of magnitude compared to ^{87}Sr and ^{171}Yb.

The bosonic isotopes ^{88}Sr [67–69] and ^{174}Yb [70, 71] have also been investigated for use in optical lattice clocks. For these isotopes, the $^1\mathrm{S}_0 - {}^3\mathrm{P}_0$ transition is even more strongly forbidden for a single-photon excitation; however, it can become allowed with the introduction of a coupling magnetic field [67]. Moreover, the clock transition has a low sensitivity to lattice polarisation effects, since the introduced magnetic field is the only source of interaction between the clock state and lattice light polarisation, which can be carefully controlled [69]. It must be noted that, as for bosons the Pauli exclusion principle does not hold, collisional effects are more significant [72]. The advantages of ^{88}Sr include its higher abundance in nature and simpler cooling schemes [68].

1.4.3 Next-generation clocks

Aside from optical clocks based on single ions or neutral atom lattices, there have recently been proposals for different types of optical clocks which would be even more suitable for fundamental physics tests, particularly for the more extreme atomic properties that lead to a higher sensitivity to the variation of the fine structure constant (discussed in more detail in section 1.6.1). Berengut, Dzuba and Flambaum [73] identified suitable narrow optical transitions in highly charged ions (HCI) for high-precision clock operation. Optical clocks based on HCI [74–77] have the possibility to achieve lower systematic uncertainties thanks to the significantly higher insensitivity to environmental perturbations, which is due to the more compact size of the HCI's electronic cloud.

Nuclear optical clocks have also been proposed, based on a narrow nuclear transition in ^{229}Th [78–81]. Because the nucleus is shielded from the environment by the surrounding electron cloud, and it can only interact with small nuclear moments, systematic frequency shifts would be much smaller than for single-ion and optical lattice clocks [82]. Furthermore, nuclear clocks could trap atoms in a solid-state crystal lattice, allowing a large number of atoms to be interrogated (several orders of magnitude more than for optical lattice clocks), resulting in an extremely improved clock stability from the high SNR [83].

There have also been proposals for a composite optical clock, consisting of a combination of an optical lattice clock and a single-ion clock [84]. As mentioned in section 1.3.2, the coherence time of the LO is a limiting factor to the optical clock stability that can be achieved. With the *differential spectroscopy* protocol [85], it is possible to use two phase-synchronised LOs to probe an optical lattice and a single ion. Corrections to the phase can be made with feedback from the higher-stability lattice clock, enabling the single-ion clock to be operated beyond the coherence time of the LO. This method would benefit from both the high stability of optical lattice clocks and the low systematic uncertainties of single-ion clocks.

1.5 Towards the redefinition of the SI second

As the SI second is currently defined in terms of the hyperfine transition in Cs, any absolute frequency measurement must be related to this realisation of the second. In practice, when a frequency comb measures the absolute frequency of an optical clock transition, this is achieved by using a 10-MHz signal from a H maser as the reference frequency for the comb, which in turn is measured relative to a Cs fountain clock. Because of the high level of accuracy and stability that can now be achieved by optical clocks, the uncertainty in the measurement of the absolute transition frequencies of certain atoms is limited by the accuracy and stability of the current Cs primary standard. Therefore, in order to improve the limit on the achievable accuracy, a redefinition of the SI second is necessary in terms of an optical transition frequency.

Advancements in atomic clocks will lead to an improvement in the time scales. International Atomic Time (TAI) is the result of the periodic comparison between hundreds of atomic clocks across around 80 institutes. A weighted average of each local realisation of the second is taken based on the clocks' performances and is used to regularly calibrate the time scale. Several species of ions and neutral atoms with optical transitions have already been accepted as secondary representations of the second [86], meaning that they are suitable to already contribute to the calibration of TAI through the comparison with the primary standard, despite the limited level of uncertainty. Once the SI second is redefined in terms of an optical frequency, these optical clocks can start contributing to TAI with a higher level of accuracy.

Before the impending redefinition, a lot of work must be done to properly characterise the performance of optical clocks and compare the frequencies between different systems. The limitation imposed by the caesium standard is overcome by performing measurements of the frequency ratio between two optical clocks. These kinds of measurements reveal the true limit on the accuracy imposed by the optical standards. In order to strengthen the basis on which the second would be redefined, international clock comparison campaigns are routinely carried out between various laboratories to compare the frequencies of distant clocks through optical fibre links.

The International Committee for Weights and Measures (CIPM) has proposed a set of milestones that need to be collectively accomplished before the second can be redefined [87]. These include the achievement of uncertainties two orders of magnitude below that of Cs by several optical clocks, and the agreement of frequency ratios between various institutes within the 10^{-18} level. It is also required for several optical clocks to be contributing to TAI as secondary representations of the second.

1.5.1 Absolute frequency measurement

One common method to measure the absolute frequency of an optical transition is to directly measure the ratio of the optical frequency with the frequency of the Cs primary standard, which would be provided by a local H maser calibrated by a Cs fountain clock. The reason why masers are used as an intermediate reference is because of their long-term reliability, high short-term stability and low phase noise [88]. High accuracies have been achieved with such absolute frequency measurements, for instance for ^{171}Yb [89, 90], ^{171}Yb$^+$ [24, 25], ^{88}Sr$^+$ [28], ^{87}Sr [91].

An alternative method has more recently started to be explored, which is to reference the measured optical frequency to the SI second through a link to TAI [92–96]. The optical frequency is measured by a frequency comb relative to the signal from the local maser reference, whose frequency is in turn continuously compared with TAI via satellite links. As the frequency of TAI is the result of a weighted average of hundreds of participating atomic clocks, the systematic bias could potentially be reduced with such a measurement. This method is also advantageous in case a Cs frequency standard is not available locally for direct comparison. Chapter 5 will cover in detail this type of absolute frequency measurement technique.

1.5.2 Optical frequency ratio measurement

The measurement of the ratio between two optical frequencies is fundamental for the characterisation of the true limit on the accuracy achievable by optical clocks. Ratio measurement results are also incorporated together with absolute frequency measurements in the calculation of the optical frequency values chosen to be secondary representations of the second [87, 97]. While absolute frequency measurements can be performed independently by each laboratory, measurements of the ratio between two optical frequencies typically involve an optical fibre connection between the optical clocks, whose frequencies are compared by a frequency comb. The measurement of the frequency ratio between two clocks in the same laboratory [32, 39, 45, 55, 98–101] would be free from the gravitational redshift, and if the ratio is measured between two optical transitions in the same ion, particularly the E3 and E2 in ^{171}Yb^{+}[25, 102], this would be free from other common noise sources.

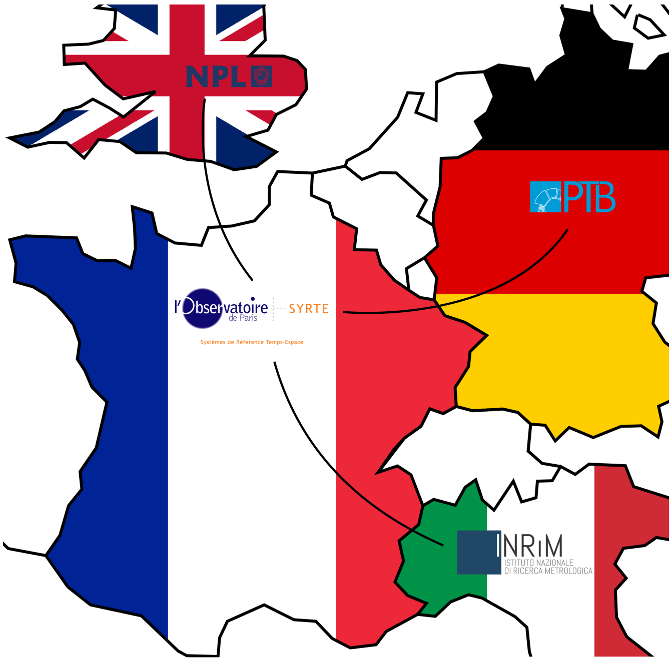

Figure 1.6: Ground-based European network of clocks connected via optical fibres, including NPL in the United Kingdom, SYRTE in France, PTB in Germany and INRIM in Italy.

For a more robust demonstration of the reproducibility of optical clocks, optical fibre link networks have been constructed to connect multiple laboratories to enable their collaboration in the context of coordinated clock comparison campaigns (see chapter 6). A European network of clocks connected via optical fibre frequency links has already been established, as shown in Fig. 1.6, and is yet to be further expanded [103]. Other optical fibre networks include the link between the National Institute of Standards and Technology (NIST) and JILA in Colorado, United States [104] and between the National Institute of Information and Communications Technology (NICT) and the University of Tokyo [105].

Ratio measurements between distant laboratories have been published [106–108] in which the optical frequency transfer contributes negligibly to the overall stability and uncertainty of the frequency measurement. Another demonstration of the reproducibility of optical clocks is the loop closure relationship $\frac{\nu_a}{\nu_b} \times \frac{\nu_b}{\nu_c} \times \frac{\nu_c}{\nu_a} = 1$ which was demonstrated through three measurements conducted at RIKEN (Japan) [109–111] to be consistent beyond the SI limit for three optical clocks based on ^{199}Hg, ^{171}Yb and ^{87}Sr respectively.

1.6 Applications

1.6.1 Measurement of the variation of fundamental constants

The exceptional stability and accuracy of optical clocks has started to be exploited for the search of new physics, particularly the variation of fundamental constants. The fine-structure constant α is responsible for the coupling of charges with electromagnetic fields, which determines the transition frequency between two energy levels [112]. Furthermore, transitions between hyperfine levels also depend on the proton-to-electron mass ratio $\mu = m_\mathrm{p}/m_\mathrm{e}$ fundamental constant.

As optical clocks are based on atomic transitions between two energy levels, the rate of their “ticking” would be affected by a frequency shift originating from the slow, long term drift of α. This drift can be measured by comparing two transitions of different clocks with different sensitivities to changes in α, such that if α is varying, it would be possible to detect the energy levels drifting away or towards each other [113].

The rate of variation of α is measured via:

$$\frac{\dot{r}}{r} = (K_1 - K_2)\,\frac{\dot{\alpha}}{\alpha}\,, \tag{1.8}$$

where $r = \nu_1/\nu_2$ is the ratio between two clock transition frequencies and K_i are the sensitivity coefficients that differ for each clock transition [114]. For a particular clock transition ν_i, the sensitivity to α is defined by [77]:

$$K_i = \frac{\partial \ln\left(\frac{\nu_i}{cR_\infty}\right)}{\partial \ln \alpha}\,, \tag{1.9}$$

where R_∞ is the Rydberg constant. The E3 transition in $^{171}\mathrm{Yb}^+$ has a particularly high sensitivity to the variation of α, namely $K_{\mathrm{E3}} = -5.95$, being the highest sensitivity factor out of all currently operational single-ion and optical lattice clocks, followed by Hg^+ with $K_{\mathrm{Hg}^+} = -2.94$. Generally, these coefficients are otherwise relatively low, between 0.008 and 1.0 [115].

The current experimental constraint on the slow drift of α are derived by Lange *et al.* [102] from measurements of the ratio between the E3 and E2 transitions of $^{171}\mathrm{Yb}^+$ between 2016 and 2020. The constraint is given by:

$$\frac{\dot{\alpha}}{\alpha} = (1.0 \pm 1.1) \times 10^{-18}\ \mathrm{year}^{-1}. \tag{1.10}$$

Furthermore, Lange *et al.* also determined the most up-to-date limits to the slow drift of μ based on $^{171}\mathrm{Yb}^+$(E3)/Cs ratio data from between 2010 and 2019:

$$\frac{\dot{\mu}}{\mu} = (-0.8 \pm 3.6) \times 10^{-17}\ \mathrm{year}^{-1}. \tag{1.11}$$

As previously mentioned, new types of atomic clocks with higher sensitivities to the variation of the fine structure constant have been proposed, such as HCI clocks and nuclear clocks. Berengut, Dzuba and Flambaum [73] demonstrated the high sensitivity of HCI clocks to the variation of α, surpassing the K factor of $^{171}\mathrm{Yb}^{+}$ E3 by two orders of magnitude. K factors of various species of HCI clocks are listed in the review by Kozlov *et al.* [75]. Furthermore, a UV nuclear transition in $^{229}\mathrm{Th}$ has been proposed as a good candidate, where Flambaum [78] predicted that a limit to the variation of α as stringent as 10^{-23} year^{-1} could be achievable in the future.

1.6.2 Dark matter detection

It is predicted that the coupling of light dark matter fields to the particles and fields of the Standard Model could lead to a shift in frequency or phase of atomic energy levels. This would lead to an apparent change in the value of the fine structure constant [116, 117]. One possible model is that self-interactions within the dark matter field could cause it to form clumps, known as topological defects, stationary in the galactic rest frame. Fig. 1.7 shows a

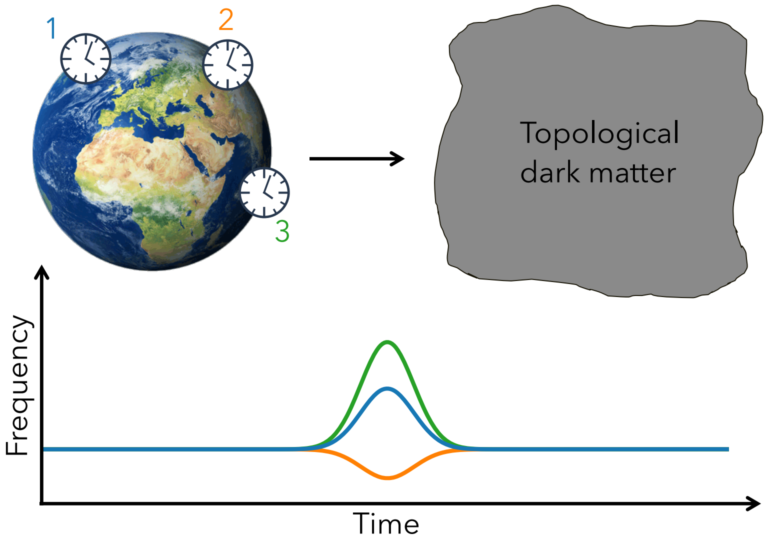

Figure 1.7: Diagram showing how different species of optical clocks would perceive a frequency shift upon the interaction with a topological dark matter.

schematic of the Earth sweeping through a dark matter defect, causing a desynchronisation between different clocks at different locations. This would appear as simultaneous spikes within a clock network, identified distinctly from all other systematic noise sources [118].

While there is no knowledge on the frequency of transient dark matter events, measurement campaigns involving a multitude of optical clocks in various laboratories are being carried out with the scope of posing constraints on on $\delta\alpha/\alpha$ depending on the transient duration of the event and the size of the topological defect. In 2016, Wcisło *et al.* [119] proposed an experimental approach that did not require clock signals to be correlated in real time, instead relying on precise time stamps that can be independently correlated in post-processing.

While that work only compared the readouts of two co-located optical clocks, in 2018 Wcisło *et al.* [116] improved the constraint on $\delta\alpha/\alpha$ by two orders of magnitude in an experiment conducted in an earth-scale network of distant optical clocks. The most up-to-date constraint on the transient variation of α is given by Roberts *et al.* [108], who analysed ratio data of optical clocks at NPL, Systèmes de Référence Temps-Espace (SYRTE) in France, and Physikalisch-Technische Bundesanstalt (PTB) in Germany connected via fibre links, and measured $|\delta\alpha/\alpha| < 5 \times 10^{-17}$ for transient durations of 10^3 s.

1.6.3 Chronometric geodesy

From the theory of general relativity, it is known that clocks are sensitive to the gravity potential, meaning that two identical clocks in different locations on the Earth would exhibit different ticking rates due to the different gravitational redshift they experience. This frequency shift is given fractionally by:

$$\frac{\Delta\nu}{\nu_0} = \frac{g\Delta h}{c^2}\ , \tag{1.12}$$

where g is the local gravitational acceleration and Δh represents a change in height [120].

To compare the frequency between two optical clocks, the gravitational redshift must be known to a very high level of accuracy, since a gravity potential difference equivalent to 1 cm height difference corresponds to a fractional frequency offset of 10^{-18}. Modern geodetic levelling methods are not suitable over large distances such as hundreds of kilometers. The technique of levelling [121] can be used to measure relative heights and potential differences over short distances with millimetre resolution; however, this method becomes less accurate over longer distances. On the other hand, the Global Navigation Satellite System (GNSS) is much better suited to measuring gravity potentials over large distances; however, the results do not account for small local variations. The best method currently available to determine the gravity potential in a specific location relies on a combination of GNSS data and local variations of g that can then be fed into models. The resulting uncertainty is of the order of a few centimetres [122, 123].

The uncertainties from current geodetic levelling methods are limiting the accuracy of clock comparisons. However, once the performance of optical clocks has been validated at the 10^{-18} level through local ratios, free of the gravitational red shift, the optical clocks themselves will become the most suitable tools to conduct high-resolution geodetic measurements.

Grotti *et al.* [124] conducted an experiment in the Alps with a transportable ^{87}Sr optical clock [125] determining the height difference between two locations separated by 90 km. The results were altogether consistent with the potential measured with GNSS methods. This was the first experimental demonstration showing how transportable optical clocks could be deployed in the field for geodetic measurements. More recently, a gravimetric measurement was performed at the centimetre level with a pair of transportable ^{87}Sr optical clocks separated by 450 m in height at a broadcasting tower in Tokyo [126, 127].

Bondarescu *et al.* investigate how the gravitational effect of underground density anomalies such as. oil/gas reservoirs or ore deposits can be measured by an optical clock [128]. In a later work, they also explore the possibility of employing an optical clock to measure the effect of an inflating magma chamber causing changes in the gravity potential from mass redistribution and vertical displacement [129].

1.6.4 Compact optical clocks for space

While optical clocks strongly rely on comparisons between one another, the uncertainties on frequency measurements would be limited by satellite links for cross-continent comparisons [130]. Moreover, while optical fibre links can preserve the stability of the frequency transfer over hundreds of kilometres [106, 131, 132], it is not yet known how to achieve this on an intercontinental scale.

The prospect of creating a satellite network of space-borne optical clocks is appealing for a wide range of reasons, as this would not only enable more accurate frequency comparisons between ground-based optical clocks worldwide, but would also enhance the performance of chronometric geodesy, time dissemination, global navigation and also fundamental physics tests [133]. In fact, a global positioning system with onboard optical clocks would effectively constitute an Earth-scale dark matter detector [118].

Current state-of-the-art optical clock systems are almost exclusively developed in research laboratories, where the various components form a bulky and complex setup that usually takes up the size of an entire room, and where the environmental conditions are highly controlled. In order for optical clocks to be deployed into space, these need to be redesigned into more compact systems. Work has been done over the years to reduce the size of optical clock setups to allow them to be transported [125, 126, 133–135], while trying to preserve their stability and accuracy. In 2016, Lezius *et al.* were the first to realise and deploy an atomic clock in space based on the measurement of an optical transition with a frequency comb [136]. Its successful operation in microgravity conditions paves the way for future implementation of optical clock technology in space.

1.7 Summary and thesis outline

This chapter has introduced the general principles of atomic clocks and shown several instances in which optical clocks bring improvements. Different species of frequency standards were presented and compared. The motivation for redefining the SI second in terms of an optical frequency was explained, and the different techniques for optical frequency measurement were described. Finally, the applications of optical clocks aside from precision metrology were discussed, including testing fundamental physics and chronometric geodesy.

The next chapters of this thesis focus on the ytterbium ion optical clock at NPL. Chapter 2 will present the experimental setup and methodology for operating the $^{171}\text{Yb}^{+}$ clock, from loading and trapping the ion to probing and measuring the clock transition. Chapter 3 will explain the experimental control system used to run the optical clock, emphasising various aspects of experiment automation that were achieved with its implementation. Chapter 4 will cover the various systematic frequency shifts that the ion experiences, and how they are measured and automatically analysed. Chapter 5 will focus on the methodology for measuring the absolute frequency of the optical clock with reference to TAI, and how this analysis was integrated in a generalised and automated framework. Chapter 6 will present the key results from three clock comparison campaigns that the $^{171}\text{Yb}^{+}$ ion clock participated in throughout my time at NPL. Finally, Chapter 7 will summarise the thesis and present some plans and ideas for future work.

Note that I was not the only one working on the $^{171}\text{Yb}^{+}$ ion optical clock for the duration of my PhD, and therefore there are some aspects of the experiment described in this thesis that were a result of team work. In the conclusion section of each upcoming chapter, it will be made clear what my specific contributions were. My largest contributions are presented in Chapters 3, 4 and 5, and most the work presented in these chapters was carried out by me. Furthermore, in terms of running the optical clock for measurement campaigns (as discussed in Chapter 6) and analysing the resulting data, my level of contribution increased over the years in each campaign.

2 Experimental setup

To say that an optical atomic clock is made up of three components – an atomic transition as a reference, a laser as an oscillator, and a frequency comb as a counter – is a severe understatement. In reality, there is a large number of sub-systems that make up each of those three components, which for a state-of-the-art system such as this one span across two separate room-sized laboratories. While one laboratory contains the frequency comb apparatus required for both measuring and stabilising the frequency of the oscillator, this chapter will describe in detail the experimental setup in the ytterbium ion laboratory, in which the ion is trapped, cooled, and probed.

Section 2.1 describes the atomic structure of $^{171}\mathrm{Yb}^{+}$, the role of each laser wavelength used in the setup, and how all the wavelengths are measured and delivered to the ion. Section 2.2 describes the ion trap and vacuum chamber design, and the processes for loading and trapping a single $^{171}\mathrm{Yb}^{+}$ ion. Section 2.3 outlines the process for laser-cooling the ion and the laser systems required to do so. The technique for detecting a single ion in the trap will also be explained. Section 2.4 describes the laser systems required for probing the two clock transitions, the probe sequence itself, and different algorithms for locking to a clock transition. Section 2.5 explains the methods for stabilising the frequencies of the clock lasers and for directly measuring them with the frequency comb.

2.1 The $^{171}\mathrm{Yb}^{+}$ ion

At the heart of the experiment lies a single $^{171}\mathrm{Yb}^{+}$ ion. Natural ytterbium is part of the lanthanide series of elements and has an atomic number of 70. There are seven stable isotopes of ytterbium, of which $^{171}\mathrm{Yb}$ has a natural abundance of 14.216 % [137]. Because of the odd-numbered isotope, the imbalance between the number of protons and neutrons causes a nonzero nuclear spin, which in turn leads to hyperfine splittings in the atomic energy levels. Only two out of the seven isotopes have an odd atomic mass number, ^{171}Yb with a nuclear spin of $I = 1/2$ and ^{173}Yb with a nuclear spin of $I = 5/2$. ^{171}Yb is therefore chosen for its simplest resulting hyperfine structure. A hyperfine structure is advantageous for atomic clocks because transitions between integer hyperfine levels allow $m_F = 0 \ \rightarrow m_F = 0$ transitions, which are insensitive to the first-order Zeeman shift.

2.1.1 Atomic structure

The energy level diagram of ^{171}Yb^{+} is shown in Fig. 2.1. One of the unique characteristics of ^{171}Yb^{+} is the presence of two optical clock transitions: the electric quadrupole (E2) transition $^2\mathrm{S}_{1/2} \ \rightarrow \ ^2\mathrm{D}_{3/2}$ at 436 nm and the electric octupole (E3) transition $^2\mathrm{S}_{1/2} \ \rightarrow \ ^2\mathrm{F}_{7/2}$ at 467 nm, both of which have a narrow enough linewidth to be a suitable frequency standard.

The transition $^2\mathrm{S}_{1/2}(F = 1) \ \rightarrow \ ^2\mathrm{P}_{1/2}(F = 0)$ at 369.562 nm is used for laser-cooling the ion. This dipole-allowed transition has a natural linewidth of 19.60(5) MHz, corresponding to a lifetime of 8.12(2) ns of the $^2\mathrm{P}_{1/2}$ state [138]. The ion can take a few routes to leave the cooling cycle, the most likely of which is through a spontaneous decay to the $^2\mathrm{D}_{3/2}$ metastable state with a branching ratio of 0.501(15) % [139]. Light at 935.188 nm is required to repump the ion from the $^2\mathrm{D}_{3/2}$ state to the $^3[3/2]_{1/2}$ state, whose lifetime of 37.7(5) ns [140] allows it to rapidly decay back to the ground state and re-enter the cooling cycle.

Two electro-optic modulators (EOM) are used to apply sidebands to the 370-nm cooling light in order to target the relevant hyperfine transitions between the $^2\mathrm{S}_{1/2}$ and $\mathrm{P}_{1/2}$ states. Specifically, a 2.1-GHz sideband is applied to target the $^2\mathrm{S}_{1/2}(F = 1)$ and $\mathrm{P}_{1/2}(F = 1)$ transition such that the ion can decay to the $^2\mathrm{S}_{1/2}(F = 0)$ state where it can undergo a clock transition. Because of this, this beam is referred to as the *state-preparation* beam. Additionally, a 14.7-GHz sideband is applied in order for the ion to re-enter the

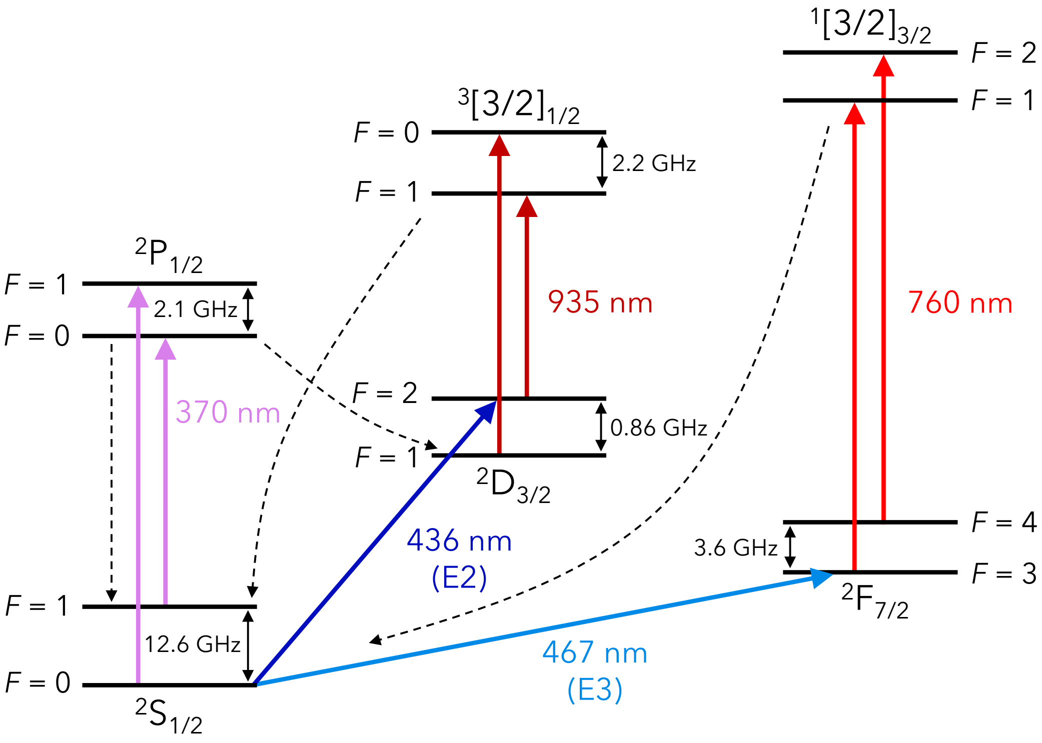

Figure 2.1: Atomic structure of ^{171}Yb$^+$. 370-nm light is used to Doppler-cool the ion. Two optical clock transitions are available, a quadrupole (E2) at 436 nm and an octupole (E3) at 467 nm. 935- and 760-nm lasers are used to repump the ion out of the E2 and E3 clock states respectively such that it can spontaneously decay back to the ground state.

cooling cycle from the $^2S_{1/2}(F = 0)$ state.

The E3 transition at 467 nm has an exceptionally narrow natural linewidth, of the order of a few tens of nHz, given its upper-state lifetime of 1.6 years [22]. A 760-nm laser (see Appendix A.1) is used to repump the ion out of the long-lived clock state into the $^1[3/2]_{3/2}$ state, which has a lifetime of 30.9(6) ns [141], allowing it to decay back into the cooling cycle. The E2 transition at 436 nm has a natural linewidth of 3.1 Hz [23] with an upper-state lifetime of 51.3 ms. Upon a successful excitation to the $^2D_{3/2}$ state, the 935-nm laser (see Appendix A.2) is used to repump the ion back into the cooling cycle.

Finally, ^{171}Yb also has a dipole transition $^1S_0 \rightarrow {}^1P_1$ at 398.911 nm [142] that is used in the first step of a two-photon ionisation process to ionise the ^{171}Yb atom. The second step is carried out by the 370-nm laser, providing the energy required for ^{171}Yb to be excited from ^{1}P$_1$ to the continuum, which results in its ionisation.

There are several advantages of using the ^{171}Yb^{+} ion as a reference for an optical clock. Because the natural linewidth of the E3 transition is so narrow, it will never pose a limitation on the achievable instability. Moreover, the systematic shifts to the E3 transition frequency are generally very low. It is particularly useful to be able to probe two different transitions on the same single trapped ion: since the E2 transition is more sensitive to magnetic or electric fields, it can be used as a sensor of the external field disturbances. Scaled-down frequency corrections can then be applied to the E3 transition frequency.

2.1.2 Light delivery and measurement

All the wavelengths involved in cooling, photo-ionisation, probing and repumping are in a range for which many lasers are commercially available, meaning that the optical systems required for operating a ^{171}Yb^{+} ion clock can be reliable and robust. Laser setups are in place targeting each one of the transitions pictured in Fig. 2.1. To deliver the laser light to the ion, the light from each system is coupled into polarisation-maintaining (PM) fibres, which all come together at the Beam Combiner, shown in Fig. 2.2. In this setup, the light from each fibre is collimated by a Thorlabs FibrePort collimator, whose appropriate choice is determined by the wavelength, beam waist, and the fibre's mode field diameter. All the wavelengths are combined into a colinear beam by a series of single-edge laser dichroic beam splitters[1], and are then coupled by a parabolic collimator[2] into an endlessly-single-mode photonic-crystal fibre[3] (PCF) which sends the light to the ion. The parabolic mirror and PCF are chosen because they can accommodate the whole range of wavelengths without introducing chromatic aberrations. The 5 degrees of freedom of

---

[1] Laser 2000 Photonics BrightLine®

[2] Thorlabs RC02FC-P01

[3] NKT Photonics aeroGUIDE-5-PM

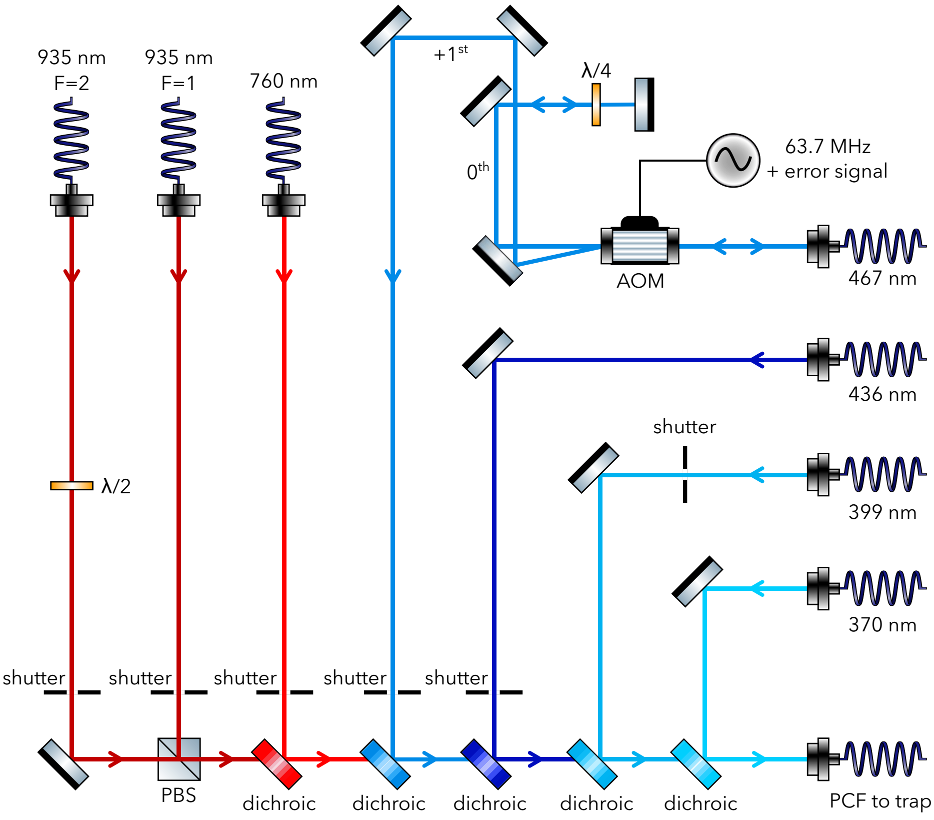

Figure 2.2: Diagram of the Beam Combiner setup. The light from each wavelength is combined in a series of dichroic mirrors and coupled by a parabolic mirror into the PCF that sends the light to the ion. This diagram, together with the other diagrams in this thesis depicting optical setups, made use of the ComponentLibrary by Alexander Franzen [143].

the FibrePorts allow the setup to contain a minimal number of mirrors for fibre-coupling, making it simple, compact and robust. Prior to this Beam Combiner, the lasers were delivered by free-space and brought together on a setup of polarising beam splitters (PBS), resulting in a less robust setup and poor coupling efficiencies into the PCF.

The wavelength of each beam is measured by a High-Finesse Wavelength Meter[4] at a 0.1 pm precision. This measurement is useful to select the appropriate cavity mode to lock a laser to, and it provides a suitable resolution for any free-running laser. From each laser setup, a pick-off is installed such that a small portion of the light is coupled into a fibre

---

[4] WS/6-200

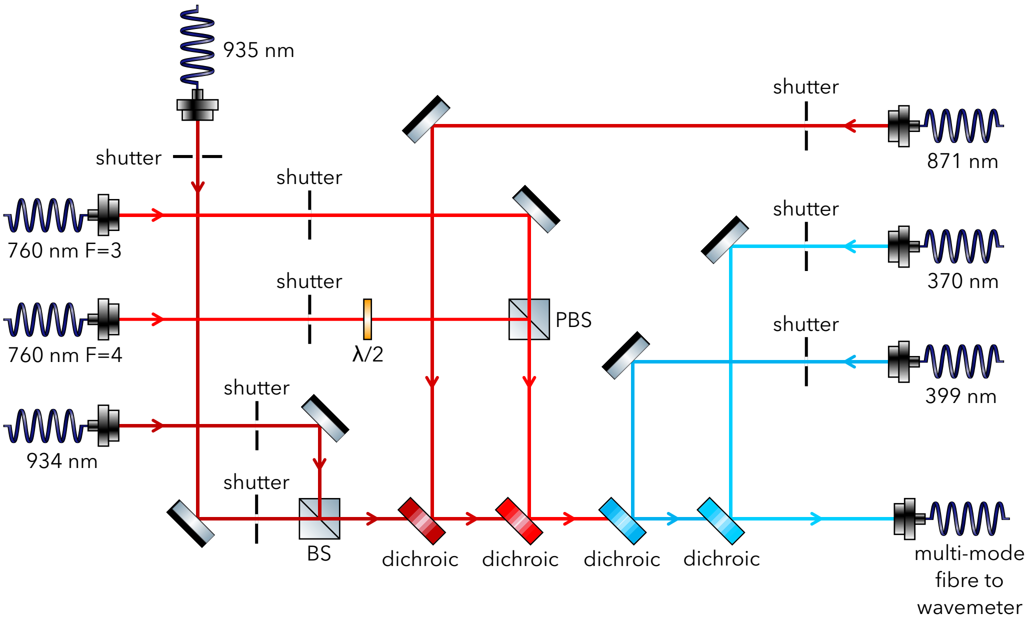

Figure 2.3: Diagram of the Wavelength Switcher setup. Fibre-coupled light from seven different wavelengths is combined with a series of dichroic mirrors into a multi-mode fibre that connects to the wavemeter.

leading to a Wavelength Switcher setup, shown in Fig. 2.3. This was a new setup, with shutters to control which individual beam is measured by the wavemeter at any one time. A series of dichroic mirrors is used to combine each wavelength into a single multi-mode fibre that connects to the wavemeter. The wavemeter is typically calibrated weekly with an internal neon-lamp.

2.2 Loading and trapping

A single ion requires an exceptionally well-controlled environment in order for one to make use of it for high-precision spectroscopy purposes. It is therefore important for the ion trap design to minimise the sensitivity to environmental perturbations that could cause unwanted noise. This section will describe the current trap and vacuum chamber design, and explain the process of loading and trapping a single ion.

2.2.1 Ion trap

The Paul trap [18] is one of the first successful experimental ion trap designs. The Laplace equation for an electric potential Φ,

$$\nabla^2\Phi = 0 \, , \tag{2.1}$$

shows that it is impossible to confine an ion in a static electric field. Instead, the Paul trap is based on a quadrupole potential created by time-varying electric fields. This quadrupole potential is expressed as [18]:

$$\Phi = \frac{\Phi_0}{2d^2}(\alpha x^2 + \beta y^2 + \gamma z^2) \, , \tag{2.2}$$

where d is a geometrical scaling parameter. The Laplace condition in Eq. (2.1) imposes that $\alpha + \beta + \gamma = 0$. In three dimensions, for a quadrupole potential generated by two end-cap electrodes, this condition is satisfied by $\alpha = \beta = 1$, $\gamma = -2$, with the following resulting trapping potential in cylindrical coordinates:

$$\Phi = \frac{\Phi_0(r^2 - 2z^2)}{2d^2} \, , \tag{2.3}$$

where the electrode separation is $2d$ and the electric potential applied to them is Φ_0. The applied potential is a combination of DC and RF:

$$\Phi_0 = U_0 + V_0 \cos \Omega t \, , \tag{2.4}$$

with $\Omega = 2\pi\nu_{\mathrm{RF}}$, where ν_{RF} is the applied RF. The motion of the ion in three dimensions $x_i = \{x, y, z\}$ with parameters $\gamma_i = \{\alpha, \beta, \gamma\}$ is described by the Mathieu equation:

$$\frac{d^2 x_i}{dt^2} + \gamma_i \frac{Q}{md^2}(U_0 + V_0 \cos \Omega t) x_i = 0 \, , \tag{2.5}$$

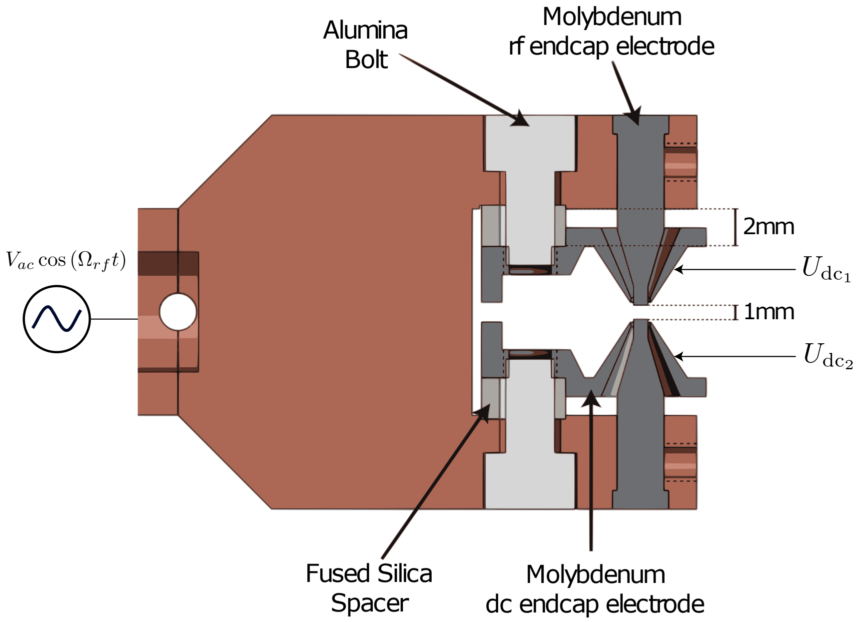

Figure 2.4: Trap cross section: RF end-cap electrodes are contained within DC electrodes, mounted in a copper support structure with alumina bolts and insulated from the RF by fused silica spacers. Diagram reproduced from Ref. [144].

where m is the mass of the ion and Q is its charge. This equation of motion will play an important part in the minimisation of the ion's micromotion in the trap, which will be discussed in more detail in section 4.1.

The trap that is currently used at NPL to trap a single ion of $^{171}\mathrm{Yb}^{+}$ was designed by Nisbet-Jones *et al.* [144] based on the end-cap trap design [145], targeting the minimisation of BBR from the trap, phonon heating of the ion, ion micromotion caused by stray electric fields, and background gas collisions. Fig. 2.4 shows a vertical cross-section of the trap. The support structure is made of oxygen-free high thermal conductivity copper. Two cylindrical end-cap electrodes with a diameter of 0.75 mm and separation of 1 mm carry the RF potential which confines the ion in all three dimensions. The RF is provided by a helical resonator and conducted by the copper support structure that the end caps are mounted in. Because electric field noise can arise from surface impurities or shape irregularities in the electrodes, they are made of 99.9 % pure molybdenum, and their flat tips are polished to a mirror finish.

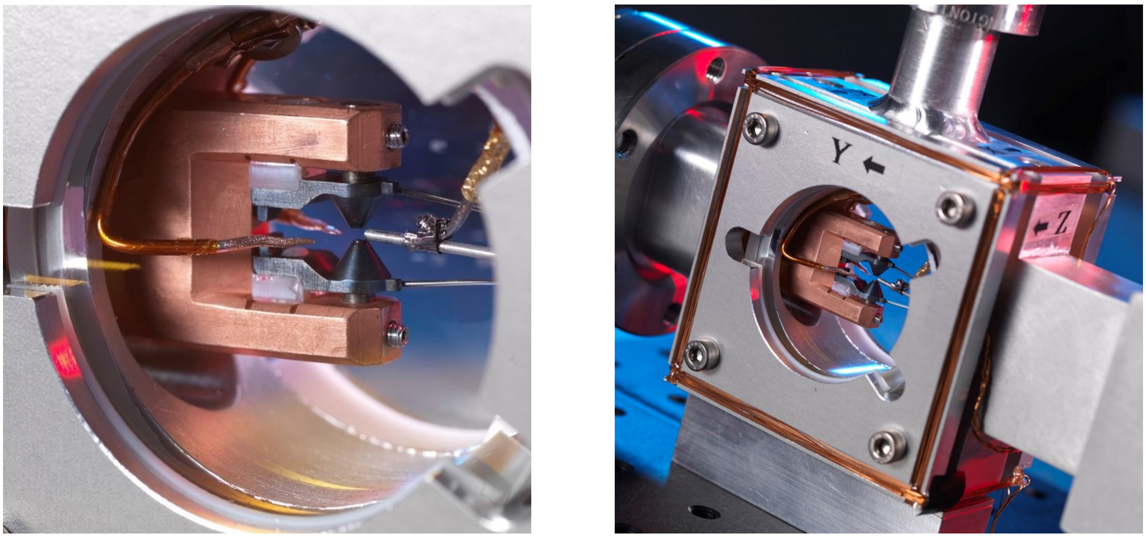

(a) (b)

Figure 2.5: Pictures of the ion trap inside the vacuum chamber.

The end-caps are contained within a pair of conical DC electrodes, also made of molybdenum, mounted in the copper support structure with alumina bolts, and insulated from the trapping RF by fused silica spacers. The gap between the RF and DC electrodes is 135 µm in the trapping region and 1 mm at the base. The asymmetric structure of the DC electrodes shields the ion from the high-voltage RF coming from the copper mount, which would otherwise distort the quadrupole potential in the trapping region.

Fig. 2.5a shows a photo of the trap that includes a few additional elements not depicted in the previous diagram, such as two compensation electrodes and an oven. The compensation electrodes, together with the pair of conical electrodes, each provide a DC voltage chosen to keep the ion in the centre of the trapping region and to minimise its micromotion. The oven consists of a tantalum tube (with an outer diameter of 1.02 mm and an inner diameter of 0.86 mm) containing enriched ytterbium, which when heated produces a collimated beam of ytterbium atoms directed towards the centre of the trapping region. A set of three orthogonal Helmholtz coils (pictured in Fig. 2.5b) is used to control the magnetic field at the ion's position. Finally, an additional coil is used to produce a magnetic field in the y direction to aid the laser-cooling process (see section 2.3).

2.2.2 Vacuum chamber

The vacuum chamber containing the trap operates at a base pressure of $\sim 1 \times 10^{-11}$ mbar. This ultra-high vacuum (UHV) environment is sustained by a SAES NEXTorr D100-5 pump, which consists of a non-evaporable getter (NEG) connected to a diode ion pump. The NEG pump is able to remove active gases (e.g. H_2, O_2, H_2O vapour) at a rate of up to 100 l/s from the vacuum chamber by trapping them in its porous cartridge and forming stable chemical compounds. The ion pump is used complementarily to pump inert gases (e.g. N_2, Ar) at a rate of 6 l/s.

Fig. 2.6 shows a diagram of the vacuum chamber geometry. The chamber is made of aluminium and has dimensions of $70 \times 70 \times 20$ mm^3. A 40-mm-diameter cylindrical opening in the centre of the chamber allows for optical access. The opening is sealed by two windows, one of which is made of UV-grade fused silica and is transparent to all the laser wavelengths required to operate the clock, while the other one is made of magnesium fluoride (MgF_2) which is transparent to wavelengths of up to 7 µm allowing the trap to be thermally imaged. The windows are sealed to the chamber via a cold-welded indium wire.

The laser wavelengths are delivered via three optical fibres whose outputs are arranged almost orthogonally, as shown in Fig. 2.6. The horizontal (H) beam comes out of the PCF

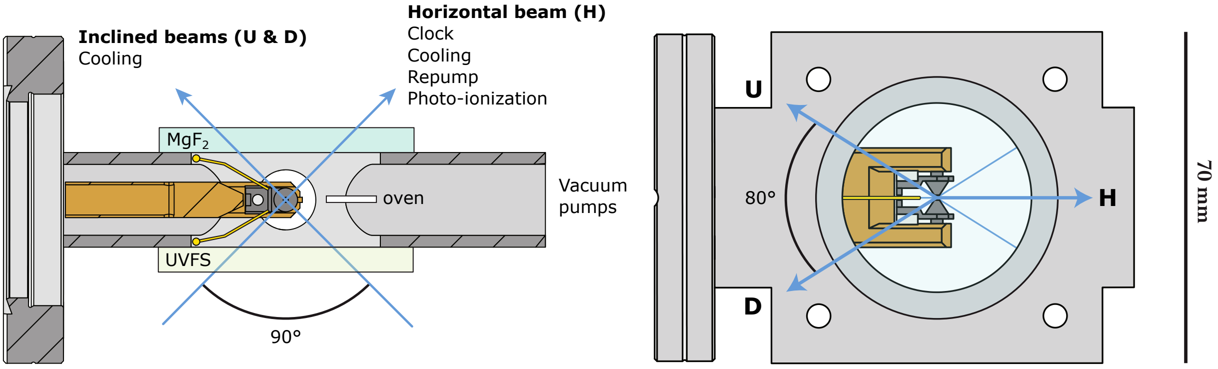

Figure 2.6: Diagram of the vacuum chamber containing the ion trap. The blue arrows indicate the paths of the three near-orthogonal laser beams. Figure reproduced from [144].

carrying all the wavelengths, which are focused by a pair of silver-coated parabolic mirrors to a waist of 19 µm at the ion's position. The other two inclined beams in the up (U) and down (D) directions are both approximately orthogonal to the H beam and carry only 370-nm cooling light. Both beams are delivered through single-mode PM fibres, which are focused to a waist of 50 µm at the ion. The fused silica window's large optical access angle enables the delivery of the H, U, D beams.

The vacuum chamber, together with all electronics and optical fibres in the trap area of the laboratory, is covered by a black foam cardboard box of dimensions $120 \times 55 \times 31$ cm^3 with an inner lining of mu-metal shielding. The box serves the purpose of shielding from both ambient light and external magnetic fields.

2.2.3 Loading an ion

In order to load a single ^{171}Yb$^+$ ion into the trap, the oven is resistively heated by running a current through wires that are connected to it via a feed-through. It is expected that the temperature rise of the oven during loading is of the order of 100 K. While the oven is hot, a collimated beam of isotopically-enriched ^{171}Yb passes through the centre of the trap, where 399-nm and 370-nm light from the H beam photo-ionise the atoms. With typical operating powers of the two lasers ($\sim$ 10 µW of 399 power and $\sim$ 1 µW of 370 power at the ion) and an oven current of approximately 5 A, a single ion is loaded on average 120 s after the oven started firing. The setup for the 399-nm laser is described in Appendix A.3.

To capture and trap the ion, a frequency of $\Omega = 2\pi \times 13.7$ MHz with an amplitude of 100 mV (corresponding to 150 mW of forward power) further increased by an amplifier is applied to the helical resonator matching its resonant frequency. This in turn provides the RF for the end-cap electrodes to produce the quadrupole potential in which the ion is captured. After loading, the amplitude of the RF drive is increased to up to 150 mV (500 mW), making the trap deeper in favour of ion retention.

2.3 Cooling

The RF trapping potential is fully responsible for the confinement of the ion in the trap, and thus the ion can remain trapped without being laser-cooled. In fact, an uncooled ion has been observed to remain in the trap for periods of up to 45 hours. However, Doppler cooling [146–148] is an essential requirement for performing clock operations, as not only this would ensure much smaller temperature-dependent systematic shifts, but also because the ion's fluorescence as a result of its cooling is used to determine the state that the ion is in.

The ion is Doppler-cooled by shining 370-nm laser light in the H, U and D directions with a frequency red-detuned to the cooling transition ${}^2\mathrm{S}_{1/2}(F = 1) \rightarrow {}^2\mathrm{P}_{1/2}(F = 0)$. If the ion's momentum is in the opposite direction to that of the red-detuned light, the Doppler effect causes the ion to see the light as blue-shifted, bringing the effective frequency back to resonance such that the ion can absorb the photons, with a rate that is dependent on the ion's opposing velocity. To decay back to the ground state, the ion re-emits the absorbed photon in a random direction, meaning that over time its net momentum averages to zero.

It must be noted that for a constant polarisation of the 370-nm beam driving the ${}^2\mathrm{S}_{1/2}\,(F = 1) \rightarrow {}^2\mathrm{P}_{1/2}\,(F = 0)$ cooling transition, the ion would be optically pumped into a dark state, which depending on the polarisation would be a superposition of the $m_F = 0, \pm 1$ sublevels. For this reason, the cooling process is aided by a large applied magnetic field of ~ 300 µT for the destabilisation of the dark states [149], leading to an increase in the population of the excited state, and thus an increase in the cooling rate. The magnetic field must be applied at an oblique angle to the linear polarisation of the 370-nm beam, setting the ion's quantisation axis parallel to the field. In our setup, the magnetic field is entirely in the y direction of the laboratory-defined axis, which is at an angle of 32° from the H-beam, and is applied by the additional y-coil.

As explained in section 2.1, the 935-nm repump laser is essential for the ion to re-enter its cooling cycle after being excited to the $^2\mathrm{P}_{1/2}(F = 0)$ state. The spontaneous emission of the 370-nm photons during the cooling process is manifested as ion fluorescence, which is the metric used to detect the state of the ion. A portion of the photons emitted by the ion are collected through the vacuum chamber's fused silica window and focused into a photo-multiplier tube[5] (PMT). Fig. 2.7 shows the dependence of the ion's fluorescence on the frequency detuning from the centre of the cooling transition line. The sharp dip in fluorescence at the line centre and the consequent lack of fluorescence indicates that the ion is no longer being cooled, and instead it is being heated up by the blue-detuned light.

---

[5] Sens-Tech P25PC

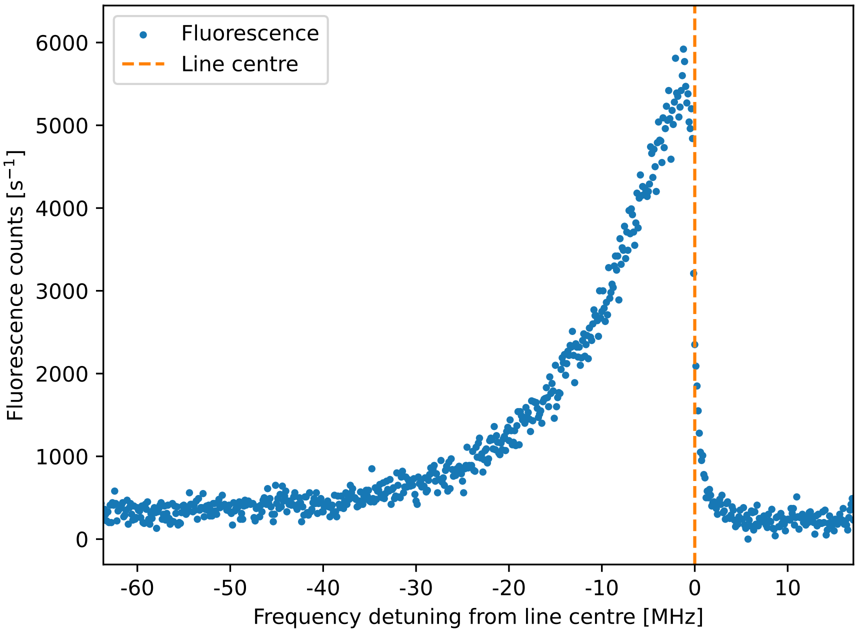

Figure 2.7: Line shape of the ion's cooling transition. The ion fluorescence signal is visible and increases as the red-detuned frequency approaches the line centre, at which point it dips down as the ion starts to be heated up by blue-detuned light.

2.3.1 370-nm laser setup for cooling

The laser setup of the 370-nm system is shown in Fig. 2.8. A Toptica DL Pro external-cavity diode-laser (ECDL) with a Nichia diode outputs 369.5-nm light which is locked to a cavity via the top-of-fringe "Lock-in" method. The cavity transmission is measured by an amplified photodiode[6], whose signal is fed to the Toptica DLC Pro laser controller. The laser grating piezo is continuously scanned over a voltage range producing a cavity transmission peak. In order to keep the laser locked to the peak of the transmission, the derivative of this signal is obtained by demodulating the photodiode signal with the same frequency as the laser frequency modulation input. The derivative signal, which approaches zero at the centre of the resonance with a different sign on either side, allows the diode current to be adjusted in the right direction to keep the laser in lock.

The locking cavity, designed at NPL, is a piezo-tunable low-drift Fabry-Pérot cavity consisting of two concave mirrors separated by a 100-mm long spacer made of ultra-low expansivity (ULE) glass, which makes it extremely insensitive to thermal changes. The glass's coefficient of thermal expansion (CTE) is around 10^{-8} K^{-1} at room temperature. The free spectral range of the cavity is 1630 MHz. The cavity is placed in a vacuum casing and is kept at a pressure of $< 10^{-6}$ mbar. A temperature-controlled copper sheet and an additional layer of insulation separate the vacuum chamber from an external aluminium casing. The same cavity design is also used to lock the 935-nm laser.

The wavelength of the light is measured by the wavemeter thanks to a pick-off that allows a small portion of light to be coupled into a fibre leading to the Wavelength Switcher. Once the laser is locked to the right mode with the aid of the wavemeter, its frequency is adjusted at the MHz level by varying a high-voltage piezo controller[7] that alters the length of the cavity. This fine adjustment is (infrequently) done such that the amplitude of the ion's fluorescence signal is at the FWHM of the cooling transition line from Fig. 2.7.

---

[6] Thorlabs PDA36A-EC

[7] Thorlabs MDT693A

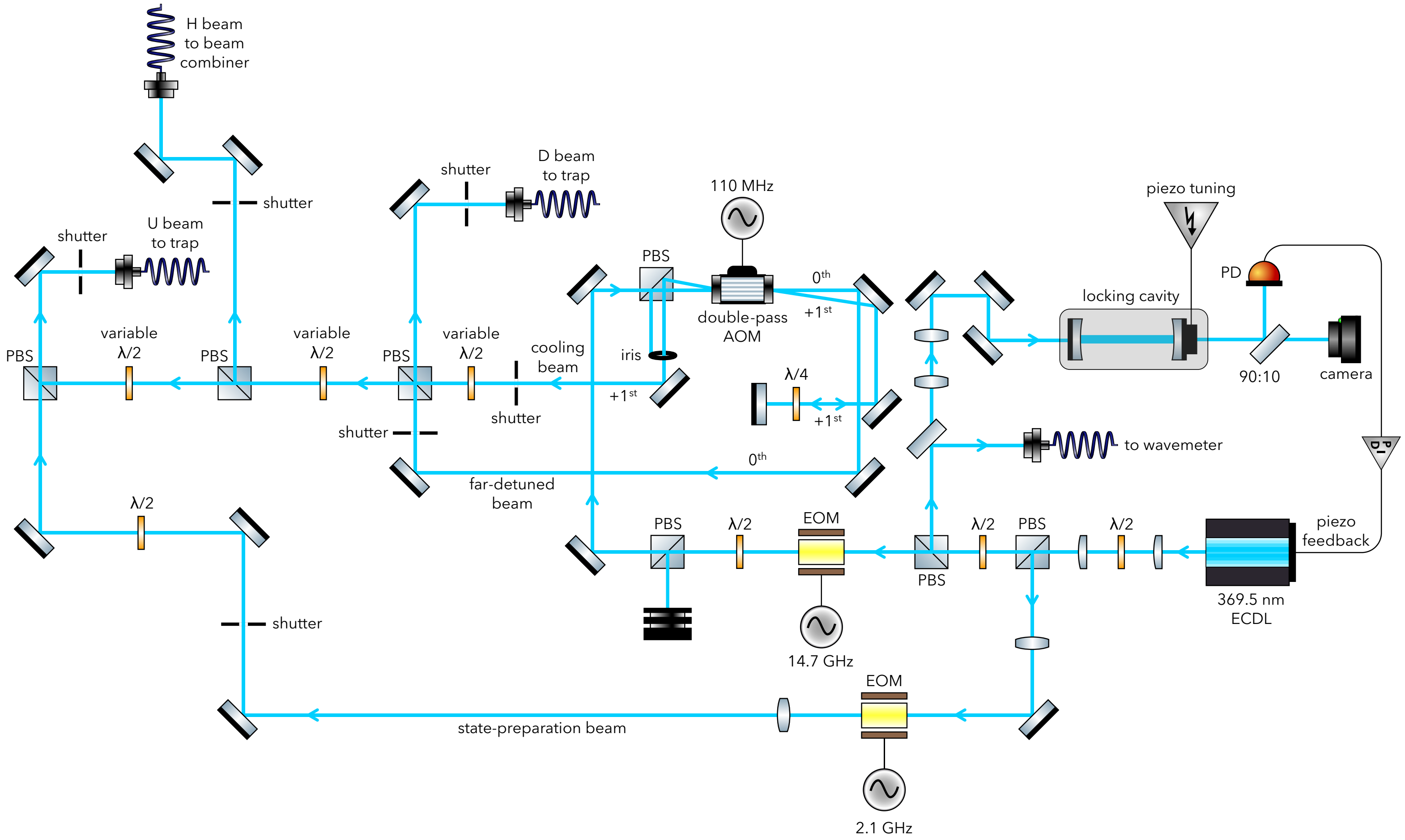

Figure 2.8: Diagram of the 370-nm cooling laser setup. The light from a 369.5-nm diode laser is locked to an external cavity via the top-of-fringe locking method. The cooling light is split into the three H, U, D beams by variable half-wave plates, which are then coupled into PM fibres.

The 14.7-GHz beam[8] passes through an acousto-optic modulator[9] (AOM) which allows the frequency and the power of the cooling light to be controlled by the computer. The light is then split into the three H, U, D beams via half-wave plates on homemade computer-controlled rotation mounts, enabling a custom split of power between the three beams. Each beam is coupled into a PM fibre, and while the U- and D-beam fibres lead straight to the trap, the H-beam fibre outputs its light at the Beam Combiner. The far-detuned beam, which is only used during ion loading to provide some extra 370-nm power, is coupled into the D-beam fibre, while the state-preparation beam[10] is coupled into the U-beam fibre.

2.3.2 Detecting a single ion

A high level of fluorescence indicates that one or more ions are present in the trap. In order to determine the precise number of ions, the technique of electron shelving [5] is used. While the ion is being cooled, the -3.06 GHz sideband on the 935-nm beam is turned off to shelve the ion in the $^2\mathrm{D}_{3/2}\,(F=2)$ state for the duration of its lifetime, until it naturally decays back to the $^2\mathrm{S}_{1/2}$ state re-entering the cooling cycle. The ion fluoresces while it is cooled, whereas it appears dark when it is shelved. Both the off-resonant excitation to the upper state and the decay to the ground state occur approximately every 50 ms, making a very clear distinction between bright and dark states.

By measuring the fluorescence for a suitable amount of time, a histogram can be plotted as in Fig. 2.9 with the blue/circle bars showing two distinct peaks for the two possible fluorescence levels of a single ion, dark and bright. If instead there were two ions in the trap, either one or both ions can be observed fluorescing in the ground state, leading to an additional peak at roughly double the counts/s of the single ion's fluorescence as shown by the orange/line bars in Fig. 2.9.

---

[8] The 14.7-GHz sideband is applied by a QUBIG EO-WG14.7M2 EOM

[9] Isomet 1206C-2-1002

[10] The 2.1-GHz sideband is applied by a New Focus 4431 EOM

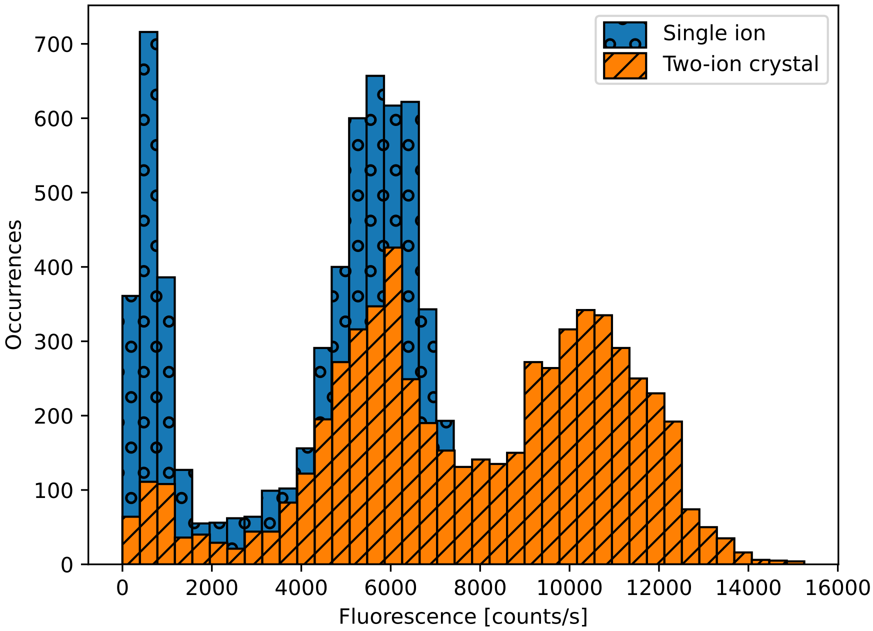

Figure 2.9: Fluorescence histogram for a single ion and for a two-ion crystal in the trap. For a single ion, the first peak represents the background counts in the dark state, while the second peak represents the ion fluorescing. For two ions, the three peaks correspond respectively to zero, one and two ions fluorescing. The amplitude of the fluorescence peaks is halved as the number of fluorescence states the ions can be in is doubled.

While the ion fluorescence is measured by a PMT for all clock operations, an EMCCD camera[11] is installed on the other side of the vacuum chamber to image the ion through the MgF_2 window for diagnostic purposes. Figs. 2.10a, 2.10b and 2.10c show images of respectively a single ion, a two-ion crystal and a cloud of ions in the trap. Multiple ions can be loaded into the trap if the power of the 399-nm beam is too high, if the oven current is too high, or if the frequency of the 370-nm laser is too red-detuned.

To understand the true scale of this experiment, Fig. 2.11 shows a picture of a single trapped $^{171}Yb^+$ ion between the two conical electrodes, whose distance between each other is 1 mm. While the single ion is visible thanks to its own emitted fluorescence, the electrodes are made visible by the 370-nm cooling light scattering off them.

---

[11] Andor iXon Ultra 897

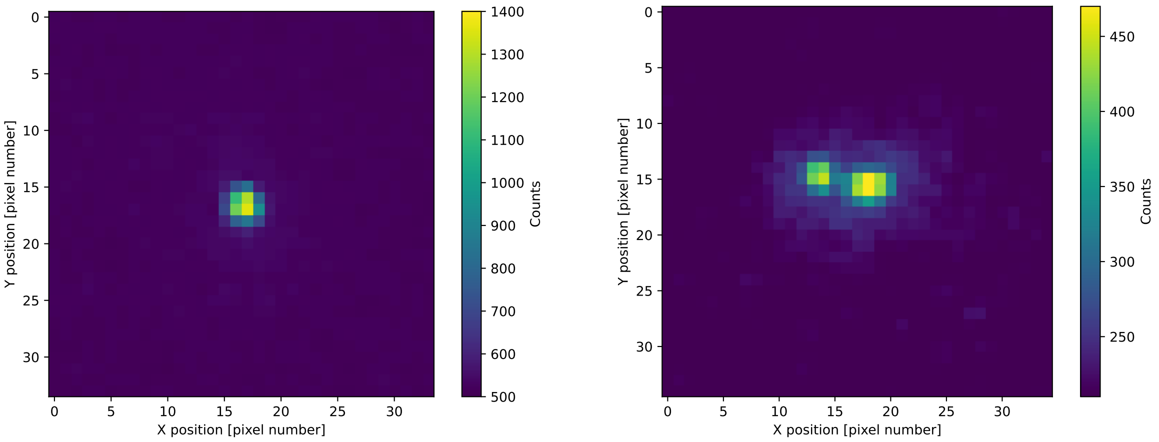

(a) A single ion[12]

(b) A two-ion crystal.

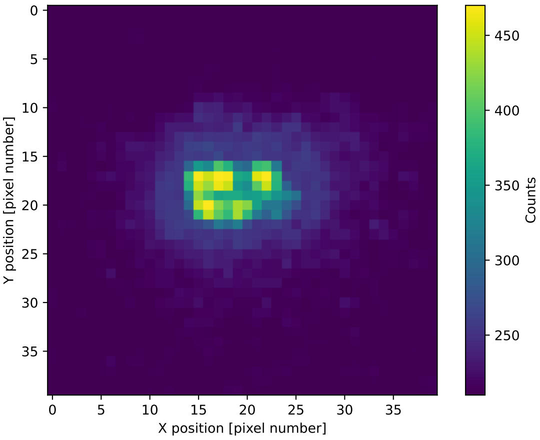

(c) A cloud of ions.

Figure 2.10: Images from the EMCCD camera of one or multiple ions in the trap. The pixel size is approximately 2.5 × 2.5 µm.

---

[12] The difference in colourbar scale in Fig. 2.10a compared to Figs. 2.10b and 2.10c is due to it having been taken at a different time than the other two, therefore with different camera settings and/or a different level of fluorescence.

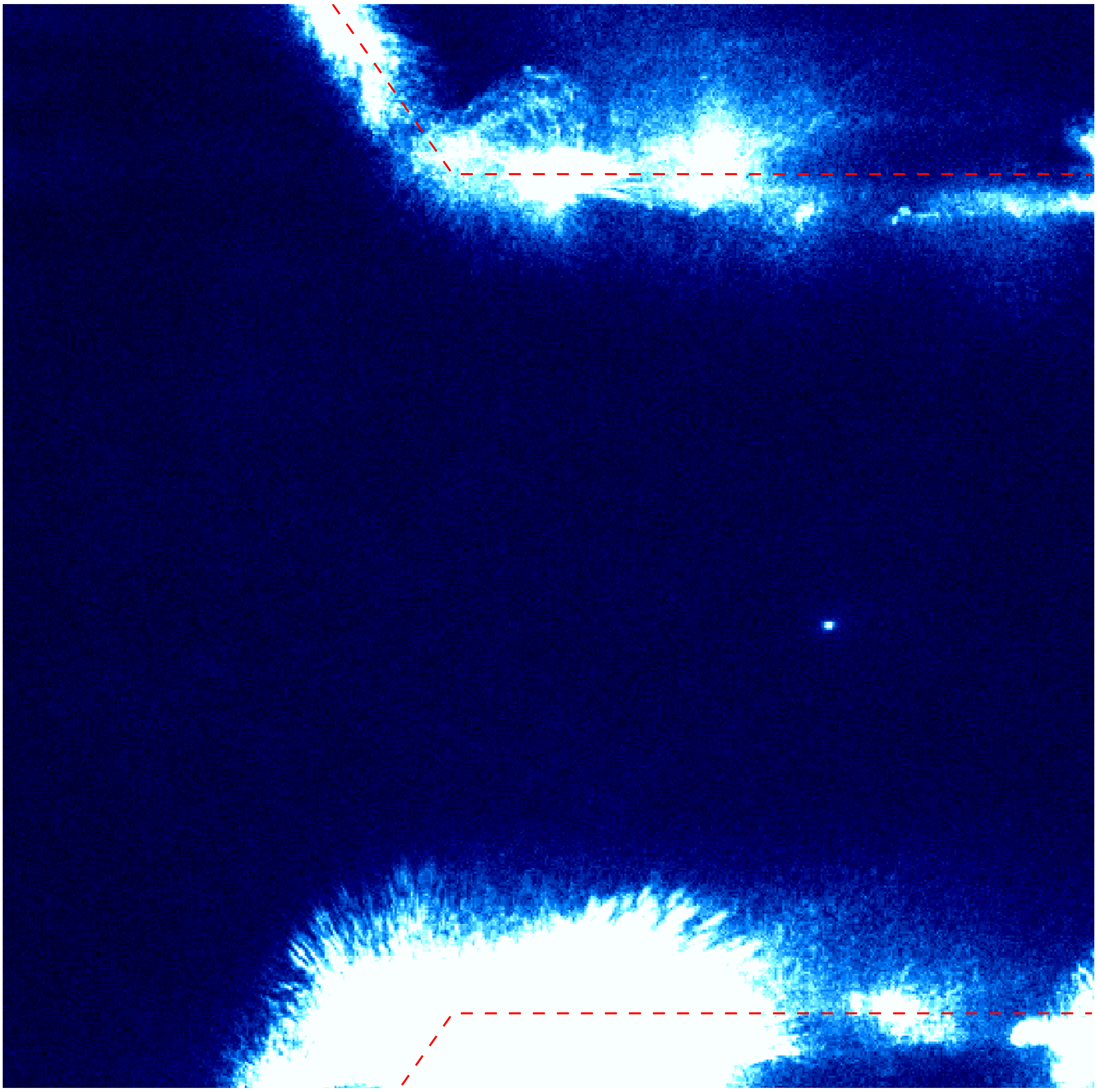

Figure 2.11: Image (512 × 512) taken with the EMCCD camera of a single ion in between the trap electrodes. 370-nm scatter makes the conical electrodes visible, and their position is indicated with the red dashed lines. The distance between the electrodes is 1 mm.

2.4 Probing the clock transition

With an ion that is trapped and cooled, it is now possible to probe one of the two clock transitions. Both clock beams at 436 and 467 nm are frequency-doubled from infrared (IR) lasers at 871 and 934 nm respectively. There are several reasons why this is the case. Firstly, at the time of the development of the optical clock system, laser technology was not sufficiently developed to generate the blue wavelengths directly. Secondly, the frequency of the clock light is measured by a frequency comb which spans IR wavelengths. Finally, the optical cavities which the lasers are locked to are typically higher-performing for IR wavelengths.

The two IR clock laser setups are extremely robust systems that very rarely require any adjustment or modifications. For this reason, they can essentially be treated as black boxes, allowing for a greater focus on the frequency-doubled light that actually probes the ion. Appendices A.4 and A.5 describe the two clock laser setups in detail, while section 2.5 will focus on how the IR light is frequency-stabilised and measured.

2.4.1 467-nm laser setup for probing the E3

Fig. 2.12 shows the optical setup for the 467-nm beam. The residual IR light after the doubler is measured by a homemade photodiode for path length stabilisation (PLS), consisting of an asymmetric Michelson interferometer setup. The rest of the IR light is then split and sent to be measured by the two frequency combs. The blue light passes through an AOM, referred to as the phase AOM, which is used for the phase noise cancellation in the 467-nm beam. The light is then coupled into a fibre that leads to the Beam Combiner. Fig. 2.2 shows the optical components in the 467-nm beam. The light passes through the 467 clock AOM, and while the $+1^{\text{st}}$ order is selected to couple into the PCF and probe the ion, the 0^{th} is retro-reflected and used for PLS.

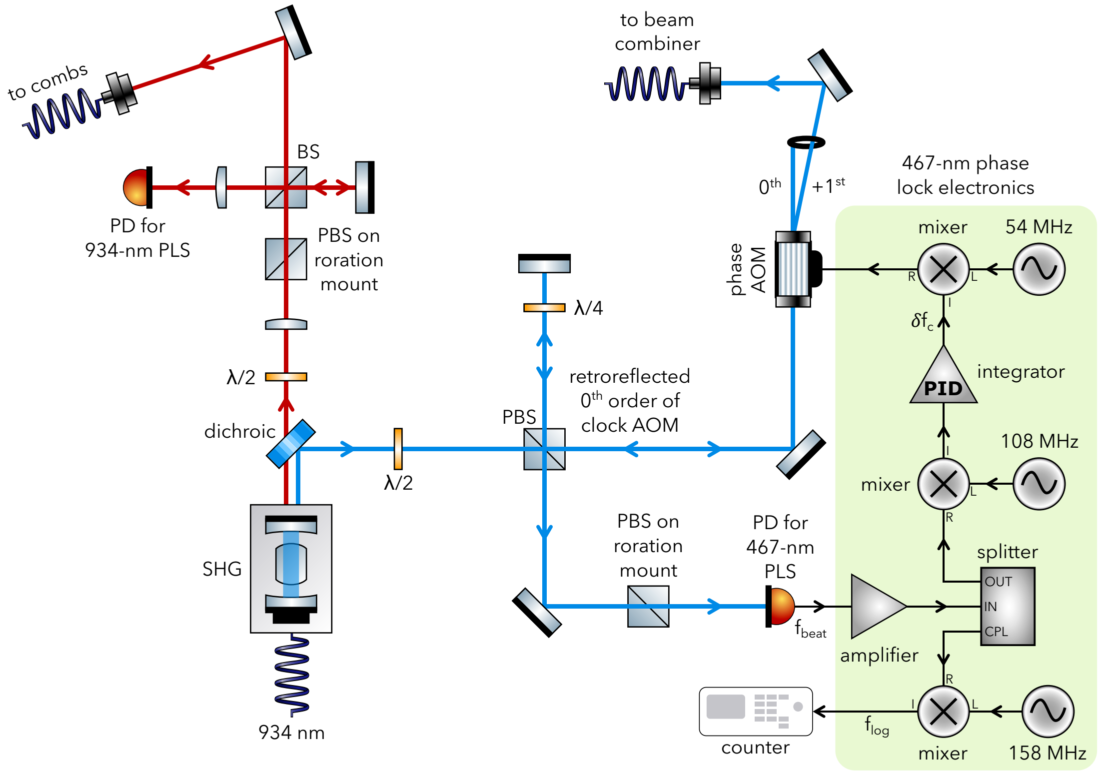

Figure 2.12: Diagram of the 467-nm laser setup for probing the E3 transition. The blue light passes through the phase AOM and gets coupled and sent to the Beam Combiner. The retro-reflected 0th order of the clock AOM at the Beam Combiner is beat against the incoming 467-nm beam for phase noise cancellation.

The beat frequency f_{beat} between the two colinear beams is measured by a photodiode[13]. The electronic components in the green section of Fig. 2.12 are set up for the phase noise cancellation in the 467-nm beam. The photodiode beat signal is split into two: one signal is logged by a frequency counter, while the other is sent to an integrator which outputs a correction δf_c to drive the error signal to zero. This frequency is then combined with a reference frequency of 54 MHz to drive the 467 phase AOM. Note that in the 436-nm optical setup (described in Appendix A.6) there is currently no phase AOM in place, and therefore the phase noise is not yet accounted for.

---

[13] Thorlabs PDA015A/M

2.4.2 Choosing the probe power and probe duration

The clock transition is probed with a Rabi π-pulse, and the optimal probe duration and power required to achieve this is determined by Rabi-flopping. Fig. 2.13 shows a plot of the excitation of the E3 transition, at a constant arbitrary power, as a function of probe duration. The probe time corresponding to the first peak would then be selected to operate at for maximal excitation. It can be seen that as the probe time increases, the Rabi oscillations are damped and flatten out at around 50% excitation. This is the result of the ion's temperature causing it to be in a superposition of vibrational levels in the harmonic trap, and transitions from each vibrational level having slightly different Rabi frequencies [150]. The rate of damping of the oscillations is therefore determined by the motional heating rate of the ion in the trap.

Rabi-flopping can also be useful to choose the optimal probe power for a desired probe time. Because the QPN is inversely proportional to the probe time, it is beneficial to

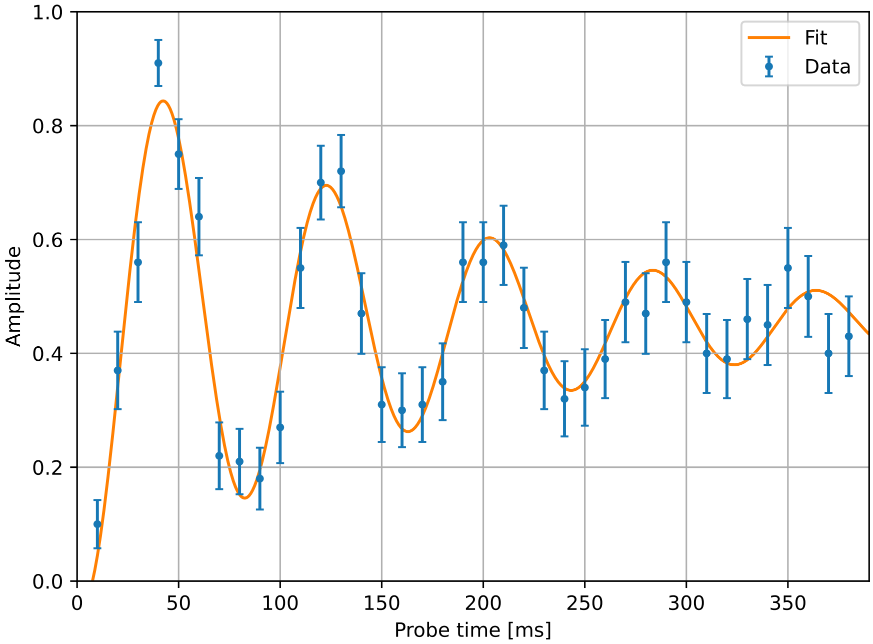

Figure 2.13: Rabi-flopping at a constant probe power and varying probe duration.

choose a long probe time to improve the frequency stability. However, since the ion is not being cooled during a clock probe, the pulse duration is typically limited by the trap heating rate. Furthermore, the coherence time of the probe light is also a limiting factor for the pulse duration. The combination of these effects would be observed by a faster rate of decoherence in the Rabi oscillations and a lower π-pulse amplitude. Therefore, a good balance must be reached to probe a coherent π-pulse with a high amplitude and for a long enough duration.

2.4.3 Clock probe sequence

A clock cycle is composed of six stages: cooling, state preparation, pre-probe delay, probe, readout, and repumping. The beams that shine on the ion during each stage are controlled by the shutters in the Beam Combiner setup (Fig. 2.2), with exception of the 370-nm cooling and state-preparation beams which are controlled by the shutters in the 370-nm laser setup (Fig. 2.8).

During the probe sequence, a particular magnetic field direction combined with a clock-beam polarisation direction is chosen to maximise the excitation of the clock transition. This magnetic field has a magnitude of 3 µT, which is small enough not to cause large magnetic-field shifts, and big enough to align the ion's quantisation axis in a defined direction. This magnetic field is permanently on, generated by currents running through the set of three orthogonal coils surrounding the vacuum chamber.

Cooling For the first 10 ms of the sequence, the ion is cooled by the three H, U, D beams, carrying the 370-nm light with the 14.7-GHz sideband. The power of each beam is chosen by a combination of half-wave plate positions for which cooling is optimised, targeting 2000 counts/s of fluorescence in the H beam and 100 counts/s in the U and D beams combined.

State preparation The 14.7-GHz cooling beam is turned off, and the state-preparation beam with the 2.1 GHz sideband addressing the $^2\mathrm{S}_{1/2}(F=1) \rightarrow \mathrm{P}_{1/2}(F=1)$ transition is turned on for 10 ms, allowing the ion to decay to the $^2\mathrm{S}_{1/2}(F=0)$ state, pumping the population to the required state to undergo a clock transition.

Pre-probe delay Before probing the clock transition, all the beams and the large magnetic field in the y direction that aids the cooling cycle are turned off for 25 ms. This delay ensures that all shutters will have closed by the start of the clock probe, as this must be the only light shining on the ion during that stage of the sequence. While 25 ms is plenty of time for the shutters to close (these typically take < 5 ms to close), this relatively long delay allows the coil current generating the large magnetic field to completely decay.

Probe The shutter in the clock beam is then opened, and the clock AOM is turned on and left on for the duration of the probe pulse. Typical pulse durations for the E3 transition are 400-650 ms, requiring hundreds of µW of optical power in the 467-nm beam for a π-pulse. For the E2 transition, with an upper-state lifetime just above 50 ms, pulse durations between 10-50 ms have been used, with 436-nm beam powers < 1 nW. A delay of 3 ms is applied between the shutter opening and the AOM turning on to ensure that the shutter has fully opened before the beginning of the probe pulse.

Readout In order to detect the state of the ion without affecting it, the large magnetic field and all beams are turned back on apart from the relevant beam that would repump the ion out of the clock state (935-nm $F=2$ for the E2, 760-nm $F=3$ for the E3). In this way, if the ion had remained in the ground state upon an unsuccessful excitation, it would re-enter the cooling cycle and emit fluorescence. On the other hand, if the ion had been successfully excited to the clock state, the ion would appear dark. This is referred to as a quantum jump. The duration of the readout stage is typically 10 ms, during which ~ 20 photons are detected.

Repumping Finally, the relevant repump beam is turned on such that if the ion had been excited to the clock state, it would be able to re-enter the cooling cycle and undergo the next clock sequence. The repump stage duration is 10 ms.

While the state of each shutter matches exactly with the beams received by the ion during a given stage, the AOMs required for a particular clock sequence are kept on for as long possible. The reason for this is that the thermal effects of the AOMs turning on and off are significant and would lead to drifting fibre-coupled beam powers affecting the accuracy of the measurement. For this reason, the 370-nm AOM is kept on for the entirety of the clock sequence, with only the cooling-beam and state-preparation shutters (see Fig. 2.8) controlling when and which 370-nm beams the ion sees during each stage.

The clock AOM is left on during the cooling, state-preparation, pre-probe delay and repumping stages, with the clock-beam shutter blocking the beam from reaching the ion. The AOM is turned off just after the pre-probe delay, such that it can be turned on for the probe after the clock-beam shutter has opened. This allows the timing of the pulse to fully rely on the timing of the AOM rather than the shutter. The AOM is then turned off at the end of the pulse, and turned back on after the readout stage has been completed.

2.4.4 Algorithm for locking the probe light to the clock transition

It is in the nature of clock measurements to gather a large number of data points in order to reach a high level of frequency stability. The complication that arises in making repeated measurements is that the clock lasers are locked to a cavity whose length can slowly drift over time as a result of thermal expansion or material creep deformation. This means that the AOM frequency required to probe the clock transition would need to be continuously changing. Even though the ultrastable cavity has an extremely low drift rate (of the order of 10^{-4} Hz/s), this is still significant for Fourier-limited transition linewidths of 1 Hz and 15 Hz for the E3 and E2 respectively over continuous measurement periods of several hours.

A locking algorithm is therefore used to keep the probe light locked to the clock transition. This is implemented by applying a series of alternating probes on the high and low frequency sides of the FWHM of the transition. These are referred to as probing on the *right* and *left*. Any asymmetry in the excitation would give information on the direction of the cavity drift, such that a new estimate of the probe frequency can be made. The clock AOM is placed in this feedback loop: the RF signal driving it is responsible for applying the appropriate frequency in each probe pulse.

A single servo cycle i, during which the frequency of the clock transition is assumed to be f_i, consists of four pairs of right and left probes at a frequency of $f = f_0 \pm \mathrm{FWHM}/2$. For the minimisation of sensitivity to the cavity's low-frequency noise, the probes are interleaved with a Thue-Morse sequence [151]. For a sequence of $N = 8$ probes, the right and left pulses are interleaved as shown in Fig. 2.14.

At the end of the eight probes, the number of jumps that occurred on the right (n_i^{right})

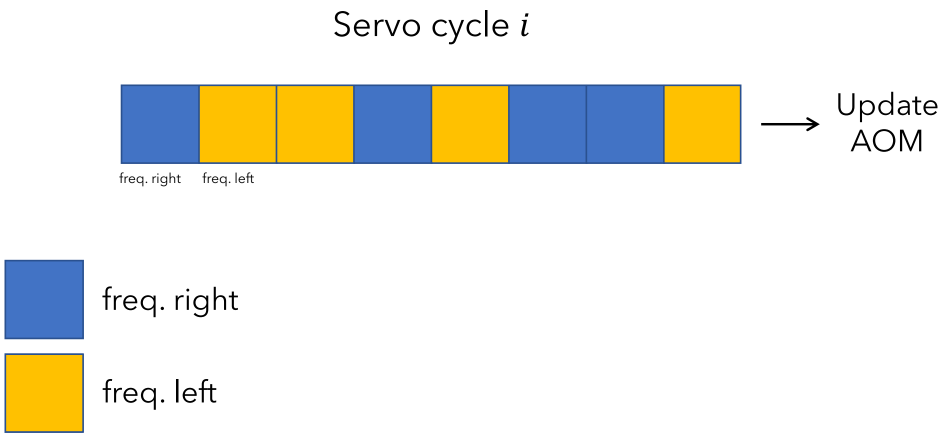

Figure 2.14: Interleaved pulse sequence for a single-servo lock. Blue and yellow squares represent right and left frequencies respectively (i.e. $f_i \pm \mathrm{FWHM}/2$)

and on the left (n_i^{left}) of the transition are counted, and the error signal is calculated as:

$$e_i = \frac{2(n_i^{\text{right}} - n_i^{\text{left}})}{N} \ . \tag{2.6}$$

The error signal would be zero when on resonance with the transition. The new best guess of the centre frequency that should be used in the next servo cycle $i+1$ can be then calculated as:

$$f_{i+1} = f_i + \text{FWHM}\left(G_1 e_i + G_2 \Delta t_i \sum_{j=0}^{i} e_j\right) \ , \tag{2.7}$$

where Δt_i is the duration of the i^{th} servo cycle, and G_1 and G_2 are set constants that behave respectively as a first and second integral gain in a PID servo.

A complication arises when probing specifically the E3. The optical power required to probe this transition leads to a probe-induced AC Stark shift proportional to the laser intensity $\langle \mathbf{E}^2 \rangle$. This effect is negligible for the E2 given the extremely low power required to drive it, however this shift can be several Hz large for the E3, which is problematic when targeting a mHz-level measurement accuracy. For this reason, a dual-servo locking algorithm is employed, in which two interleaved single servos are run at two different power levels P_1 and P_2. As these would produce different AC Stark shifts, resulting in different frequencies f_1 and f_2, the unperturbed frequency f_0 can be extrapolated:

$$f_0 = f_2 - \frac{R}{R-1}(f_2 - f_1) \ , \tag{2.8}$$

where $R = P_2/P_1$ and $P_1 < P_2$. The two low (L) and high (H) power servos are interleaved with the sequence HLHLHLHL, which is flipped to LHLHLHLH every other servo cycle. The full series of high/low power and left/right frequency pulses is shown in Fig. 2.15. If the stability on the individual servo frequencies f_1 and f_2 are respectively σ_1 and σ_2, the instability on the extrapolated frequency is calculated as:

$$\sigma_{\text{extr.}}^2 = \frac{R^2}{(R-1)^2}\sigma_1^2 + \frac{1}{(R-1)^2}\sigma_2^2 \ . \tag{2.9}$$

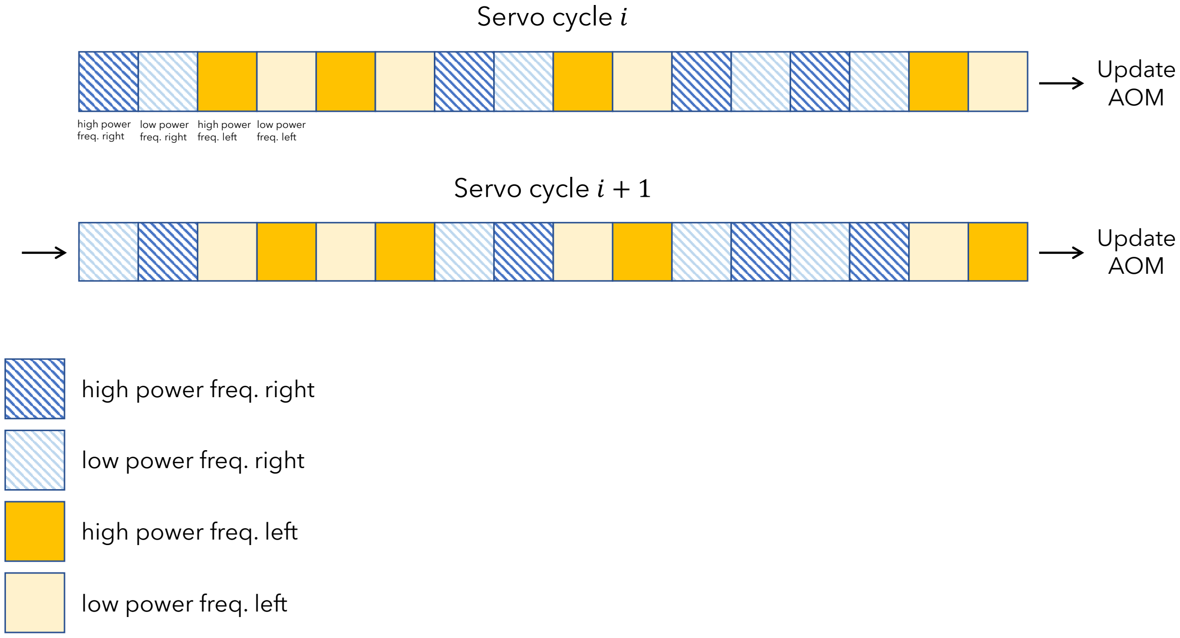

Figure 2.15: Interleaved pulse sequence for a dual-servo lock. Striped blue and solid yellow squares represent right and left frequencies respectively (i.e. $f_i \pm \mathrm{FWHM}/2$), and dark and light colours represent high and low power pulses respectively.

2.4.5 Power servo for the 467-nm light

A power servo is used to power-stabilise the beam. The power-servo setup is shown in Fig. 2.16. After probing the ion and passing through the vacuum chamber windows, the 467-nm light is split into two beams. The power of one beam is continuously monitored by an out-of-loop (OOL) photodiode. The other beam is measured by an in-loop (IL) photodiode[14] with 70 dB gain. The IL photodiode's voltage output V_{IL} is connected to a voltage differencer board which takes as a second input a chosen reference voltage V_{ref}. The subtracted signal $V_{\mathrm{out}} = V_{\mathrm{IL}} - V_{\mathrm{ref}}$ is fed to an integrator with bandwidth ≤ 500 kHz which makes a small correction δV_{c} to drive the input error signal to 0 V. The output of

---

[14] Thorlabs PDA36A-EC

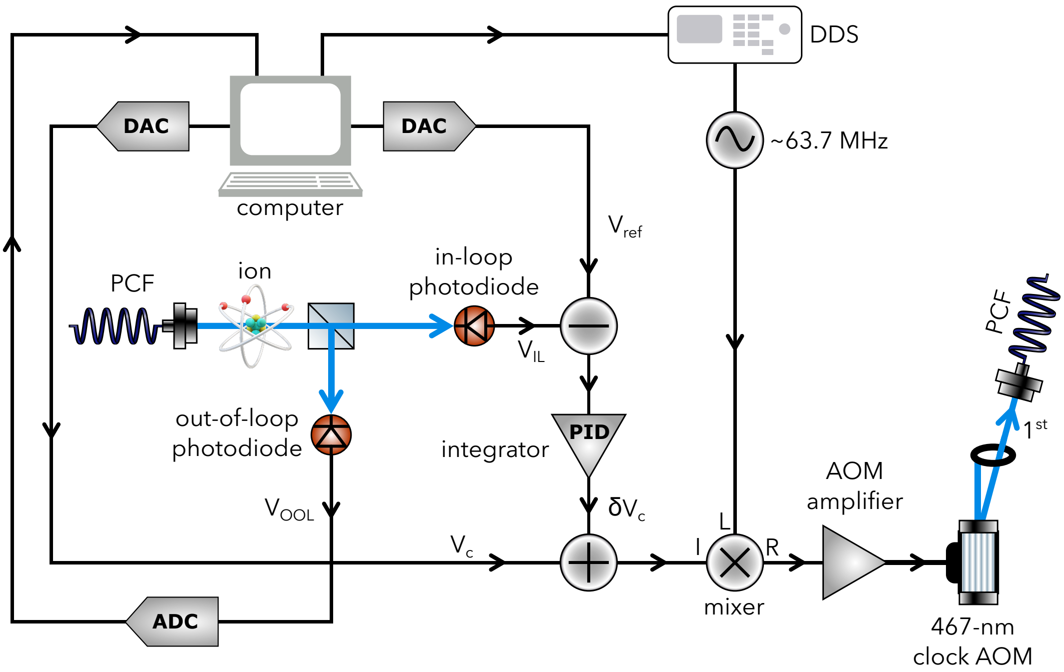

Figure 2.16: Diagram of the power servo setup to stabilise the power of the 467-nm beam.

the integrator is added up with another constant DC signal V_c and sent to a mixer which is used to set the appropriate attenuation to the RF signal driving the 467-nm clock AOM. Since the integrator range is very limited, the initial attenuation applied to the RF signal before being mixed with the integrator correction needs to be appropriately chosen such that the required δV_c falls within the integrator's range.

2.5 Stabilising and measuring the optical frequency

A multi-branched erbium-doped fibre optical frequency comb in a neighbouring laboratory plays a part in both the stabilisation and the measurement of the frequency of the light that probes the clock transition. A second frequency comb in another nearby laboratory is also used to directly measure the frequency of the clock lasers as a check of the first comb's performance, verifying that the latter does not introduce any measurement offset or excess noise. Both frequency combs are referenced to a 10 MHz signal coming from the hydrogen maser that generates the local timescale UTC(NPL). While the following subsections will focus on the E3 transition and the stabilisation and measurement of 934-nm light, it must be noted that the setup in place for the 871-nm light is almost equivalent.

2.5.1 934-nm clock laser stabilisation

Fig. 2.17 shows the E3 optical clock system in its entirety, with the ion as the reference, the 934-nm laser as the oscillator, and the frequency comb as the counter. The frequency of the 934-nm light is stabilised in two stages. The first stage is a Pound-Drever-Hall (PDH) lock [152] to the local cavity, which works as follows. An EOM produces two sidebands far from resonance at frequencies $\omega_0 \pm \omega_m$, where ω_0 is the carrier frequency. The three components ω_0, $(\omega_0 \pm \omega_m)$ are then reflected from the cavity, incurring different reflection coefficients $R(\omega_0)$ according to their detuning from the cavity's resonant frequency:

$$E_{\text{ref}} = R(\omega) E_{\text{in}} \ , \tag{2.10}$$

with E_{ref} and E_{in} being the complex amplitudes of the reflected and incident beams respectively. The complex reflection coefficient $R(\omega)$ represents the phase offset that the beam acquires after being reflected. The interference of the two sidebands with the carrier beam results in a beat at the EOM's modulation frequency ω_m. If the laser were exactly on resonance with the cavity, the two beat notes would be out of phase by 180°, resulting in total destructive interference. However, if it were slightly off resonance, a small error signal would be detected by a photodiode and fed to an integrator, which would apply the necessary correction to steer the laser back on resonance.

The second stage of frequency stabilisation occurs in a separate nearby laboratory. A 1064-nm laser is locked to an ultrastable cavity. The cylindrical cavity spacer, made of ULE glass, has an outer diameter of 10 cm and length of 48.5 cm. The cavity is operated at room temperature and is placed in a vacuum system mounted on a vibration isolation

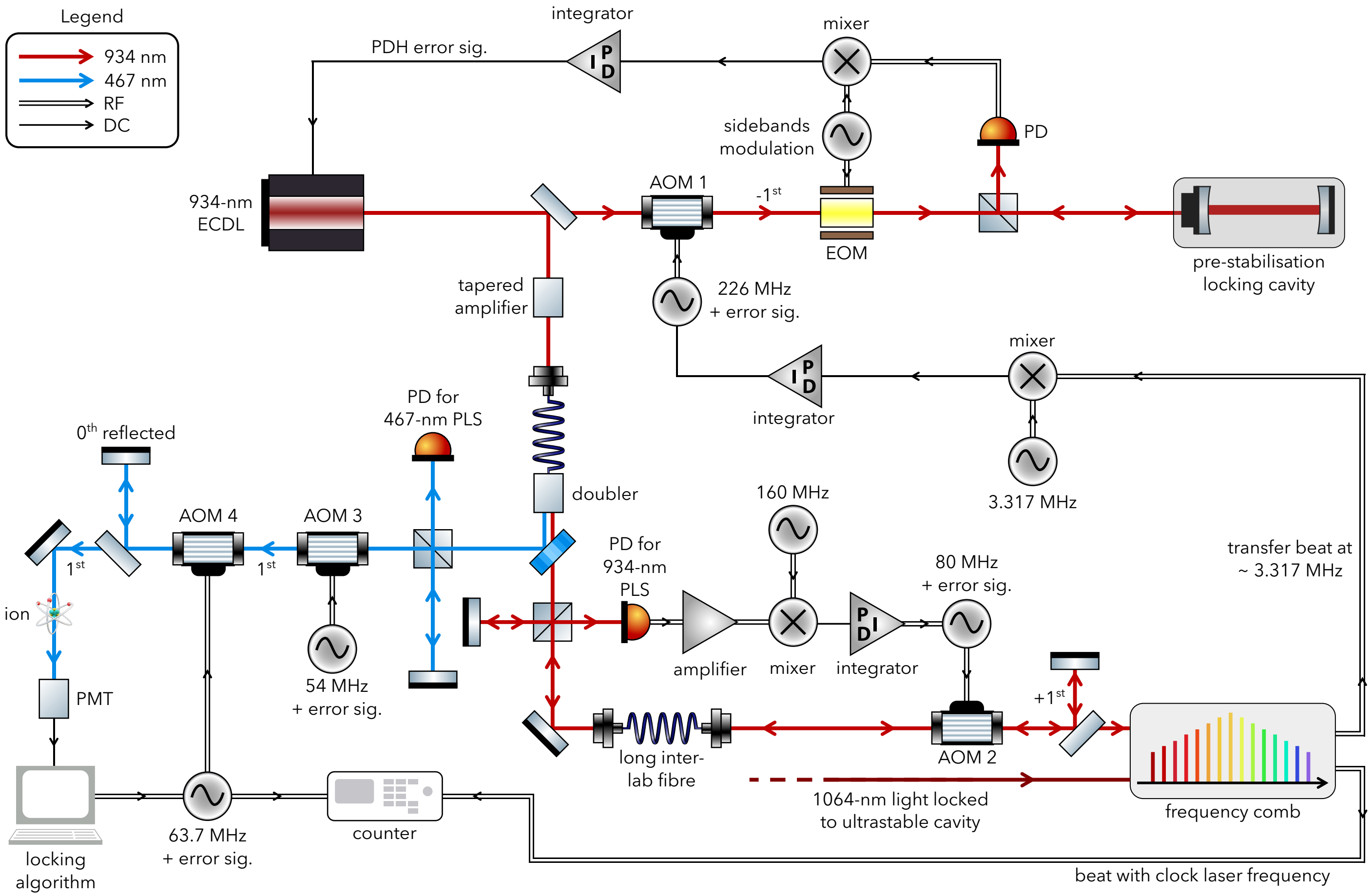

Figure 2.17: Simplified full clock setup for probing the E3 transition and measuring its frequency. The 934-nm light is locked to a local pre-stabilisation cavity via a PDH lock. The frequency-doubled 467-nm light passes first through AOM 3 used to cancel the phase noise on the blue light, and then through AOM 4 used to keep the light locked to the clock transition. The 934-nm light after the doubler is sent to the frequency comb laboratory, in which it passes through AOM 2 used to cancel the 934-nm phase noise accumulated in the inter-lab fibre. Finally, the light reaches the frequency comb, where its frequency is directly measured, and where the stability from an ultrastable 1064-nm laser is transferred to it. An integrator connected to AOM 1 is used to drive the difference between the transfer beat and the reference frequency of 3.317 MHz to zero.

platform. Signals from a 3-axis seismometer placed on the floor near the platform are actively fed forward in order to cancel out vibrations [153]. The stabilised 1064-nm light is then beat with the nearest tooth of the frequency comb, and its stability is transferred to the 934-nm laser via the transfer oscillator scheme [154]. With the same method, the stability of the 1064-nm laser can be transferred to any other light that is measured by the same frequency comb, including the 871-nm clock laser, and also the clock laser used to probe the ^{87}Sr lattice. In practice, as shown in Fig. 2.17, a transfer beat of ~ 3.317 MHz is produced at the frequency between the 1064-nm ultrastable laser and the 934-nm clock light. This transfer beat is mixed with a reference frequency of 3.317 MHz and sent to an integrator which applies a signal to AOM 1 to drive the difference between the two frequencies to zero.

This ultrastable cavity system is ultimately responsible for the achievement of a sub-Hz linewidth of the clock lasers. It is this high level of laser coherence that makes it possible for the E3 transition to be probed with long probe times of over 500 ms. It must be noted that the limit to the clock stability lies in the QPN rather than the Dick effect, which is negligible given the high duty cycle in the E3 transition, which is approximately 90 %. For this reason, the ultrastable local oscillator determines the achievable QPN limit.

2.5.2 Frequency measurement of the 934-nm clock laser

Other than transferring stability to the clock laser, the frequency comb is also used to directly measure the frequency of the clock laser. However, the light that reaches the comb is not the same as the light that probes the ion. For the E3 transition, the frequency of the 934-nm laser is first doubled to 467 nm, and then passes through two AOMs, one for phase noise cancellation in the blue light and one for keeping the frequency locked to the clock transition, which both apply an RF offset. Furthermore, before reaching the frequency comb, the 934-nm light passes through an AOM used for cancelling the phase noise accumulated in the fibre that interconnects the ytterbium ion laboratory and the frequency comb laboratory.

All the frequencies in this chain are logged, and in particular the clock AOM frequency and the beat between the frequency comb and the 934-nm light are measured by a K+K FXE multichannel high-resolution phase and frequency counter, which is referenced to a 10 MHz signal coming from the UTC(NPL) hydrogen maser. It must be noted that in the case of a dual-servo lock, it is not the AOM frequency that is sent to the counter but the extrapolated frequency. To account for this possibility of sending to the counter a frequency that is different from the one driving the clock AOM, the signal that is sent to the counter is generated by a separate direct digital synthesis (DDS) channel.

2.6 Conclusion

This chapter has introduced the experimental apparatus used for operating the $^{171}\mathrm{Yb}^+$ optical clock at NPL. The atomic structure of $^{171}\mathrm{Yb}^+$ was described, and it was shown how all the relevant laser wavelengths are combined and delivered to the ion. The ion trap and vacuum chamber designs were described, together with the method for loading an ion into the trap. The mechanism for laser-cooling the ion was explained, and the different methods for detecting the number of ions in the trap based on their fluorescence were presented. The sequence for probing the clock transition was outlined, and the locking algorithms for keeping the probe light locked to the clock transition were described. Finally, the full optical clock setup was presented, showing how the reference (ion), oscillator (clock laser), and counter (frequency comb) all come together, and the methods for stabilising and measuring the frequency of the probe laser were explained.

A large portion of the experimental apparatus described in this chapter was already in place before the start of my PhD. Since then, I have consistently contributed to the maintenance and optimisation of the various setups. Furthermore, it must be noted that I made a major contribution to the design and assembly of the Beam Combiner setup used for carrying the light from all wavelengths to the ion, as described in section 2.1.2.

While this chapter was more focused on the physical components of the experimental setup and the measurement methods for operating the optical clock, the following chapter will cover the new experimental control system, and how it integrates the various electronic components in the setup. A strong focus will be put on how a new level of experimental automation has been reached, and on the plan towards achieving unattended clock operation.

3 ARTIQ implementation and automation

The ytterbium ion optical clock experiment at NPL was historically run using LabVIEW programs, many of which were cumbersome given the complexity of the experiment and the number of devices that the computer needs to control in a single experimental routine. Over time it became more and more difficult to make changes or improvements to the experiment. Moreover, LabVIEW programs cannot be conventionally version-controlled, making it difficult for the history of their changes to be traceable.

With the emergence of ARTIQ (Advanced Real-Time Infrastructure for Quantum physics), developed partly by ion trappers for quantum information and atomic physics applications, it was chosen for the ytterbium ion experiment to undergo a transition towards this new control system. One of the major advantages of using ARTIQ is the possibility to use Python to program experiments which are then executed with sub-microsecond latency on an FPGA with a timing resolution at the nanosecond level [155]. This also enables the possibility to fully version-control the Python codes that run the experiments and record their version together with the data they generate. Furthermore, ARTIQ brings a new level of scalability and flexibility of the experimental control programs.

Throughout this thesis, several examples of automated experimental routines will be described, and comparisons will be made with how those experiments used to be executed with more manual intervention using the previous control system. The high level of automation gained by using ARTIQ also allows almost every aspect of the optical clock experiment to be run remotely, as very few systems require physical manual intervention.

3.1 ARTIQ hardware setup

The ARTIQ rack used to control the experiment contains a Sinara 1124 Carrier “Kasli” v1.1 board, which is externally clocked by a 100 MHz signal referenced to the H maser generating UTC(NPL). Kasli is the main processor of the system, and contains the FPGA responsible for all ARTIQ operations. Three Sinara 2128 8-channel isolated TTL v1.1 cards are connected to Kasli, providing digital input/outputs (DIO) via front-panel SMA connections. Two Sinara 4412 "Urukul" v1.3 boards each contain 4 DDS channels which are used to provide RF signals at sub-mHz resolution. Finally, a Sinara 5432 DAC "Zotino" v1.3 board is used to output voltages between 0 and ± 10 V.

The outputs of the two 4-channel SRS shutter controllers are provided by the TTL cards, allowing ARTIQ to have full control on the state of each shutter in the Beam Combiner and the cooling, state-preparation and far-detuned beam shutters in the 370-nm setup. Furthermore, the oven controller is toggled by a TTL output, and the PMT signal is measured by a TTL input. The 370-nm, 436-nm and 467-nm AOMs are all driven by the DDS outputs of the Urukul boards, and the cable frequencies that are sent to the K+K counters are also outputted by the Urukuls. The voltages V_{ref} and V_{c} used in the power servo system are outputted by the Zotino board.

Several other peripheral systems are controlled by ARTIQ, such as the homemade shutter drivers that control the shutters in the Wavelength Switcher and the H, U, D shutters, the current controllers for the trap coils, the RF trap drive, and the waveplate rotation mounts in the 370-nm setup. All these require custom-written Python driver wrappers to allow ARTIQ to communicate with these devices. In this way, it is possible to create ARTIQ "experiments" for all the necessary experimental routines required for running the optical clock.

3.2 Automated ion loading

Previously with LabVIEW, the process of loading an ion into the trap used to require a large amount of human intervention. Without the motorised rotation mounts (see section 2.3.1), half-wave plates had to be rotated manually to select the desired 370-nm power splittings between the H, U, D beams for loading. The oven was then fired by a program that set the oven TTL to high for 150 s. This time limit is chosen to avoid the oven getting too hot, in fact, the oven is then left to cool for approximately another 100 s after an unsuccessful loading attempt.

The beam shutters and 370 AOM were all controlled by another program which required the user to manually select their states in real time. Various loading schemes were used that required manual toggling of these states. For example, in order to capture and cool hotter ions, loading was done with the 370 AOM off such that all the power would come from the 0^{th} order far-detuned beam. In order to detect whether an ion was loaded or not, the AOM had to be toggled on every few seconds to check if the level of fluorescence had significantly increased, indicating the presence of one or more ions. If an ion was detected by a rise in fluorescence, it was up to the user to manually terminate the oven-firing program in time to avoid any other ions getting trapped.

In contrast, with a single ARTIQ experiment it is now possible to load a single ion into the trap with the click of a button. The rotation mounts are automatically set at pre-selected wave plate presets for the appropriate power splittings of the three 370-nm beams. The trap RF drive amplitude is automatically decreased to 100 mV to load with a slightly shallower trap. The oven is set to fire for a maximum of 150 s, and every 4 s the 399-nm beam shutter is automatically toggled off for 1 s so that the fluorescence can be recorded. This is done because with the newly-installed high-power 399-nm laser, the 399-nm scatter from the electrodes would produce a high background signal, meaning that if the fluorescence were to increase upon loading an ion, the SNR would be very low.

If an ion is loaded before the end of the 150 s, the fluorescence would be detected to be above a certain set threshold, and the loading routine would terminate. The oven would stop from firing any longer, and the trap drive amplitude would be slowly brought back up to the chosen operational level (typically 130-150 mV). However, if by the end of the 150 s no significant change in the fluorescence level has been detected, the experiment switches to a cooling stage in which the oven is no longer firing and cools down for another 150 s. During this time, the 399-nm beam is turned off and the fluorescence is monitored continuously. If an ion were to appear during this stage, the loading routine would terminate. At the end of the cooling stage, if the fluorescence level has stayed the same, the experiment switches back to the loading stage, and repeats the above process until an ion is loaded.

3.3 Locking algorithm and multi-servo flexibility

With the old LabVIEW system, although the experiment for maintaining a lock to the clock transition was automated, there were many limitations. For example, for a dual-servo locking scheme at two different powers, it was not possible to select different probe durations to achieve optimum π-pulses at both beam powers. Furthermore, because of the complexity of the program design, it would be significantly cumbersome to create any more complex multi-servo locking schemes.

Fig. 3.1 shows a simplified picture of how a dual-servo lock to the clock transition used to be executed in LabVIEW. Once the appropriate best guess of the frequency for the upcoming clock probe was found, the left/right-frequency and high/low-power probes were interleaved as in Fig. 2.15. For both the high- and low-power servos, the same $\pm\delta f$ and probe duration were used. At the end of the servo cycle, the timestamp was recorded, and the extrapolated frequency used throughout that servo cycle was written to a file associated with this timestamp. The new extrapolated frequency was then calculated using Eq. (2.8) and, generated by a DDS, the RF signal was sent to the K+K counters to be measured. Finally, the error signal and cavity drift rate were re-estimated such that the best guess frequency for the next servo cycle could be calculated with Eq. (2.7).

Several improvements to the locking algorithm were made for the ARTIQ version of the experiment, described by the diagram in Fig. 3.2. The timestamp at the beginning of

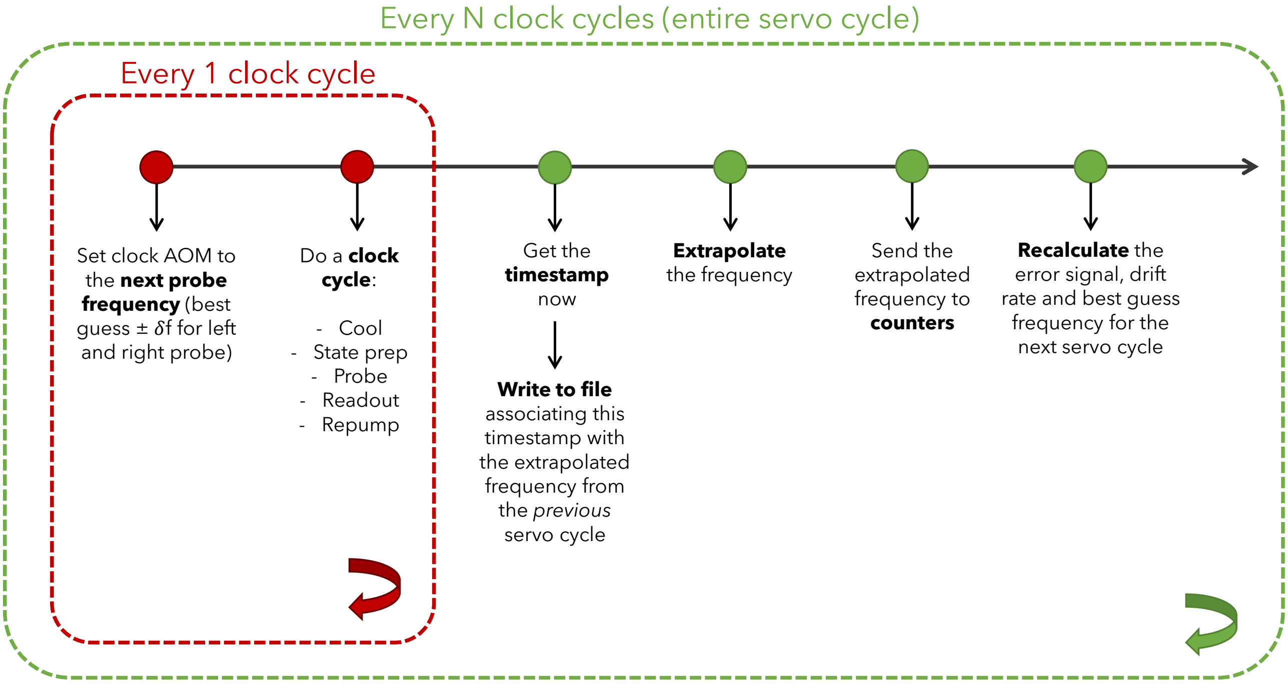

Figure 3.1: LabVIEW dual-servo algorithm.

each clock cycle is recorded and the best guess frequency for the next probe is calculated and recorded in the database (see section 3.4). The clock AOM is set to the next probe frequency f_j, which not only includes the $\pm\delta f$ offset to probe at the FWHM but also an offset that accounts for the cavity drift rate $\delta f/\delta t$, as calculated from the previous servo cycle. This frequency is expressed as:

$$f_j = f_0 + \frac{\delta f}{\delta t}(j+1)\Delta t \, , \tag{3.1}$$

where $0 \leq j \leq N-1$ is the number of the clock cycle within a given servo cycle of N probes, and δt is the average clock cycle duration. After a pair of clock cycles from the high- and low-power servos, the extrapolated frequency is calculated. A new timestamp is recorded, and the extrapolated frequency is written to the database associated to this timestamp. Immediately after that, the extrapolated frequency is sent to the counters to be measured. At the end of the servo cycle, the error signal and cavity drift rate are

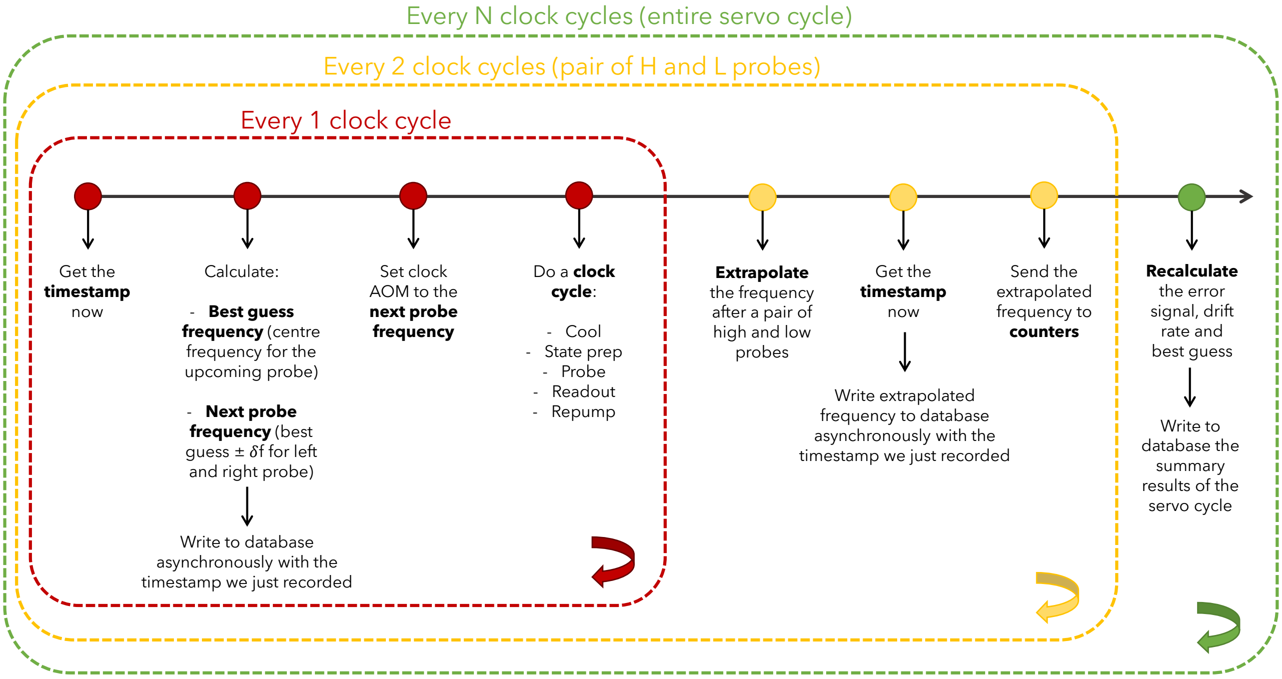

Figure 3.2: ARTIQ dual-servo algorithm.

recalculated and written to the database, and the new best guess frequency is estimated.

By accounting for the drift rate throughout the servo cycle, the effective cavity drift is much smaller, reducing possible frequency offsets in the clock's output. The new servo algorithm also produces extrapolated frequency data at a higher rate. In terms of the dual-servo locking experiment itself, a lot more freedom of parameter choice was available thanks to the relative simplicity to implement this with ARTIQ. Fig. 3.3 shows a small part of the input parameters that can be chosen for a particular dual-servo lock experiment. While previously with LabVIEW the two servos shared all parameters aside from the voltage reference targeting different powers, with ARTIQ it is possible to select their parameters independently, such as clock AOM attenuations, targeted FWHM, and clock probe duration.

Starting frequency of servo 1	63.7 MHz
Total number of probes to interleave	8
Name of servo 1	low_power
Name of servo 2	high_power
Voltage reference of servo 1 (V1)	0.2 V
Voltage reference of servo 2 (V2 > V1)	0.6 V
Power servo voltage offset	1.2 V
Clock AOM attenuation on servo 1	21 dB
Clock AOM attenuation on servo 2	15 dB
FWHM guess for servo 1	1 Hz
FWHM guess for servo 2	1.5 Hz
Probe duration for servo 1	500 ms
Probe duration for servo 2	250 ms
Power ratio (high/low)	3
Guess of AC Stark shift per voltage reference [Hz/V]	8
Device name of clock DDS	dds_467

☐ Due date: Jun 23 2022 00:00:00
Pipeline: main
Priority: 0
☐ Flush
Logging level: INFO
Revision: current

Figure 3.3: Example of an ARTIQ GUI, specifically for the dual-servo lock experiment.

3.4 Monitoring and alerting

All the data recorded through ARTIQ is stored in InfluxDB [156], a time-series database, which is interfaced with a Grafana dashboard [157], allowing the data to be viewed in real time. Aside from the ARTIQ peripherals mentioned in Section 3.1, other devices were integrated with ARTIQ with the purpose of real-time monitoring. With the possibility to set up alerts based on values going over or below a set threshold and send messages to a Microsoft Teams channel, various aspects of the experiment can be closely monitored and a laboratory user can manually recover it from certain failure modes soon after their occurrence. An example of a Grafana dashboard displaying experimental data over a given time interval can be seen in Fig. 3.4.

The most important metrics to monitor in the optical clock experiment are the fluorescence and the clock transition excitation fraction. If the fluorescence drops below a set threshold, an alert is sent out indicating that the ion has gone dark. Most of the time, this is due to either the 370-nm laser unlocking and thus no longer cooling the ion, or the ion having been lost from the trap. In either one of these cases, the user can act upon the alert and either re-lock the cooling laser or reload an ion. Moreover, if the excitation fraction is found to be out of bounds, indicating that the lock to the clock transition has failed, steps can be taken to set it back in lock.

The current, voltage and temperature of the 370-nm and 399-nm lasers are monitored via a connection to the Toptica DLC Pro, such that the historical values can always be recalled whenever the system is shut down or undergoes a sudden or accidental change. Furthermore, the 370-nm cavity transmission is monitored and an alert is sent out whenever it drops below a certain threshold, indicating that the laser has unlocked. The two local clock cavity temperature controllers are also used to monitor the cavity temperatures. The same type of temperature controller was also set up with a thermistor located above the laboratory gantry such that the laboratory temperature can also be monitored in real time. There have been some occasions in which the water cooling of the clock laser boxes was cut off, or the air cooling of the laboratory failed. If any of the three temperatures exceed a specified limit, the user is alerted that there is an issue in the cooling system, such that maintenance can be immediately contacted to fix the problem.

Another useful monitoring system consists of the wavemeter measurement of the wavelength of each laser. An experiment is set up with the Wavelength Switcher to cycle

Figure 3.4: Grafana dashboard displaying data from a dual-servo lock experiment during a chosen time interval, showing ion fluorescence, clock servo frequencies, excitation fractions, high and low frequency jumps for high and low power servos, and laboratory and cavity temperature data.

through all the laser wavelengths at intervals of 100 s, or alternatively single wavelength of interest can be monitored continuously.

3.5 Plan for unattended clock operation

The existing system for monitoring failure modes and sending alerts to laboratory users such that they can be resolved is the first step in the direction of full automation and unattended operation of the optical clock. Ideally, the experiment would be able to automatically recover from failure modes without any human intervention. This section will outline a plan for an ARTIQ "metacontroller" system involving a series of experiments that monitor the status of the clock and upon a particular failure mode automatically take the appropriate steps to fix the issue and bring the clock back to operation.

The idea for the metacontroller algorithm is shown by the flowchart in Fig. 3.5. When the experiment is started, the program would go through all the required routines that need to be launched: these include the lock to the clock transition, fluorescence and jump rate monitors, wavelength monitors, temperature monitors, and cavity transmission monitors. The transfer beat between the clock laser and the ultrastable laser via the frequency comb is also monitored, although we do not have full control of this parameter in the ytterbium ion laboratory due to the involvement of the comb.

After making sure that all the aforementioned experiments are running, the program would check whether any of the monitoring routines have detected a failure mode. If everything is running smoothly, the next step in the algorithm would be to check if the calibration experiments have been triggered by a 12-hour timer, in which case the lock would be stopped, and the calibration experiments would be launched. The algorithm would then restart from the beginning, and if the the lock was stopped, it would be restarted after determining that not all required experiments are running.

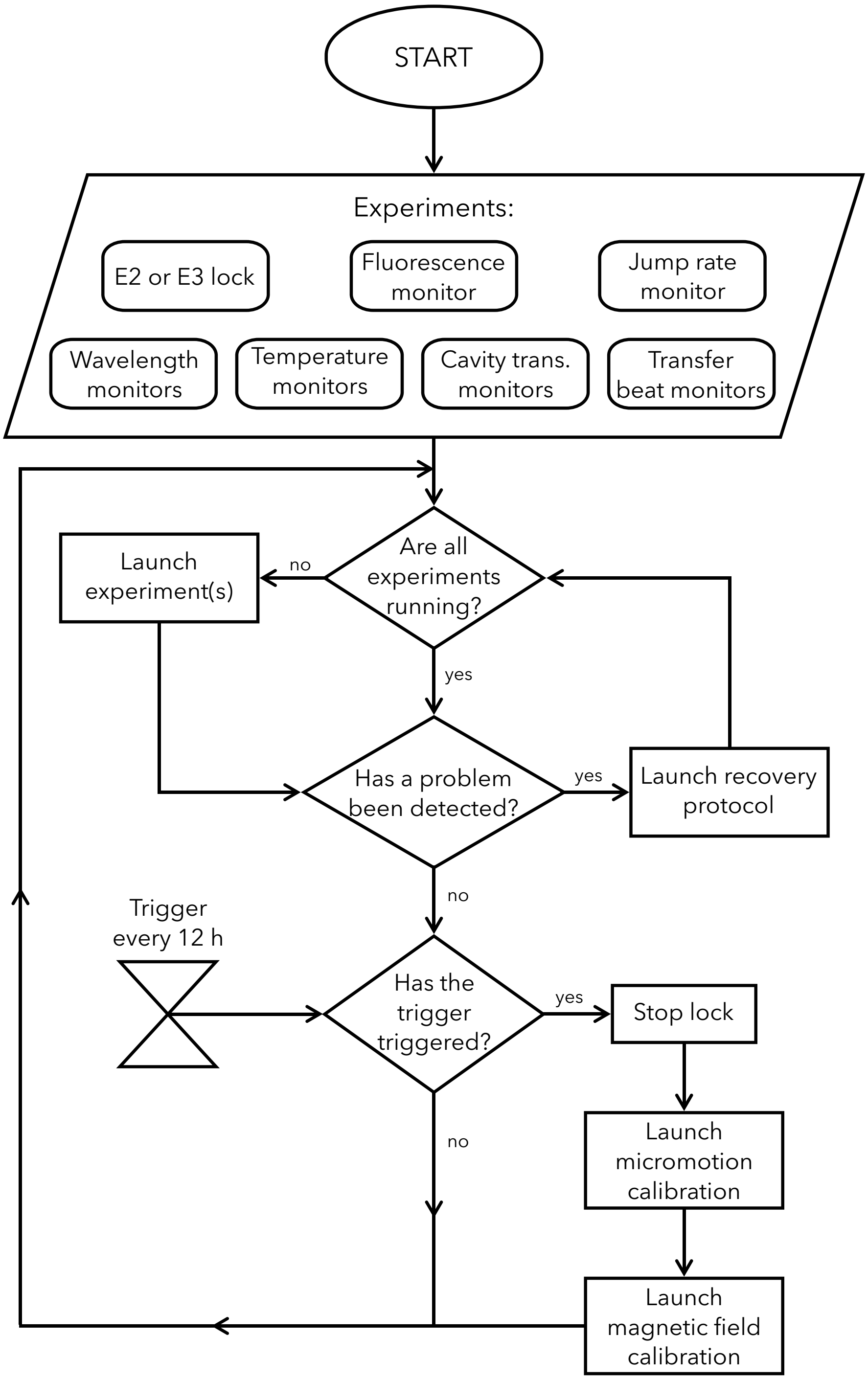

Figure 3.5: Flowchart diagram of the overarching metacontroller algorithm.

If instead a failure mode was detected by one of the monitoring routines, the recovery protocol would be launched. The basic algorithm for this is shown in Fig. 3.6. There are certain aspects of the experiment that cannot be computer-controlled, such as the 871-nm, 934-nm and 935-nm laser locks. If any of their cavity transmission signals are detected to go below a threshold, then the lock would be stopped, and after sending an alert about the specific problem, the program would halt until the laser is manually relocked. The temperature in the laboratory and in the clock-laser cavities could also be detected to go above a certain threshold due to a failure in the laboratory cooling system, which we do not have remote control of. In any other case, the failure mode can be recovered from automatically.

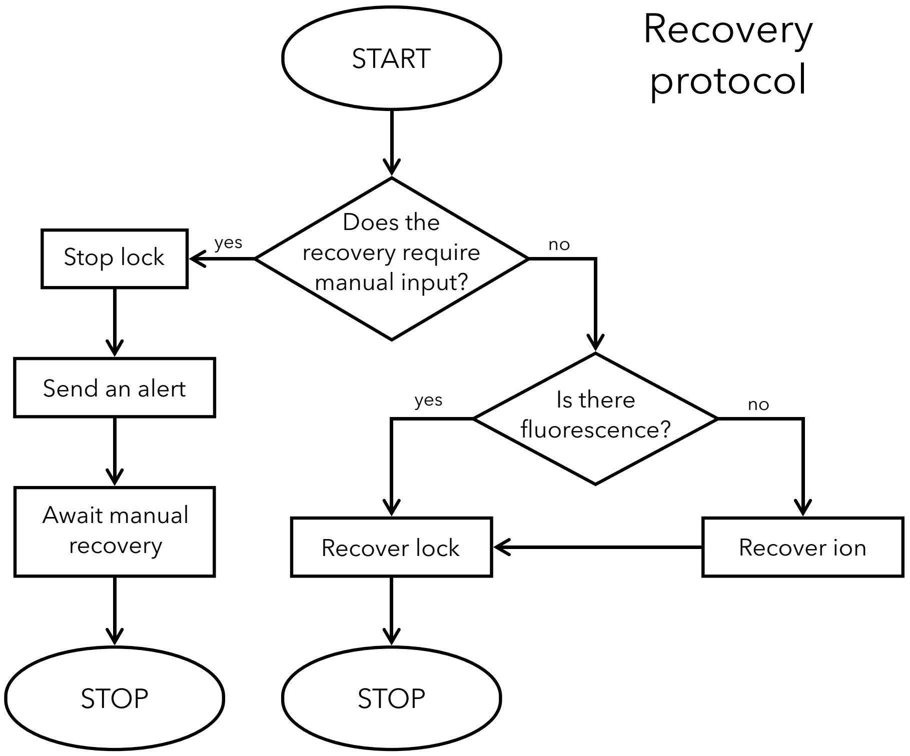

Figure 3.6: Algorithm for the recovery protocol.

3.5.1 Ion recovery

After determining that the problem can be resolved automatically, the program would initially check the level of fluorescence to determine if the ion is dark. In this case, the ion recovery protocol is launched. This is described by the flowchart in Fig. 3.7a. One of the most likely reasons for the ion to have gone dark is because the 370-nm laser has unlocked from the cavity. If this is the case, then the laser can be automatically relocked, and if the fluorescence has returned, then the ion recovery was successful.

However, if the ion is still dark with the cooling laser locked, then any further checks would require the lock to the clock transition to be interrupted. Turning on the 370-nm far-detuned beam is often helpful to recover the ion after a period with insufficient cooling, and also turning on the powerful 399-nm beam would help dissociate a YbH^+ molecule that might have formed. If after ten minutes the fluorescence has still not recovered, then it can be assumed that the ion was lost, and the ion-loading experiment can be launched. In normal conditions, the only reason for the ion loading to be unsuccessful after a reasonable number of attempts would be because the hardware safety limit of ytterbium oven fires has been reached, requiring a manual reset.

One failure mode that is not yet accounted for in the algorithm is the ion getting stuck in either one of the 760-nm $F = 3$ or $F = 4$ states due to the laser wavelengths not being perfectly tuned. However, it is expected that in the near future a new wavelength meter will be installed in the setup which will have a high-enough resolution to enable the two 760-nm lasers to be locked to it.

3.5.2 Lock recovery

The metric to determine whether the clock AOM is locked to the clock transition is the quantum jumps observable in the fluorescence signal. A stable high fluorescence signal with a lack of jumps indicates that the lock is no longer working, as the ion would be

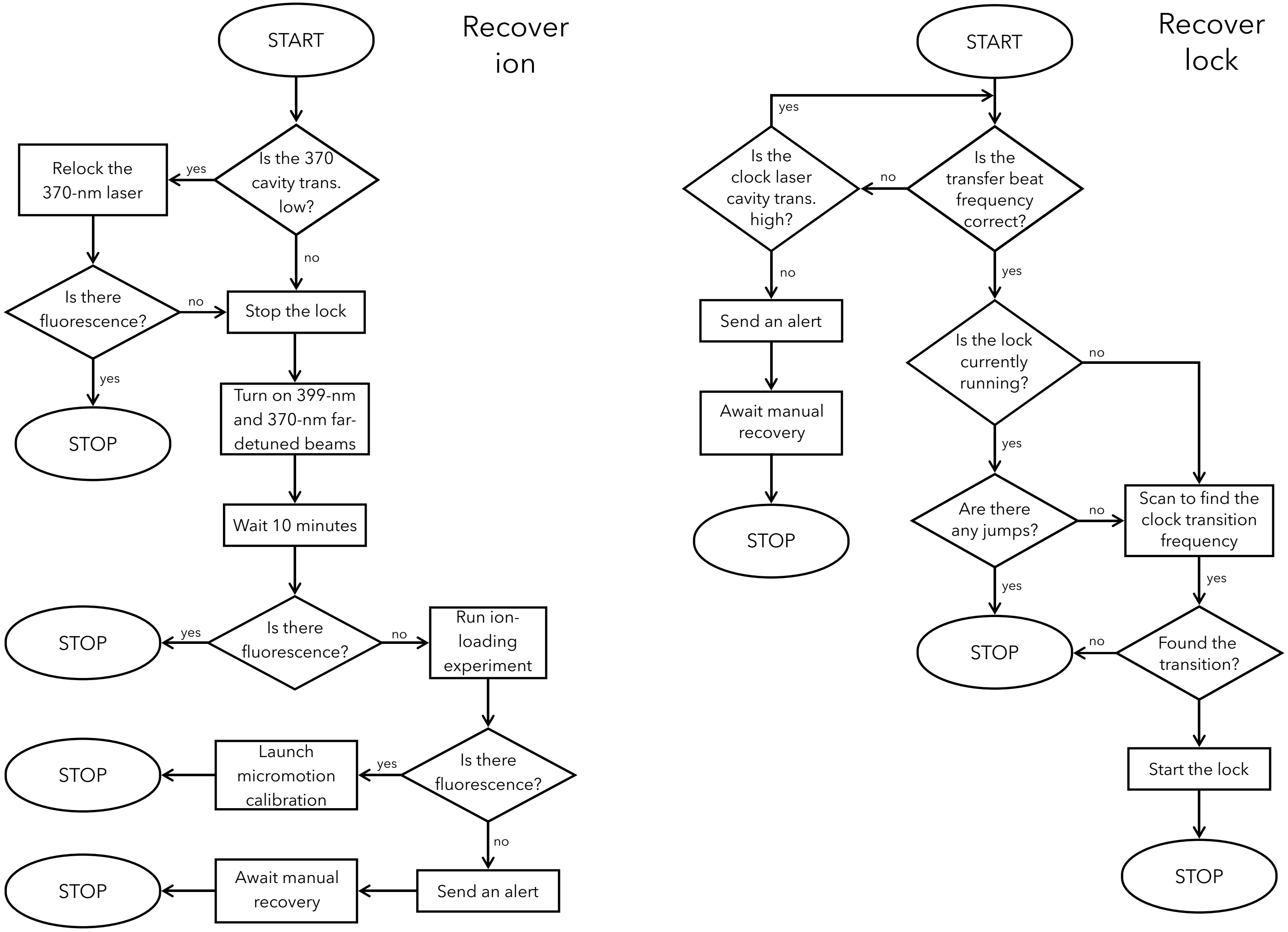

(a) Ion recovery. **(b)** Lock recovery.

Figure 3.7: Algorithms for the automated recovery from most foreseeable failure modes.

stuck in the cooling cycle without getting excited to the clock state. The lock recovery algorithm is displayed in the flowchart in Fig. 3.7b. If the transfer beat frequency between the clock laser and the frequency comb is incorrect, this could be due to the clock laser having unlocked from the local cavity, in which case it would have to be relocked manually. If instead the problem lies in the ultrastable cavity or the frequency comb, which we do not have control of, then the algorithm would keep checking the transfer beat frequency until the problem has been resolved.

Depending on how long it took for the failure mode to be resolved, if the lock was not interrupted, there is a chance that the servo is still close enough to the transition frequency to pull in and go back in lock. If however no jumps are detected, or if the lock had been interrupted, then the next step in the algorithm consists in performing a frequency scan to find the clock transition. If it is found, then the lock can be restarted, and the lock recovery protocol is resolved. If the transition is not detected, it can be assumed that there is another issue that needs resolving, and therefore in the next metacontroller loop the recovery protocol would launch again.

3.6 Conclusion

The implementation of the ARTIQ control system helped in enabling a higher level of automation in the experiment. The flexibility and scalability of ARTIQ code simplified the creation of several new experimental control programs. I had a major role in the implementation of ARTIQ in the experiment, in the programming of several automated routines, in the setup of the automated alerts, and in the general maintenance and debugging of the system. I also made a significant contribution to the design of the algorithms for the automated recovery from failure modes.

While this chapter only covered a few sample routines that were automated and improved, such as loading an ion and locking to the clock transition, throughout the following chapters it will become apparent how many aspects of the experiment have benefited from this new control system. The next chapter will in fact cover how several of the systematic frequency shifts that the ion experiences were measured in an automated manner.

While for the moment many experimental failure modes are monitored, they are not resolved automatically, and instead an alert is sent out for a laboratory user to intervene. This chapter described an initial plan for a “metacontroller” algorithm designed for the experiment to automatically recover from the most common failure modes. Although a few systems in the laboratory are not computer-controlled, and therefore would require manual intervention upon their failure, they are all known to be very robust and are not expected to fail frequently. Once this metacontroller is implemented, the optical clock will in principle be able to run unattended, achieving an unprecedented level of percentage uptime.

4 Systematic frequency shifts

During a measurement of the clock transition frequency, the ion is subject to several systematic effects caused by various factors. First of all, the intensity of the light used to probe the ion induces an AC Stark shift, and the magnetic field set to align the ion's quantisation axis causes a second-order Zeeman shift. Because the ion's environment is at room temperature, it interacts with the environmental BBR. The ion also interacts with the electric fields in the trap used to confine it. Furthermore, the ion is not perfectly stationary, resulting in a shift caused by time dilation. Moreover, the trap is not in a perfect vacuum environment, meaning that some residual gas in the chamber could collide with the ion and shift its transition frequency. Finally, the ion's position in a gravitational field leads to a gravitational redshift.

Accuracy and stability are the two main parameters that describe the performance of an optical clock, and the accuracy can be increased by reducing all the systematic frequency uncertainties by a careful characterisation and calibration of the ion's environment and its interactions with it. For any particular optical clock measurement, which is typically performed as part of a measurement campaign (see Chapter 6), a so-called "uncertainty budget" accompanies the frequency measurement, indicating a value and uncertainty for each systematic shift.

In the past, the analysis of all the systematic shifts from a particular measurement campaign would take several months to complete due to the large amount of manual processing of the data. The programs for calculating the shifts and uncertainties used to be written in a mixture of programming languages and spreadsheets, and many of the results and code versions were not properly traceable. Now, all these analysis programs have been rewritten into Python, and have been designed such that only a few input parameters (such as pointers to raw data and values) are necessary for the whole analysis to be automatically carried out and result in a frequency correction and uncertainty.

Moreover, each systematic shift analysis program is version-controlled, and the version tag accompanies any outputted result, making the generation of any uncertainty budget completely traceable.

While the automation of the analysis of the systematics was done prior to the implementation of the new ARTIQ control system, which meant that the data were no longer stored in text files but in a database, effort was put into making the analysis compatible for both data types. However, it must be noted that ARTIQ has significantly simplified the data analysis process, since any ARTIQ experiment automatically stores in the database all the input parameters that were set.

This chapter will focus on the systematic shifts which have undergone the most progress in terms of the automation of their measurement and of their analysis, and will briefly mention the remaining systematics. Throughout my PhD, having been part of three measurement campaigns, the measurement and analysis techniques for certain systematic shifts kept evolving; in this chapter, they will be described in their most recent form, which led to the uncertainty budget for the 2022 measurement campaign. The results for this campaign are covered in chapter 6.4.

4.1 Micromotion-related shifts

The trapped ion is not perfectly motionless in the trapping potential. Its motion in a trapping potential driven at frequency Ω was already described in section 2.2 by Eq. (2.5). This equation can be rewritten in terms of dimensionless constants a_i and q_i, such that it can be solved to first order as [158]:

$$x_i(t) = [x_{0,i} + x_{1,i}\cos(\omega_i t)][1 + \frac{q_i}{2}\cos(\Omega t + \phi_i)] \,, \tag{4.1}$$

$$\text{with} \quad \omega_i = \frac{\Omega}{2}\sqrt{a_i + \frac{q_i^2}{2}} \,. \tag{4.2}$$

In this equation, $x_{0,i}$ represents the displacement of the ion, induced by stray electric fields, away from the RF node. This displacement leads to excess micromotion. On the other hand, intrinsic micromotion is introduced by $x_{1,i}$ which is the amplitude of the temperature-dependent ion motion at the secular frequencies ω_i in the harmonic trap potential. The motion of the ion in the trap, away from the electric field null, gives rise to two different systematic shifts: the second-order Doppler shift, and the RF Stark shift.

Second-order Doppler shift For an ion confined in the Lamb-Dicke regime, the first-order Doppler broadening is found to be negligible [159], and only the second-order shift is considered. An ion moving at a speed v experiences time dilation which decreases the observed clock frequency. For an ion of mass m and temperature T trapped in an RF potential driven at frequency Ω, the fractional shift is given by:

$$\left\langle \frac{\Delta\nu_{\text{Dop.}}}{\nu} \right\rangle = -\frac{1}{2}\frac{\langle v^2\rangle}{c^2} = -\left(\frac{e}{2mc\Omega}\mathbf{E}_{\text{RF}}\right)^2 - \frac{3k_{\text{B}}T}{mc^2} \,, \tag{4.3}$$

in which the first term arises from motion driven by the residual RF field at the trapping node, $\mathbf{E}_{\text{RF}}$. The second term is the contribution from the thermal kinetic energy of the ion with RF confinement in all three directions.

RF Stark shift The micromotion caused by the electric field $\mathbf{E}$ that the ion experiences in the trap leads to a Stark shift proportional to $\langle \mathbf{E}^2 \rangle$ [160]:

$$\left\langle \frac{\Delta\nu_{\text{RF}}}{\nu} \right\rangle = -\frac{\Delta\alpha}{2h}\langle \mathbf{E}^2\rangle = -\frac{\Delta\alpha}{2h}\left(\frac{\mathbf{E}_{\text{RF}}^2}{2} + \frac{m\Omega^2}{e^2}3k_{\text{B}}T\right) \,, \tag{4.4}$$

where $\Delta\alpha = \alpha_{\text{excited}} - \alpha_{\text{ground}}$ is the differential polarisability of the clock transition. In this equation, the first and second term represent the contributions from the excess and intrinsic micromotion respectively.

4.1.1 Measurement and minimisation of the micromotion

Excess micromotion is detected with the technique of photon correlation, treated in detail in Refs. [7, 158] for the relevant case in which the trapping frequency is comparable to the cooling transition linewidth. In short, the fluorescence modulation caused by excess micromotion is correlated to the RF trap drive phase ϕ. The variation of the photon emission rate S is expressed by:

$$S(t) = S_0 + \Delta S \cos(\Omega t - \phi) \ , \tag{4.5}$$

where S_0 is proportional to the mean fluorescence, $\Delta S/S_0$ represents the normalised modulation amplitude caused by the excess micromotion, and t is the delay between the photon arrival time and the subsequent RF zero crossing.

As described in Ref. [7], for the minimisation of the excess-micromotion amplitude, the voltages of the four DC electrodes shown in Fig. 2.5a from section 2.2 are varied to compensate the residual electric field at the RF node causing the excess micromotion. In order to determine the optimal voltages to minimise the micromotion, a series of voltage configurations are chosen within set bounds, and fluorescence measurements $S(t)$ are taken in each configuration by probing the ion for a specified amount of time (typically 5 to 10 seconds) in each of the H, U, D beams. The targeted mean fluorescence is set to 2000 counts/s for each beam such that S_0 remains consistent. Furthermore, one of the four electrodes, specifically the bottom conical electrode, is fixed at a constant voltage such that the electric potentials arising from the electrode voltages remain approximately constant over time. The magnitude and direction of the resulting electric field gradient will also play an important role in the measurement and minimisation of the electric quadrupole shift (see section 4.3.1).

At the end of the series of micromotion scans, the new optimum electrode voltages are found by minimising the residual mean square error in each of the three orthogonal

370-nm beam directions. This voltage configuration is then sent to the electrodes such that micromotion can be minimum throughout any subsequent clock experiments. The micromotion minimisation routine is typically carried out once a day, since it is observed that the day-to-day changes in the optimum voltages are very small (on average less than 2 % over a 2-week period).

4.1.2 Analysis

After choosing the appropriate voltage configuration that achieves minimum micromotion, the effect of the residual micromotion on the transition frequency must be determined. The measured micromotion signal $\Delta S/S_0$ is proportional to $J_1(\beta)/J_0(\beta)$ for the modulation index $\beta \ll 1$ [158], which is related to $\mathbf{E}_{\mathrm{RF}}$ by:

$$\beta_i = \frac{kQ}{m\Omega^2} E_{\mathrm{RF},i} \ , \tag{4.6}$$

for each near-orthogonal beam direction i, where Q is the charge of the ion and k is the wave vector of the laser. With this information, it is possible to determine $\mathbf{E}_{\mathrm{RF}}$ and hence calculate the average second-order Doppler shift and RF Stark shift throughout the measurement period with Eq. (4.3) and Eq. (4.4) respectively. The uncertainty on the combined shift is typically at the mid 10^{-19} level for the E3 and comes from the propagation of the uncertainties on the measured micromotion in the three directions (corresponding to their standard deviations) with the uncertainty on the ion temperature and on the differential polarisability coefficient.

4.1.3 Automation

In the past, the micromotion-minimisation routine was performed by a LabVIEW program, in which starting electrode voltages and a scan range were set. The scan was performed separately for each of the three H, U, D beams. The half-waveplates in each beam path (see

Fig. 2.8) needed to be manually adjusted to target 2000 counts/s in each individual beam. After the end of a scan with one beam, a prompt would appear requesting the next beam and wait for the user to manually rotate the waveplates and block the appropriate beams for the next series of scans. At the end of the routine, a micromotion model was automatically generated with new optimum voltages, however the threshold for distinguishing positive and negative micromotion needed to be manually set each time according to the fit results. Finally, a new scan was performed at the optimum voltages in each beam, and the outputted micromotion amplitudes were manually recorded. At the end of a clock measurement period, all the recorded amplitudes were averaged for each beam and inserted into an Excel spreadsheet that would calculate the second-order Doppler and RF Stark shifts and their uncertainties.

This process has been greatly simplified with the implementation of ARTIQ, shutters for each of the three 370-nm beams and homemade computer-controlled waveplate rotation mounts. After selecting the starting voltages, scan ranges and three sets of waveplate positions targeting 2000 counts/s in each beam, the minimisation routine runs automatically without requiring any human intervention. For each beam, the waveplates are automatically rotated and the shutter states are automatically set. At the end of the routine, the new optimum voltages are automatically calculated, and this time the phase threshold is included as a fitting parameter. Following the end of this analysis, the routine automatically starts another scan with the new electrode voltages, and stores the resulting micromotion amplitudes in the database. By providing only the micromotion experiment IDs and the value for the ion temperature, a python program can then extract the micromotion amplitudes and trap drive frequency Ω from the database and calculate the two shifts and uncertainties.

4.2 Second-order Zeeman shift

The E2 and E3 clock transitions are both driven between two $m_F = 0$ states, making them insensitive to first-order Zeeman shifts. However, they are still subject to a second-order Zeeman shift that needs to be characterised. With the ion in a static magnetic field $\mathbf{B}$, the clock transition frequency undergoes a second order DC Zeeman shift:

$$\Delta\nu_{\mathrm{DC}} = k_{\mathrm{g}\to\mathrm{e}} B_{\mathrm{DC}}^2 \ , \tag{4.7}$$

where $k_{\mathrm{g}\to\mathrm{e}}$ is a constant coefficient for a given transition. This coefficient was measured for both clock transitions in Ref. [25].

Furthermore, magnetic field noise originating from the AC mains voltage at 50 Hz and other external sources of magnetic field noise can cause a second-order AC Zeeman shift to the transition frequency,

$$\Delta\nu_{\mathrm{AC}} = k_{\mathrm{g}\to\mathrm{e}} \langle B_{\mathrm{AC}}^2 \rangle \ , \tag{4.8}$$

where the time average $\langle B_{\mathrm{AC}}^2 \rangle = B_{\mathrm{AC}}^2/2$ is taken because the measurements are slower than the AC frequency. The total second-order Zeeman shift is therefore given by:

$$\Delta\nu = k_{\mathrm{g}\to\mathrm{e}} \left(B_{\mathrm{DC}}^2 + \frac{B_{\mathrm{AC}}^2}{2} \right) \ . \tag{4.9}$$

4.2.1 Measurement

A series of spectroscopy scans are routinely carried out to probe the Zeeman components of the clock transition, with the purpose of measuring the magnetic field strength arising from the coils and for tuning the background magnetic field. With the current experimental setup, it is not possible to probe the E3 transition with short pulse times for a coarse-resolution scan over the Zeeman components, as that would require a large amount of optical power that is not available. However, the Zeeman components of the E2 can be easily probed, and the shift experienced by the E2 can be converted to the E3 shift by means of the coefficients k_{E2} and k_{E3}. Fig. 4.1 shows a full scan covering the carrier and both pairs of $\Delta m_F = 1$ and $\Delta m_F = 2$ Zeeman components of the E2 in a bias magnetic field targeting 7 µT. Because different magnetic field directions lead to different line strengths for a particular Δm_F, the strongest pair of Zeeman peaks is targeted in a scan. For normal clock operation, the E3 is typically probed in $\mathbf{B}_y$, and in this field direction the strongest components of the E2 are the $\Delta m_F = 1$.

Calibration of background magnetic field It is shown in Fig. 4.2 that magnetic fields in the laboratory drift over time. In order to keep the direction of the desired magnetic field calibrated, the background magnetic field $\mathbf{B}_0$ is re-evaluated daily. This is done by scanning the Zeeman components of six magnetic fields, i.e. three orthogonal magnetic fields $\mathbf{B}_1$, $\mathbf{B}_2$, $\mathbf{B}_3$ and their opposites. A magnetic field $\mathbf{B}$ is related to the background $\mathbf{B}_0$

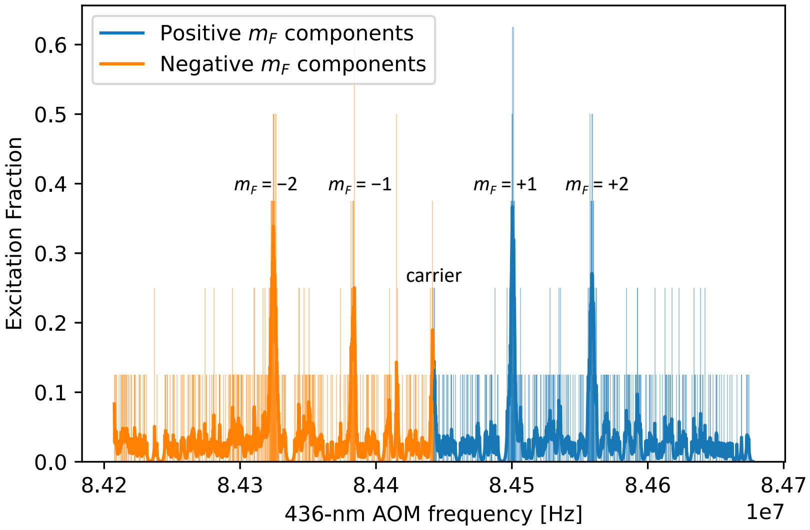

Figure 4.1: Smoothed scan of the $m_F = 0, \pm1, \pm2$ Zeeman components of the $^2\mathrm{D}_{3/2}$ state with a bias magnetic field at 7 µT. The raw data is shown in the background behind the smoothed line.

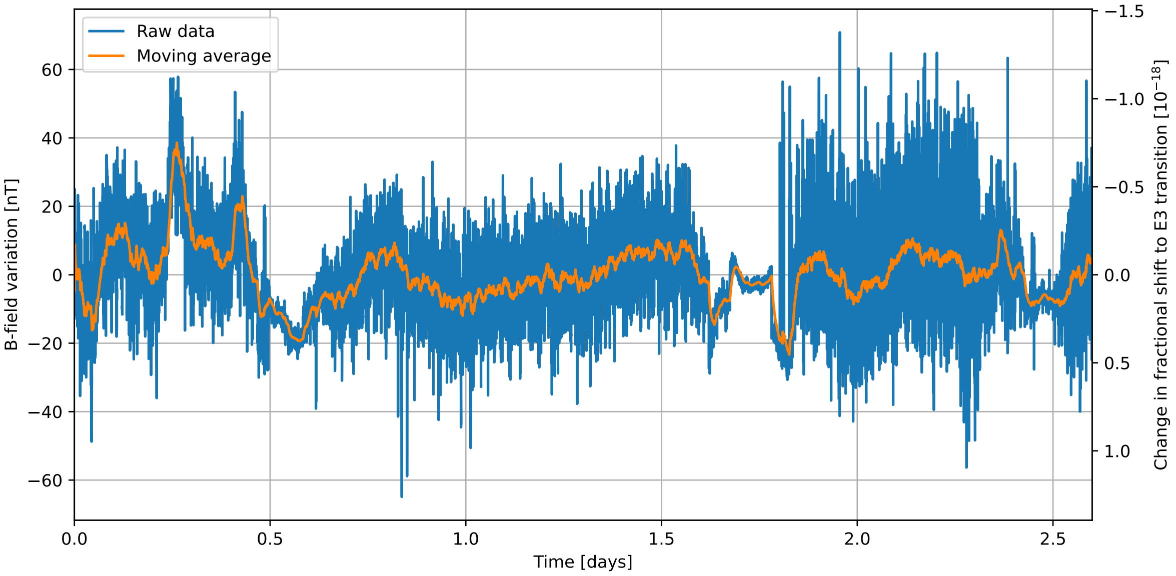

Figure 4.2: Variation of the background magnetic field measured with a Hall sensor. The scale on the right hand side shows the effect of such variations on the E3 transition frequency, assuming a bias field of 3 µT.

by:

$$\mathbf{B} = \mathbf{J}\mathbf{I} + \mathbf{B}_0 \,, \tag{4.10}$$

where $\mathbf{I}$ is the set of coil currents that generates the magnetic field $\mathbf{B}$, and $\mathbf{J}$ is a fixed Jacobian describing the magnetic field response of the coils. The new $\mathbf{B}_0$ is determined by fitting the six resulting magnetic field magnitudes to Eq. (4.10).

4.2.2 Systematic shift analysis

The Zeeman components from scans over the E2 transition in $\mathbf{B}_y$ are fitted with a Rabi profile in order to find their centre frequencies and their widths. The magnitude B_{DC} of the magnetic field is calculated from the frequency separation between the two Zeeman peaks with quantum numbers $m_F = \pm 1$. These quantities are related with the following equation [161]:

$$\nu_{m'_F} - \nu_{m_F} = (m'_F - m_F) B_{\mathrm{DC}} \frac{g_F \mu_{\mathrm{B}}}{h} \,, \tag{4.11}$$

where g_F is the Landé g-factor and μ_B is the Bohr magneton. Moreover, the AC component of the magnetic field is estimated by the average FWHM of the Zeeman components. The final value for the second-order Zeeman shift is calculated as the average result of Eq. (4.9) over all scans of $\mathbf{B}_y$. The uncertainty on the total shift is calculated based on an upper-bound magnetic field uncertainty of 30 nT, gathered from the results shown in Fig. 4.2, corresponding to a fractional frequency uncertainty at the mid 10^{-19} level.

4.2.3 Automation

Prior to the experimental upgrade to ARTIQ, magnetic field scans and calibrations used to be a cumbersome process: coil current values for each magnetic field had to be inputted manually in a LabVIEW program, after being calculated on a spreadsheet from the latest background $\mathbf{B}_0$. After the program completed the scans, the results had to be analysed by a separate MATLAB script that would print out the magnitudes for each field and the values for the new $\mathbf{B}_0$ components. The magnitudes were recorded and kept track of manually throughout a measurement campaign, and the calculation of the Zeeman shift was finally done in a spreadsheet.

With ARTIQ, the process has been hugely simplified by significantly reducing the manual input required to conduct a magnetic field measurement and to analyse the results. The Python program that controls the experiment can access functions from a new analysis program also written in Python. Zeeman component scans are set up by ticking boxes to select which magnetic field directions to scan (e.g. $\mathbf{B}_1$, $\mathbf{B}_2$, $\mathbf{B}_3$, ...) and at what magnitude. The coil currents necessary to produce these magnetic fields are automatically calculated from the latest magnetic field background stored in the database from the previous calibration scan. At the end of the measurement, the program immediately processes the results to determine the new magnetic field background from the fit to Eq. (4.10). All these results are stored in the database, and by simply providing the experiment IDs for the scans of $\mathbf{B}_y$ throughout a clock measurement period, the analysis program automatically extracts the information necessary to calculate the second-order Zeeman shift and uncertainty, which also accounts for the uncertainty in the shift coefficients k_{E2} and k_{E3}.

4.3 Electric quadrupole shift

The electric quadrupole shift is the result of the interaction of the electric quadrupole moment of the ion with an electric field gradient. Whereas the spherically-symmetrical $^2\mathrm{S}_{1/2}\,(F=0)$ ground state does not interact with the electric field gradient, the asymmetrical upper states of both the E2 and E3 transitions are subject to the quadrupole shift. The quadrupole moment is aligned to the ion's quantisation axis, which is parallel to the direction of the magnetic field experienced by the ion. Furthermore, in the centre of the trapping region, an electric field gradient is produced by the voltages in the four DC electrodes; however, its direction cannot be explicitly measured.

Assuming a cylindrically symmetric trap potential, the quadrupole shift has the following form:

$$\Delta\nu = \frac{\Delta\nu_0}{2}\left(3\cos^2\rho - 1\right) , \tag{4.12}$$

where ρ is the angle between the ion's quantisation axis (whose direction is set by the magnetic field $\mathbf{B}$) and the direction of the electric quadrupole field at the ion in the laboratory reference frame denoted by $\hat{\mathbf{n}} = \hat{\mathbf{n}}(x,y,z)$, and $\Delta\nu_0 = |\mathbf{n}|$ is the magnitude of the shift. The shift can therefore also be expressed as:

$$\Delta\nu = \frac{|\mathbf{n}|}{2}\left(3\,\frac{(\mathbf{B}\cdot\hat{\mathbf{n}})^2}{|\mathbf{B}|^2} - 1\right) . \tag{4.13}$$

The magnitude $\Delta\nu_0$ of the quadrupole shift is given by:

$$\Delta\nu_0 = |\nabla\mathbf{E}|\,k(J,I,F,m_F)\,\Theta(L,J) , \tag{4.14}$$

where $\nabla \mathbf{E}$ is the electric field gradient, $\Theta(L, J)$ is the quadrupole moment of the upper state $|L, J\rangle$ of the clock transition, and $k(J, I, F, m_F)$ is a coefficient that includes the Wigner 3-j and 6-j symbols describing the matrix elements of the electric quadrupole operator for the atom [40].

$$k(J, I, F, m_F) = (-1)^{2F+I+J+1-m_F}(2F+1) \begin{pmatrix} F & 2 & F \\ -m_F & 0 & m_F \end{pmatrix} \begin{Bmatrix} J & 2 & J \\ F & I & F \end{Bmatrix} \begin{pmatrix} J & 2 & J \\ -J & 0 & J \end{pmatrix}^{-1} . \tag{4.15}$$

For the E3, $\Theta(F, 7/2) = -0.0297 e a_0^2$ (where e is the elementary charge and a_0 the Bohr radius) [162] and $k = 5/7$, while for the E2, $\Theta(D, 3/2) = 1.95 e a_0^2$ [162] and $k = 1$.

4.3.1 Measurement

The simplest way to deal with the electric quadrupole shift would be to probe the E3 transition in three alternating orthogonal magnetic fields, leading to three different shifts that average out to zero [40]. However, the analysis of optical clock data in which there are frequency shifts at regular intervals due to different magnetic field directions can be quite cumbersome, especially if the clock frequency is to be compared with other optical clocks for frequency ratio measurements. Instead, for simplicity, it is more convenient to probe the E3 in a single magnetic field direction, specifically in $\hat{\mathbf{B}}_y = (0, 1, 0)$. Therefore, the quadrupole shift must be directly evaluated for that particular magnetic field direction such that it can be corrected in post-processing. To determine the quadrupole shift in a specific direction, measurements must be made in many directions to establish the magnitude and direction of the electric field gradient.

The quadrupole shift is approximately 90 times larger for the E2 than for the E3 based on the values of their quadrupole moments $\Theta(L, J)$ and k factors. To exploit the higher sensitivity of the E2 transition, the quadrupole shift is measured by probing the E2 in

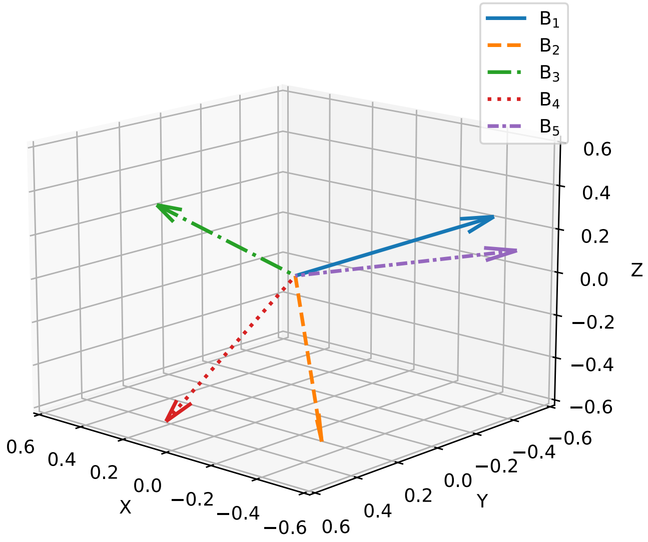

Figure 4.3: Directions of the five magnetic fields used in the quadrupole shift measurement. Note that $\mathbf{B}_1$, $\mathbf{B}_2$, $\mathbf{B}_3$ are orthogonal.

five magnetic field directions (shown in Fig. 4.3) that alternate every 30 minutes. The magnetic fields $\mathbf{B}_1$, $\mathbf{B}_2$, $\mathbf{B}_3$ are chosen to be orthogonal, while the other two fields $\mathbf{B}_4$ and $\mathbf{B}_5$ are at approximately 45° to two of the orthogonal fields. These measurements with the E2 are carried out completely separately from running the clock in the E3.

Because any lock to a clock transition is affected by the drift of the ultrastable cavity to which the clock laser is locked, this measurement is interleaved with a second *reference* servo probing the E2 in a single magnetic field, $\mathbf{B}_1$, providing a stable reference for the first *spinning* servo and allowing the effect of the cavity drift to cancel out by subtracting the frequencies of the two servos. The two servos (see Fig. 4.4) are interleaved in the same way as an E3 dual servo lock, as shown in Fig. 2.15. Two sets of current supplies are used to generate the magnetic fields for the *reference* and *spinning* servos, and a relay controlled by a TTL is used to switch between the two.

While the effect of stray electric fields in the trap cannot be controlled, the DC quadrupole potential contributing to $\nabla\mathbf{E}$ is set by the voltages of the four DC electrodes,

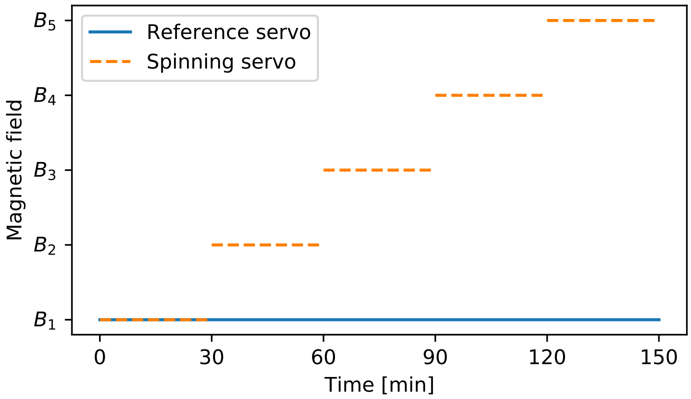

Figure 4.4: Time series of the interleaved spinning and reference servos.

and thus it is possible to minimise it. This can be done by a careful choice of voltage configurations, targeting the minimisation of the resulting quadrupole shift magnitude and of the y-component of the electric field gradient. As the E3 transition is probed in $\mathbf{B}_y$, the ion would be least sensitive to wobbles and drifts in the magnetic field if the electric field gradient were in the x or z direction. A series of measurements were performed at different voltages of the bottom conical electrode (ECB), which as mentioned in section 4.1 is the only electrode whose voltage is fixed. Figs. 4.5a and 4.5b show the resulting electric field gradient vectors and quadrupole shifts and uncertainties. The configuration with the ECB at 0 V was chosen for operation, as it resulted in the best balance between a small component in the y-direction and a small resulting quadrupole shift and uncertainty.

The quadrupole shift measurement is typically performed twice, once before and once after a long-term measurement of the E3. Given that the electric field gradient is determined by the voltages in the four DC electrodes, and these are varied only minimally during micromotion calibrations, it is expected that its change would be negligible between the start and the end of a few-week-long measurement. This is indeed verified experimentally by the two “before and after” quadrupole shift results agreeing within their uncertainty in normal conditions.

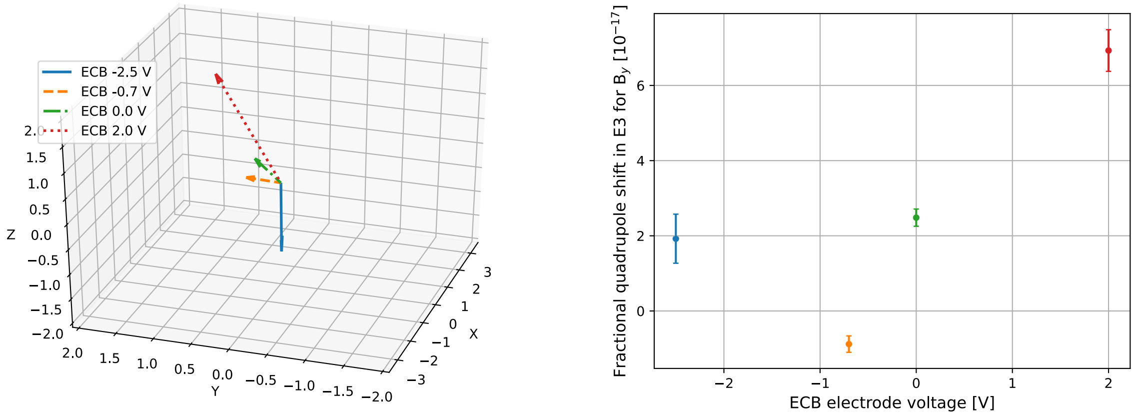

(a) Electric field gradient vectors. **(b)** Fractional quadrupole shifts and uncertainties.

Figure 4.5: Resulting electric field gradient vectors and quadrupole shifts and uncertainties for different values of the ECB electrode voltage.

4.3.2 Systematic shift analysis

The dual-servo quadrupole shift experiment described above results in five different sets of frequency data (one for each magnetic field), to which the stable frequency reference in $\mathbf{B}_1$ is subtracted (see Fig. 4.6). The data from the first 5 minutes of each 30-minute section are removed such that the effect of the servo pulling into the new frequency level can be ignored. Because the quadrupole shift is expected to average out to zero for the three orthogonal fields $\mathbf{B}_1$, $\mathbf{B}_2$, $\mathbf{B}_3$, the average frequency between those three datasets is subtracted from the average $\Delta\nu'_i$ of each of the five datasets, leading to a quadrupole shift $\Delta\nu_i$ for each magnetic field $\mathbf{B}_i$:

$$\Delta\nu_i = \Delta\nu'_i - \frac{\Delta\nu'_1 + \Delta\nu'_2 + \Delta\nu'_3}{3} \, . \tag{4.16}$$

The uncertainty on each of the five shifts $\Delta\nu'_i$ is calculated using the QPN formula defined in Eq. (1.3) for an averaging time of $\tau/3$, where τ is the total measurement time. The reason why τ is divided by 3 is because the overlapping Allan deviation of the frequency data can only be verified experimentally up to a third of the total measurement

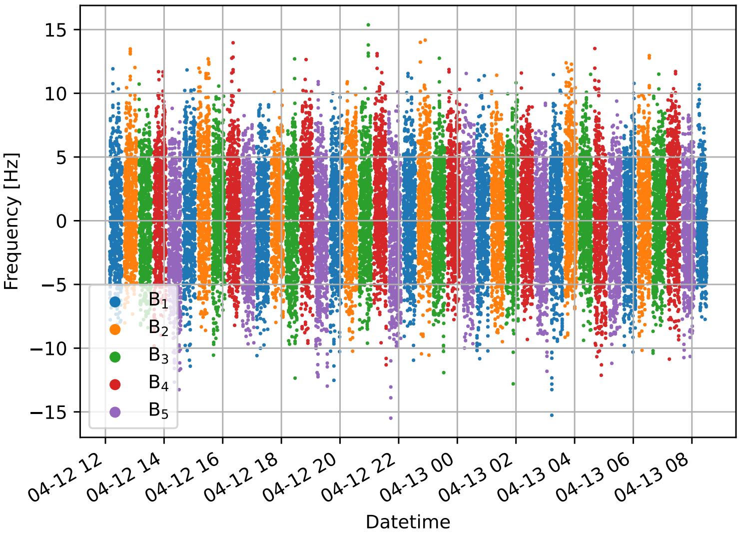

Figure 4.6: Frequency shift of the E2 transition measured in five magnetic fields with respect to a stable reference in $\mathbf{B}_1$. The magnetic fields were alternated at 30-minute intervals.

duration. Since each shift $\Delta\nu_i'$ is calculated as a difference between the *spinning* and the *reference* servo frequencies, the uncertainty is calculated as the QPN of each servo combined in quadrature.

Because the E3 is probed in $\mathbf{B}_y$, the quadrupole shift needs to be extrapolated for this magnetic field direction. The reason why $\mathbf{B}_y$ is never chosen as one of the magnetic fields to probe the E2 for the quadrupole shift measurement is because its line strength in that field is particularly poor given its vertical polarisation, which is a fixed parameter. In order to extrapolate what the quadrupole shift of the E2 would be in $\mathbf{B}_y$, the electric field gradient direction $\hat{\mathbf{n}}(x, y, z)$ and its magnitude need to be determined. This is done by performing a global fit to determine the parameters $\{x, y, z\}$ that minimise the following equation for the sum of residuals scaled by the shift uncertainties:

$$f_{\text{fit}} = \sum_{i=1}^{5} \left[\frac{|\mathbf{n}|}{2} \left(\frac{3(\mathbf{n} \cdot \mathbf{B}_i)^2}{|\mathbf{n}|^2 |\mathbf{B}_i|^2} - 1 \right) - \Delta\nu_i \right]^2 \frac{1}{\sigma_i^2} \,. \tag{4.17}$$

To aid the fitting procedure to propagate errors correctly, the Jacobian of the model function is calculated with respect to its fitting parameters $\{x, y, z\}$ and is used in the weighting of the fit.

$$\mathbf{J^T}(x,y,z) = \begin{pmatrix} \frac{\partial \Delta\nu}{\partial x} \\ \frac{\partial \Delta\nu}{\partial y} \\ \frac{\partial \Delta\nu}{\partial z} \end{pmatrix} = \frac{3(\mathbf{B}\cdot\mathbf{n})}{|\mathbf{B}|^2|\mathbf{n}|} \begin{pmatrix} B_x - \frac{x(\mathbf{B}\cdot\mathbf{n})}{|\mathbf{n}|^2} \\ B_y - \frac{y(\mathbf{B}\cdot\mathbf{n})}{|\mathbf{n}|^2} \\ B_z - \frac{z(\mathbf{B}\cdot\mathbf{n})}{|\mathbf{n}|^2} \end{pmatrix} + \frac{1}{2|\mathbf{n}|}\left(\frac{3(\mathbf{B}\cdot\mathbf{n})^2}{|\mathbf{B}|^2|\mathbf{n}|^2} - 1\right) \begin{pmatrix} x \\ y \\ z \end{pmatrix} . \tag{4.18}$$

Although the conventional fitting algorithms for bounded problems are relatively robust, these are designed to converge to a local minimum of the fit function. It was found that this particular problem has several local minima which the fit could converge to depending on different guesses of initial fit parameters. For this reason, the *differential evolution* algorithm [163] was used and tuned to maximise the probability to converge to a global minimum, determined through simulation to be 99 %. This method is also advantageous as it does not require initial guess parameters; the search is performed within a bounded grid.

After the fit has converged to a vector $\mathbf{n}(x, y, z)$, the electric field gradient direction and the quadrupole shift magnitude can be extrapolated. Based on Eq. (4.14), a scale factor is used to convert the quadrupole shift magnitude from E2 to E3:

$$\Delta\nu_{0,\mathrm{E3}} = \frac{\Theta(F, 7/2)}{\Theta(D, 3/2)} \frac{k_{E3}}{k_{E2}} \Delta\nu_{0,\mathrm{E2}} \, . \tag{4.19}$$

Finally, the angle ρ between the electric field gradient $\hat{\mathbf{n}}$ and the magnetic field $\mathbf{B}_y$ can be calculated. The uncertainty σ_f on the quadrupole shift of the E3 is calculated with the following equation [164]:

$$\sigma_f^2 = \mathbf{J}\boldsymbol{\Sigma}^x\mathbf{J^T} \, , \tag{4.20}$$

where $\mathbf{J} = \mathbf{J}(x, y, z)$ is the Jacobian from Eq. (4.18) and $\boldsymbol{\Sigma}^x$ is the covariance matrix outputted from the fit scaled down for the E3. This is then propagated with the uncertainty on the scale factor from Eq. (4.19), calculated from the errors on the quadrupole moments of the E2 and the E3.

The quadrupole shift is currently the leading source of uncertainty for both the E2 and E3 transitions. For a given electric field gradient configuration, the most significant uncertainty contribution comes from the statistical noise of the measurement, as the QPN for each magnetic field dataset was used by the fitting algorithm to determine the uncertainty on the electric field gradient. For this reason, using this measurement technique, the uncertainty can be reduced by running the quadrupole shift experiment for a longer duration. For instance, with a measurement duration of approximately 60 hours, the fractional uncertainty on the quadrupole shift on the E3 was determined to be 2.8×10^{-18}.

4.3.3 Considerations of magnetic field effects

The analysis that was just described assumed that all of the magnetic fields experienced by the ion during the quadrupole shift measurement or the E3 measurements correspond to the nominal pre-determined vectors $\mathbf{B}_i$, with constant magnitudes and directions. However, it was shown in section 4.2 that background magnetic fields can drift by up to 30 nT in a day. An imperfect cancellation of the background magnetic field would also result in slightly different magnetic field direction from the nominal $\mathbf{B}_y$. For the same reason, the E2 frequency might experience slightly different second-order DC Zeeman shifts in the five magnetic fields. All these effects are accounted for to ensure that the quadrupole shift is calculated correctly and its uncertainty is not being underestimated.

Uncertainty on $\mathbf{B}_y$ During an E3 measurement, $\mathbf{B}_y$ is typically set with a magnitude of 3 µT. Assuming that the components of $\mathbf{B}_y$ have an uncertainty of 30 nT, these uncertainties are propagated together with the parameters $\{x, y, z\}$. A Jacobian is defined with respect to the magnetic field components of $\mathbf{B}_y$:

$$\mathbf{J}^{\mathbf{T}}(B_x, B_y, B_z) = \begin{pmatrix} \frac{\partial \Delta\nu}{\partial B_x} \\ \frac{\partial \Delta\nu}{\partial B_y} \\ \frac{\partial \Delta\nu}{\partial B_z} \end{pmatrix} = \frac{3(\mathbf{B} \cdot \mathbf{n})}{|\mathbf{B}|^2 |\mathbf{n}|} \begin{pmatrix} x - \frac{B_x(\mathbf{B}\cdot\mathbf{n})}{|\mathbf{B}|^2} \\ y - \frac{B_y(\mathbf{B}\cdot\mathbf{n})}{|\mathbf{B}|^2} \\ z - \frac{B_z(\mathbf{B}\cdot\mathbf{n})}{|\mathbf{B}|^2} \end{pmatrix} . \tag{4.21}$$

A covariance matrix $\boldsymbol{\Sigma}_B$ for the magnetic field components is defined as:

$$\boldsymbol{\Sigma}_B = \begin{pmatrix} (0.03/3)^2 & 0 & 0 \\ 0 & (0.03/3)^2 & 0 \\ 0 & 0 & (0.03/3)^2 \end{pmatrix} , \tag{4.22}$$

where 0.03 is the uncertainty on each field component and 3 is the normalisation factor by which also $\mathbf{B}_y$ is normalised in the analysis. The two Jacobians $\mathbf{J}(x, y, z)$ and $\mathbf{J}(B_x, B_y, B_z)$ are then combined to form:

$$\mathbf{J}_{\text{c}} = \begin{pmatrix} \frac{\partial \Delta\nu}{\partial x} & \frac{\partial \Delta\nu}{\partial y} & \frac{\partial \Delta\nu}{\partial z} & \frac{\partial \Delta\nu}{\partial B_x} & \frac{\partial \Delta\nu}{\partial B_y} & \frac{\partial \Delta\nu}{\partial B_z} \end{pmatrix} , \tag{4.23}$$

and the two respective 3 × 3 covariance matrices are also combined diagonally into a 6 × 6 covariance matrix $\boldsymbol{\Sigma}_{\text{c}}$. The total uncertainty on the shift is finally calculated as:

$$\sigma_{\text{tot}}^2 = \mathbf{J}_{\text{c}} \boldsymbol{\Sigma}_{\text{c}} \mathbf{J}^{\mathbf{T}}{}_{\text{c}} \, . \tag{4.24}$$

Results show that the difference in the inclusion of this additional background magnetic field uncertainty is negligible.

Drifting magnetic fields To account for the possibility of drifting magnetic fields during a long-term measurement, all the magnetic field calibration scans throughout that measurement campaign are investigated. This is done for both the quadrupole shift measurement and the E3 campaign measurement. As explained in section 4.2, magnetic field calibration scans are carried out over the Zeeman components of the E2 for a range of magnetic field orientations. The measured field $\mathbf{B}$, together with the coil currents $\mathbf{I}$ used to produce each field, are fitted in order to calculate the background magnetic field $\mathbf{B}_0$ with Eq. (4.10). Since the magnetic fields are expected to drift over time, $\mathbf{B}_0$ must be re-evaluated approximately once a day in between E3 locks in order to update the currents necessary to produce the correct bias magnetic field for the next lock. The effect of this drift on the quadrupole shift is quantified in the following way. For two calibration sets k and $k+1$ taken before and after a lock, the initial magnetic field vector is calculated as:

$$\mathbf{B}_k = \mathbf{J}\mathbf{I}_k + \mathbf{B}_{0,k} \ , \tag{4.25}$$

while the final magnetic field vector is calculated as:

$$\mathbf{B}_{k+1} = \mathbf{J}\mathbf{I}_k + \mathbf{B}_{0,k+1} \ , \tag{4.26}$$

where we use the new background field $\mathbf{B}_{0,k+1}$ from the calibration set $k+1$, but the same set of currents $\mathbf{I}_k$ that was used throughout the whole lock. The quadrupole shift is then calculated for the sets of fields $\mathbf{B}_k$ and $\mathbf{B}_{k+1}$, and the difference between them is considered as the uncertainty originating from the drift. The average differences between all the E2 datasets and between all the E3 datasets are added in quadrature to the uncertainty on the quadrupole shift from Eq. (4.24).

DC Zeeman shifts in the five magnetic fields Based on the currents $\mathbf{I}_k$ and background fields $\mathbf{B}_{0,k}$ used throughout E2 locks for the quadrupole shift measurement, the second order DC Zeeman shift is calculated on the frequency measured during each of the five magnetic field datasets and is corrected for.

4.3.4 Automation

The automated experimental measurement is in the same format as a dual-servo lock, with the added complexity of switching coil current supplies between each *spinning* and *reference* servo probe and alternating magnetic field direction every 30 minutes. Thanks to the flexibility brought by ARTIQ, a large portion of core code can be shared by any type of single- or multi-servo lock experiment, making it more simple and straightforward to create new experiments of this type.

For the automation of the analysis of the quadrupole shift, several pieces of information need to be passed to the program. First of all, the key data resulting from the experiment consists of two sets of 436-nm AOM frequencies, one for the *spinning* servo and one for the *reference* servo, and two sets of excitation fractions. Integers from 1 to 5 are associated to each timestamp to indicate in which magnetic field the data was taken for the *spinning* servo. This allows the program to easily distinguish the frequency shifts for each magnetic field. The program extracts all this information from the provided experiment ID, which is unique to each lock.

For the program to analyse the effects of drifting magnetic fields on the quadrupole shift, it is also necessary to provide it with the information about all the magnetic field calibration scans performed during the quadrupole shift measurements and during the E3 campaign measurement. The experiment IDs of the relevant Zeeman component scans are passed to the program, which can then extract the information about magnetic field magnitudes throughout the measurements.

4.4 AC Stark shifts

The clock transitions experience an AC Stark shift proportional to the laser intensity $\langle \mathbf{E}^2 \rangle$ and the differential polarisability $\Delta\alpha$ [40]. For the E2 this shift is negligible, as the probe light power is < 1 nW. However, for the E3 which is probed with hundreds of microwatts of 467-nm light, the shift is so large (of the order of Hz) that it must be cancelled out in real time. This is why the E3 is probed in a dual-servo configuration at two different power levels, as already explained in section 2.4.4, such that the unperturbed frequency can be extrapolated.

The real-time frequency extrapolation assumes an exact power ratio between the two servos, as set by the user in the input parameters. However, the electronics controlling the power level are not perfect so the power can slightly drift. Moreover, the power level might not exactly correspond to what was requested, and therefore there is still a residual probe-induced AC Stark shift that must be accounted for. Furthermore, there is the possibility that some light from the other beams coupled to the PCF might leak through the closed shutters during the clock-probe stage, which would lead to a small additional AC Stark shift.

Another effect that needs to be accounted for is the overshoot in power that occurs when the clock AOM turns on at the beginning of the pulse. Due to the limited bandwidth of the integrator, there is a short period of time (tens to hundreds of microseconds) between the AOM switch-on and the moment the beam power is brought down to its requested power level. This power overshoot causes the clock transition frequency to shift temporarily. This shift is only relevant for the E3 since there is no power-servo setup for probing the E2.

The AC Stark shifts from leakage light and from the power overshoot are treated already in Ref. [7], and while their current measurement method has remained the same, both analysis programs have been rewritten in Python such that they can be run automatically. This section will focus more on the residual probe-induced AC Stark shift and its uncertainty, since there have been more significant changes in terms of the analysis and its automation.

4.4.1 Residual probe-induced AC Stark shift

As shown in Fig. 2.16, an OOL photodiode is used to measure the optical power of the 467-nm beam just after passing through the vacuum chamber windows and the beam splitter. The power data is recorded by a LabVIEW program which writes the results to a text file. The high-power and low-power probe levels are distinguished based on the expected pulse pattern. For each reported extrapolated frequency, the average measured high-power and low-power levels are used to calculate the true power ratio, leading to the true extrapolated frequency. It is therefore possible to apply a correction to the reported extrapolated frequency in post-processing.

To minimise the necessary post-correction to the extrapolated frequency, and therefore producing a more accurate frequency in real time, a short (∼ 5 minutes) dual-servo experiment was run prior to each E3 lock in order to determine a more accurate value of the power ratio to be used in the frequency extrapolation calculation. Fig. 4.7 shows that the flicker floor is reached on the order of 10^2 s, suggesting that a measurement of the

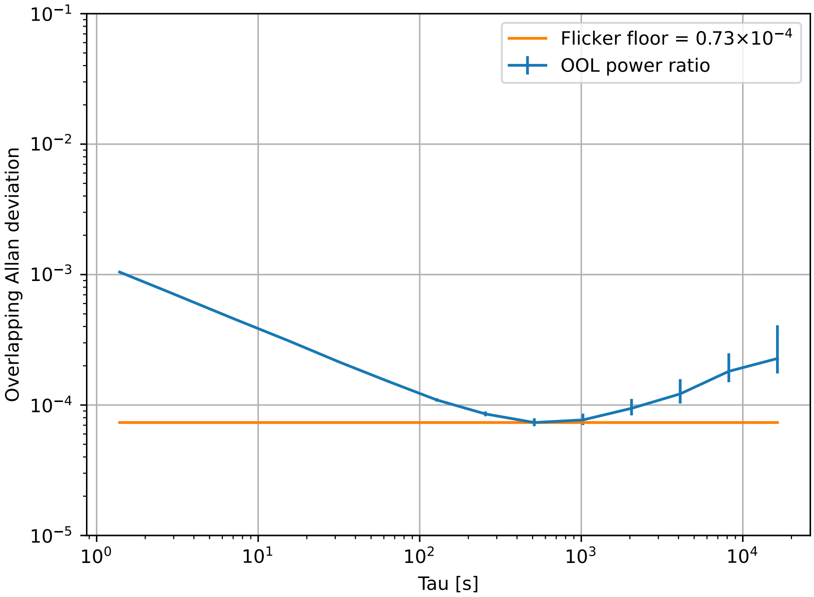

Figure 4.7: Overlapping Allan deviation of the power ratio measured by the OOL photodiode.

order of minutes should give an accurate enough estimate of the power ratio.

The flicker floor of the overlapping Allan deviation of the power ratio R_{OOL} measured by the OOL photodiode (shown in Fig. 4.7 for a sample dual-servo lock dataset) is considered as the uncertainty δR_{OOL} on the power ratio. The uncertainty on the residual AC Stark shift correction is then given by:

$$\delta\nu = \frac{\delta f}{(R_{\mathrm{OOL}} - 1)^2}\,\delta R_{\mathrm{OOL}}\ , \tag{4.27}$$

where δf is the average frequency difference between the high-power and low-power pulses.

4.4.2 Automation

Previously, the analysis of the uncertainty on the residual probe-induced AC Stark shift used to be performed on a single sample dual-servo lock dataset, in which the entirety of the OOL power ratio data was considered, regardless of the uptime of the clock during that period, and an approximate flicker floor value was visually extracted from the Allan deviation plot. This analysis has now been updated to consider all dual-servo lock datasets, and to automatically extract the high-low servo frequency difference from the database and the flicker floor from the OOL power ratio data. Furthermore, the frequency and power data are filtered by the clock uptime, which is automatically determined by ion fluorescence levels and excitation fraction. The only input parameters required for this analysis are the dual-servo lock experiment IDs and the corresponding OOL file IDs.

4.5 BBR Stark shift

The BBR Stark shift arises from the interaction of the ion with an oscillating electric field originating from the room-temperature environmental radiation. The shift depends on the temperature of the ion's environment during a clock measurement and on the differential polarisability $\Delta\alpha$ of the clock transition. The E3 has a particularly small differential polarisability [19], leading to a BBR shift with an uncertainty at the 1×10^{-18} level. On the other hand, for the E2 the BBR shift has one of the leading uncertainties in the systematic budget ($\sim 1 \times 10^{-16}$) due to the high uncertainty on $\Delta\alpha_{\mathrm{E2}}$ [23].

During a clock measurement, the temperature of the ion's environment is measured at 30-s intervals by four PT100 sensors positioned around the vacuum chamber. Fig. 4.8 shows approximately five days of temperature measurements during an E3 clock measurement period. The temperature spikes are an indication of the heat dissipated by the coils generating the large magnetic field required for cooling the ion. During a lock, the clock pulse makes up the majority of the probe sequence, thus because the coils are only on for a relatively short duration, their heat contribution is lower than when the clock is out of lock and the ion is being continuously cooled.

Previously, the analysis of the BBR shift was performed in an Excel spreadsheet, where the temperature data was manually filtered based on the start and stop times of each lock to the clock transition during a given measurement, and an average temperature was used

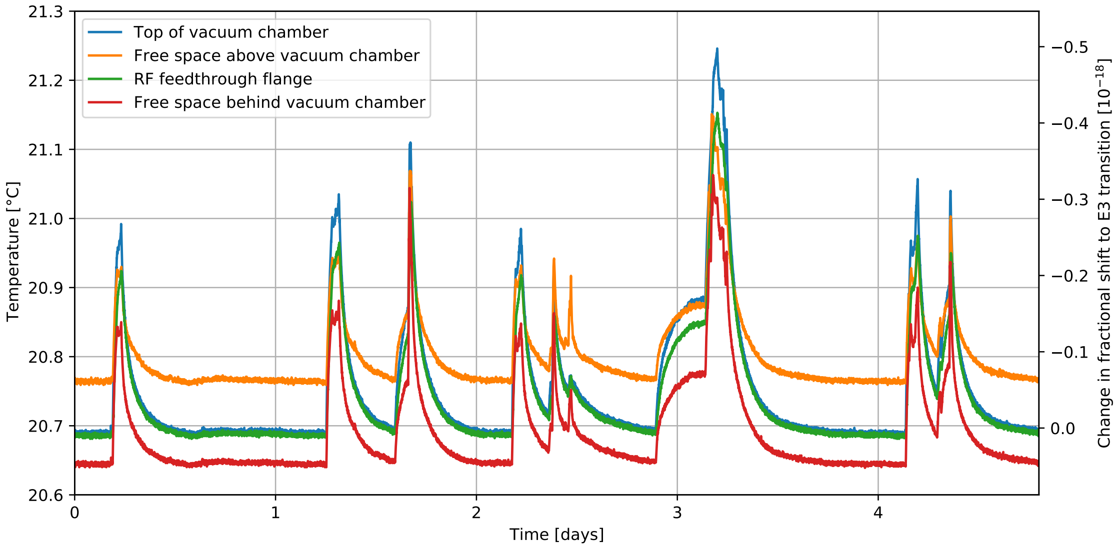

Figure 4.8: Temperature measurement in four locations around the vacuum chamber throughout a clock measurement period.

to calculate the shift during the whole period. Now, the analysis is automated with Python in the following way. The temperature data is filtered by the clock uptime which, just like for the AC Stark shift, is automatically determined based on fluorescence levels and excitation fraction. It is then possible to choose whether the correction should be applied to the second-by-second clock data, or if an average BBR shift should be produced. In both cases, the uncertainty on the BBR shift is calculated using the standard deviation of the temperature during the uptime. This analysis was automated after the three campaigns described in chapter 6 took place, and therefore all the BBR shift results reported are based on the previous more manual analysis.

4.6 Other shifts

This section will describe all the other relevant frequency shifts to the clock transition frequency whose measurement or analysis are either not yet fully automated, or not yet evaluated at all. Static shifts that do not need to be re-evaluated after each clock measurement will also be briefly described.

4.6.1 Phase noise shift

The 467-nm light passes through two fibres and two AOMs before reaching the ion. In the two fibres and the short lengths of free space, the light can accumulate phase noise, and additionally, when the light passes through the clock AOM which is continuously switching on and off, the thermal effects in the crystal can cause a phase chirp which would also lead to a frequency shift. For this reason, a PLS setup is in place to cancel out the phase noise from the 467-nm light, as described in section 2.4.

Because the phase noise is compensated, the shift is set to zero and only the uncertainty must be evaluated. A constraint on the uncertainty can be placed by observing the beat signal between the light in the main path and a short reference path. Note that the phase noise is yet to be compensated in the PCF and in the free space between the PCF output and the ion. However, it is known that the amount of phase noise accumulated in the PCF is negligible thanks to both its hollow core and the high level of temperature control in the laboratory.

4.6.2 Trap-drive-induced Zeeman shift

The RF currents in the trapping electrodes can generate AC magnetic fields that could lead to an additional second-order Zeeman shift [165]. In principle, for the Paul end-cap trap design in use, the RF electrodes are symmetric, thus it is expected for the shift to be zero. However, this must still be verified experimentally and the uncertainty needs to be quantified. The measurements for the evaluation of this shift and uncertainty are in progress at the time of writing.

4.6.3 Servo offset

The ultrastable cavity that transfers its stability to the clock laser is not perfect. Any cavity noise would correspond to frequency noise on the blue light that probes the ion. Furthermore, the cavity drift is the reason why in the locking algorithm the clock AOM must alternate in probing the high and low side of the transition. The best estimate of the cavity drift is only recalculated at the end of each servo cycle, meaning that the best guess of the transition centre frequency will always be lagging behind. The uncertainty in this estimate throughout the locking algorithm leads to a servo offset uncertainty ($\sim 1 \times 10^{-19}$ for the E3), which is calculated by simulating hundreds of finite locks to the clock transition with known cavity drift and noise parameters, and taking the standard deviation of the mean frequency offset.

4.6.4 Static shifts

Finally, the remaining systematic shifts are static and are not constantly re-evaluated for the current ion trap, as they depend respectively on the position of the ion in space and on the vacuum chamber properties.

Gravitational redshift As previously mentioned in section 1.6.3, the difference in transition frequency between two clocks is sensitive to their relative gravity potential, which must therefore be known at a good level of precision. A combination of geometric levelling and GNSS methods [122] were used to determine the height of the ion above the geoid at a 3-cm precision, allowing the gravitational redshift to be evaluated relative to a common reference level, opening up the possibility to compare clocks in different parts of the world. Since 2019, the position of the trap has not changed, such that the gravitational redshift has remained constant and equal to $(1186.92 \pm 2.45) \times 10^{-18}$.

Collisional shift Given that the vacuum in the chamber is not perfect, there is a possibility that a molecule from the vacuum chamber's background gas could collide with the trapped ion, temporarily shifting the clock transition frequency. Based on the Langevin collision model [166], it was found that these collisions occur at a rate of 1.5 h^{-1} in this vacuum chamber [7]. A conservative estimate is made by setting the uncertainty to the largest possible frequency shift caused by background collisions, such as 6×10^{-19} fractionally. Because the vacuum chamber pressure is extremely stable, this shift only needs to be evaluated once.

4.7 Conclusion

This chapter has covered in varying levels of detail all the known systematic shifts that the clock transition frequency can experience. Almost all of the systematic shift and uncertainty analyses have been completely automated and each made into version-controlled Python packages, giving full traceability to the results. After creating a configuration file in which the required input arguments are defined for each systematic (mostly consisting of experiment IDs) during a particular clock measurement period, the uncertainty budget can be produced with the click of a button. Together with my major role in the development of the overarching systematics combining software, the systematics whose evaluation I fully automated are the electric quadrupole shift, the second-order Zeeman shift, the residual probe-induced AC Stark shift and the AC Stark shift from the power overshoot. I also made a significant contribution to the automation of the BBR shift.

Furthermore, it has been shown how the measurement and calibration of several systematic shifts have been automated and significantly simplified by the implementation of the ARTIQ control system and the InfluxDB database. My largest contribution was the creation of the quadrupole shift dual-servo measurement routine. I also worked on the magnetic field calibration routine, particularly on simplifying the selection of input arguments, giving flexibility to the choice of magnetic fields to scan, automatically evaluating the coil currents required from the latest magnetic field background, and automatically determining the new background at the end of the series of scans.

Finally, I designed, developed and executed the novel quadrupole shift measurement and analysis method described in detail in this chapter. The motivation behind developing a method to directly measure the quadrupole shift rather than averaging it out to zero during the clock measurement by probing the transition in three orthogonal magnetic fields is to simplify the analysis of frequency ratios between different clocks, which would be more complex if three alternating frequency levels were being provided by our clock.

5 Absolute frequency measurements via TAI

5.1 Introduction

The current definition of the SI second is based on a hyperfine transition of frequency 9 192 631 770 Hz in the Cs atom. With optical atomic clocks now outperforming Cs primary standards by over two orders of magnitude both in terms of accuracy and stability [6, 167], it is anticipated that the second will soon be redefined based on an optical frequency. The sub-10^{-16} performance in optical clocks can only be demonstrated through frequency ratio measurements, in which the uncertainty contributions from both clocks are typically below the 10^{-16} level. However, any measurement of the absolute frequency of an optical transition is currently limited by the accuracy and stability coming from the Cs standard, since the frequency must be referenced directly to the SI second.

The Consultative Committee for Time and Frequency (CCTF) has set out a series of preliminary milestones towards the redefinition of the second [87]. Part of these objectives is the measurement of the absolute frequency of optical transitions with minimal uncertainty, to ensure that a change to an optical definition of the second would not introduce a discontinuity in the value of the SI second. One measurement method relies on the direct comparison of the optical frequency with a Cs fountain clock. Alternatively, the frequency of an optical clock can be measured with reference to the SI second realised by TAI [92–96].

5.1.1 Time scales

There are several time scales and references that are associated with the computation of TAI, summarised in Fig. 5.1, and described below.

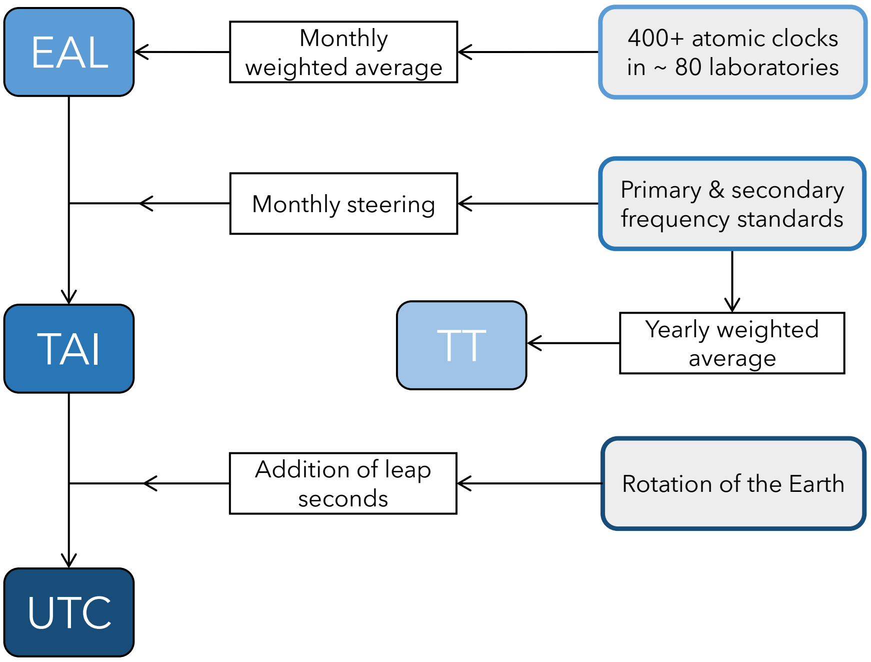

Figure 5.1: Diagram summarising the methods of computation of the various time scales described in section 5.1.1.

Échelle Atomique Libre (EAL) The free running atomic time scale EAL is realised monthly as the weighted average of hundreds of contributing atomic clocks. This ensemble average provides a very stable time scale. EAL is subsequently compared with the primary and secondary frequency standards that were operating during that month, which provide the accuracy of the time scale. This comparison allows for a frequency steering correction to be applied to EAL such that TAI conforms to the definition of the SI second [168, 169]. It is because of this regular steering and calibration by multiple primary standards that TAI is an advantageous reference for an absolute frequency measurement as opposed to a local Cs atomic clock.

International Atomic Time (TAI) TAI was proposed by CCTF to be defined as a coordinate time scale, referenced to the SI second realised on the rotating geoid. It is a virtual time scale which is computed monthly by the BIPM from EAL and primary and secondary frequency standards. The results are published by BIPM in the bulletin *Circular T* [170], which gives the time offsets between each local realisation and TAI which are reported at 5-day intervals.

Although the majority of atomic clocks that contribute to steering TAI are based on the Cs primary standard, more recently several species of ions and atoms with an optical clock transition have been identified to be suitable secondary representations of the second [86, 87], such that they can also start contributing to the computation of TAI as secondary frequency standards. One of the milestones proposed by CCTF for the redefinition of the second involves the regular contribution of optical clocks to the calibration of TAI. After the redefinition, optical clocks would be able to contribute to TAI with a significantly reduced uncertainty.

Coordinated Universal Time (UTC) UTC is the time standard that is most commonly used for international timekeeping. UTC and TAI differ by a constant offset which has been 37 s since 1st January 2017 at 0 h, as announced by the International Earth Rotation and Reference Systems Service (IERS) [171]. This offset is increased every few years with the addition of a leap second to account for the slight slowdown of the rotation of the Earth. The distinction between TAI and UTC is made such that TAI remains a continuous atomic time scale, while UTC is closely linked to the "time of day" as judged by the Sun's position in the sky. The time offsets of UTC from the local realisation of the second in a given laboratory k are reported in *Circular T* in terms of UTC$-$UTC(k).

Terrestrial Time (TT) TT(BIPM) is defined as a coordinate time of a geocentric reference system whose scale unit is chosen to agree with the SI second on the rotating geoid [172]. While TAI is computed month by month, TT(BIPM) is computed yearly in post-processing based on a weighted average of all primary and secondary frequency standards' frequency measurements that have ever contributed to TAI since 1993. For this calculation, the stability of EAL is estimated for different time periods, and naturally improves over time [168, 169]. TT(BIPM) is also an estimate of the consistency and quality of the contributing primary and secondary frequency standards, since it allows for the comparison of the behaviour of a single frequency standard with the whole ensemble [173].

5.2 Absolute frequency measurement framework

In order to measure the absolute frequency of an optical clock transition via a link to TAI, the optical frequency is first measured by a frequency comb which is referenced to a 10 MHz signal from a H maser. This maser provides the local time scale UTC(NPL) and its frequency is continuously compared with TAI via satellite links. The maser is steered regularly such that its frequency deviation from UTC is minimised. The H maser is a convenient frequency reference thanks to its long-term reliability, good short-term stability and low phase noise [88]. Fig. 5.2 shows the chain of links that connects the optical clock frequency to the SI second.

The calculation of the absolute frequency of an optical clock transition referenced to the SI second via TAI can be therefore expressed as a product of frequency ratios, as shown by the equation below.

$$\frac{f_{\mathrm{Yb}^+}}{f_{\mathrm{SI}}} = \frac{f_{\mathrm{Yb}^+}}{f_{\mathrm{UTC(NPL)}}} \times \frac{f_{\mathrm{UTC(NPL)}}}{f_{\mathrm{TAI}}} \times \frac{f_{\mathrm{TAI}}}{f_{\mathrm{SI}}} \, . \tag{5.1}$$

This equation, however, would only be valid if the uptime of the optical clock were 100 % throughout the entire 1-month TAI computation period. Realistically, the operation of an optical clock includes a certain amount of downtime, the uptime will not necessarily be exactly aligned with the 5-day reporting periods, and it also would not cover the whole 1-month period over which TAI is computed. These factors need to be accounted for when evaluating the absolute frequency of the optical clock, and therefore Eq. (5.1) needs to be

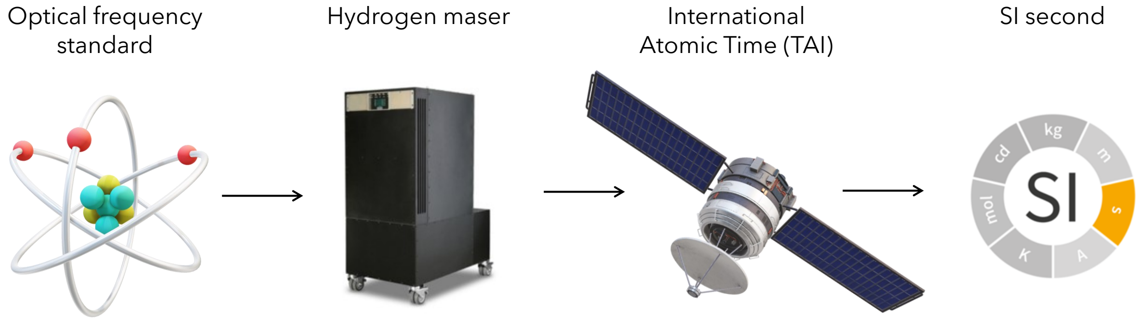

Figure 5.2: Diagram showing the steps of how an optical frequency is measured against TAI. The frequency from the optical clock is first measured by a frequency comb referenced to the signal from a H maser, which provides the local UTC realisation. This frequency is in turn compared to TAI via satellite links. The deviation of TAI from the SI second on the rotating geoid can finally be estimated.

expanded to the following form:

$$\frac{f_{\mathrm{Yb}^+}}{f_{\mathrm{SI}}} = \frac{f_{\mathrm{Yb}^+;\Delta t_1}}{f_{\mathrm{UTC(NPL)};\Delta t_1}} \times \frac{f_{\mathrm{UTC(NPL)};\Delta t_1}}{f_{\mathrm{UTC(NPL)};\Delta t_2}} \times \frac{f_{\mathrm{UTC(NPL)};\Delta t_2}}{f_{\mathrm{TAI};\Delta t_2}} \times \frac{f_{\mathrm{TAI};\Delta t_2}}{f_{\mathrm{TAI};\Delta t_3}} \times \frac{f_{\mathrm{TAI};\Delta t_3}}{f_{\mathrm{SI};\Delta t_3}}\ , \tag{5.2}$$

where Δt_i indicate the time intervals for which the respective frequency ratios are computed. Specifically, Δt_1 is the uptime of the $^{171}\mathrm{Yb}^+$ ion clock, Δt_2 corresponds to one or more 5-day TAI reporting periods that best align with the clock uptime, and Δt_3 is the 1-month TAI computation period. Fig. 5.3 shows the different time intervals used for the calculation of the absolute frequency of the $^2\mathrm{S}_{1/2} \rightarrow {}^2\mathrm{F}_{7/2}$ transition of $^{171}\mathrm{Yb}^+$ from data gathered during a frequency measurement campaign carried out in March 2020.

The general approach for the calculation of the ratios had already been established in the group at NPL; however, the evaluation of the absolute frequency used to be a laborious process that involved a large amount of manual processing. Furthermore, the calculation of the absolute frequency of $^{171}\mathrm{Yb}^+$ via TAI had only been done once at NPL [94]. My contribution in this regard revolves around the automation and generalisation of the absolute frequency calculation for any given optical clock transition measured at NPL. With this automated framework, new absolute frequency results have been produced from

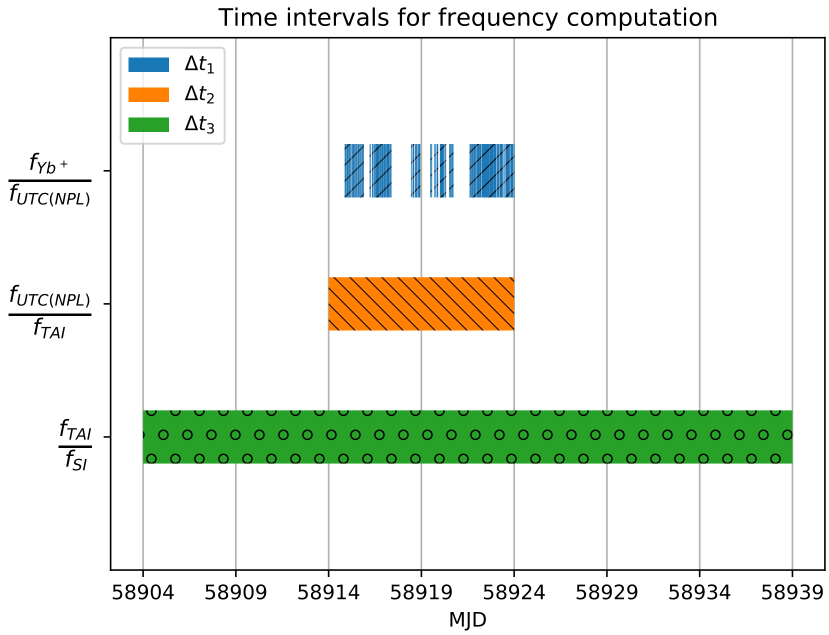

Figure 5.3: Time intervals for the computation of the corresponding frequency ratios. Δt_1 is the uptime of the ^{171}Yb$^+$ clock during the March 2020 measurement campaign, and is made up of a series of discontinuous time intervals. Δt_2 is made up of two 5-day TAI reporting periods (MJD 58914 - 58924), while Δt_3 covers the 1-month TAI computation period (MJD 58904 - 58939).

July 2019 and March 2022 ^{171}Yb$^+$ data. Furthermore, while some hardware glitches caused two out of the five ratios from Eq. (5.2) to be invalidated for the March 2020 ^{171}Yb$^+$ measurement (as explained in section 6.3), the uncertainty on the absolute frequency has been estimated for that dataset. The following sections will describe how each ratio and its uncertainty is evaluated based on sample data from the March 2020 measurement results. The features of the framework will be described, particularly emphasising the high level of automation in the evaluation of the absolute frequency.

5.2.1 Ratio at frequency comb: $f_{\mathrm{Yb}^+;\Delta t_1}/f_{\mathrm{UTC(NPL)};\Delta t_1}$

The light of the laser that probes the $^2\mathrm{S}_{1/2} \rightarrow {}^2\mathrm{F}_{7/2}$ optical transition of ^{171}Yb$^+$ is referenced to a 10 MHz signal produced by the H maser that generates the local time scale UTC(NPL).

The referencing is done using an optical frequency comb, whose repetition rate is measured against an 8 GHz reference which is synthesised by the 10 MHz signal from the maser. It is estimated that the uncertainty contribution to the frequency ratio measurement originating from the distribution and synthesis of the RF signal is of 1×10^{-16}.

The corrections to the systematic frequency shifts that affect the ion during the clock operation are applied for the computation of this ratio, and their corresponding uncertainties are accounted for. Furthermore, with the evaluation time interval for this ratio being Δt_1, the optical clock uptime, the statistical uncertainty due to the clock stability is also estimated for this period and considered as a contribution to the total uncertainty in the measurement.

5.2.2 Downtime corrections: $f_{\mathbf{UTC(NPL)};\Delta t_1}/f_{\mathbf{UTC(NPL)};\Delta t_2}$

In order to evaluate the second ratio in Eq. (5.2), we must account for the fact that for this measurement the uptime Δt_1 represents only 58 % of the time interval Δt_2 (MJD 58914 - 58924) for which *Circular T* provides an offset between $f_{\mathrm{UTC(NPL)}}$ and f_{TAI}. For this reason, it is necessary to extrapolate $f_{\mathrm{UTC(NPL)}}$ from Δt_1 to Δt_2 accounting for the downtimes in the data. Moreover, the frequency instability of the H maser that generates UTC(NPL) is affected by a linear drift and white and flicker noise, for which a deterministic and a stochastic correction need to be respectively applied.

Hydrogen maser noise model The stochastic frequency noise of the hydrogen maser measured during Δt_1 against $^{171}\mathrm{Yb}^+$ is used to create a model of the maser noise that can be used when extrapolating to different time periods, in this case for the period Δt_2. The relevant noise sources that contribute to the maser noise are the following:

- White phase noise $\sigma_y^{WPN}(\tau) = WPN/\tau$
- White frequency noise $\sigma_y^{WFN}(\tau) = WFN/\sqrt{\tau}$

- Flicker frequency noise $\sigma_y^{FFN}(\tau) = FFN$

where the parameters chosen for the noise model are respectively $WPN = 4 \times 10^{-13}$, $WFN = 14 \times 10^{-14}$ and $FFN = 9 \times 10^{-16}$.

Fig. 5.4 shows the noise model and the overlapping Allan deviation of the measured instability of the maser relative to the optical clock for a continuous set of measurement data $y(t)$ in fractional frequency units. The noise parameters were chosen such that the model would slightly overestimate the overall noise. The power spectral density $S_y(f)$ of the model is calculated as:

$$S_y(f) = \left(\frac{WPN}{\frac{\sqrt{3f_H}}{2\pi}}\right)^2 f^2 + \left(\frac{WFN}{\frac{1}{\sqrt{2}}}\right)^2 + \left(\frac{FFN}{\sqrt{2\ln 2}}\right)^2 f^{-1} \,. \tag{5.3}$$

The cutoff frequency f_H is set to 0.5 Hz for a sampling rate of 1 Hz to satisfy the sampling

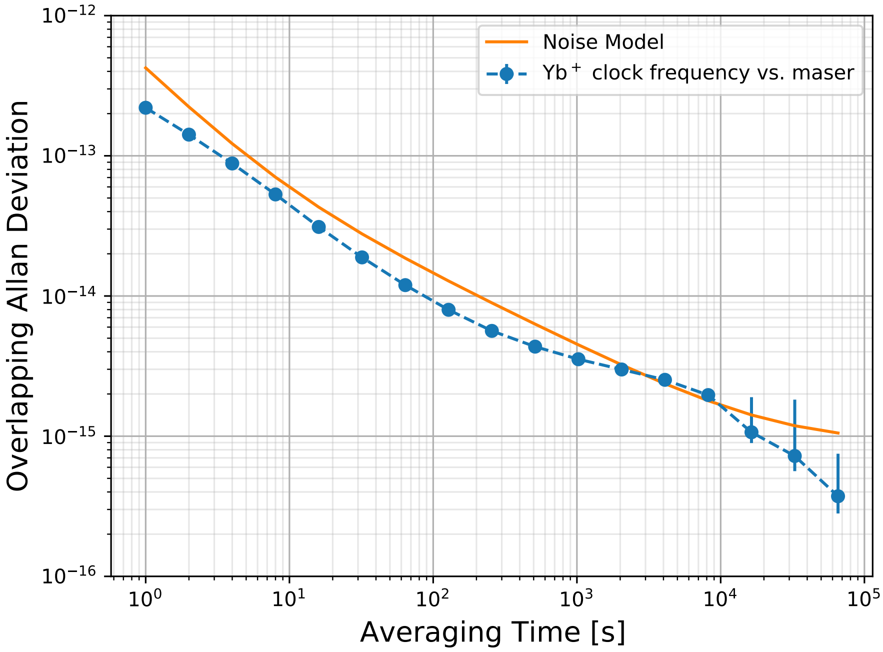

Figure 5.4: Hydrogen maser noise model based on a combination of white phase noise, white frequency noise and flicker frequency noise.

theorem, which requires the cutoff frequency to be smaller than or equal to half of the sampling rate (Nyquist frequency) [174]. A method similar to that described in Ref. [175] is employed to calculate the noise from Δt_1 to Δt_2. The root mean square (RMS) fluctuation σ_y for the full dataset of duration Δt_2 is defined in the frequency domain as:

$$\sigma_y^2 = \int_0^\infty S_y(f)df \ , \tag{5.4}$$

where the one-sided power spectral density can also be expressed as:

$$S_y(f) = \frac{|\mathcal{F}\{y(t)\}|^2}{\Delta t_2} \ , \tag{5.5}$$

where $\mathcal{F}\{y(t)\}$ is the Fourier transform of $y(t)$. For the dataset of duration Δt_1, the squared RMS is defined as:

$$\sigma_{y'}^2 = \int_0^\infty S_{y'}(f)df \ . \tag{5.6}$$

The dataset $y'(t)$ can be treated as the convolution of $y(t)$ with a temporal windowing function $w(t)$ defined as:

$$w(t) = \begin{cases} 1 & \text{for } t \in \Delta t_1 \\ 0 & \text{elsewhere.} \end{cases} \tag{5.7}$$

Therefore,

$$S_{y'}(f) = \frac{|\mathcal{F}\{y(t) \circledast w(t)\}|^2}{\Delta t_1} = \frac{|\mathcal{F}\{y(t)\}\,\mathcal{F}\{w(t)\}|^2}{\Delta t_1} \ . \tag{5.8}$$

Combining equations (5.5) - (5.8):

$$\sigma_{y'}^2 = \frac{\Delta t_2}{\Delta t_1} \int_0^\infty S_y(f)\,|\mathcal{F}\{w(t)\}|^2 df \ . \tag{5.9}$$

Given that the data are sampled at a rate of 1 Hz, the previous expression is discretised in the following way:

$$\sigma_{y'}^2 = \frac{N}{N'} \sum_{n=1}^{N} S_y(f_n)\,|\mathcal{F}\{w(t_n)\}|^2 \ , \tag{5.10}$$

where N is the total number of data points in the period Δt_2, and N' is the number of valid points (i.e. the data contained in the measurement period Δt_1). The RMS $\sigma_{y'}$ represents the stochastic uncertainty contribution of the maser during only the time intervals when the optical clock is operational.

Hydrogen maser drift and steers The frequency of the maser is drifting over time, and this drift is measured during the clock uptime Δt_1. The noise model from Fig. 5.4 does not account for this drift, since the power spectral density is hardly defined at longer timescales. Therefore, for the calculation of the ratio $f_{\mathrm{UTC(NPL)};\Delta t_1}/f_{\mathrm{UTC(NPL)};\Delta t_2}$, an additional correction needs to be applied for the extrapolation of the drift during Δt_2. Furthermore, the frequency of the maser is steered once every few days to counteract the drift, and therefore the frequency changes due to the steers must be accounted for in the calculation of the linear drift of the maser.

For each day of data, the average maser frequency relative to the optical clock is calculated over that day's uptime, and a centre-of-mass MJD is calculated for each day based on the uptime. The fractional uncertainty on the daily average frequency is calculated with a quadrature sum of the uncertainties from the maser noise model parameters:

$$\sigma_{\mathrm{tot}}(\tau) = \sqrt{\sum_i \left(\sigma_y^{\mathrm{noise}_i}(\tau)\right)^2} = \sqrt{\left(\sigma_y^{WPN}(\tau)\right)^2 + \left(\sigma_y^{WFN}(\tau)\right)^2 + \left(\sigma_y^{FFN}(\tau)\right)^2}\,, \tag{5.11}$$

with τ equal to the given day's uptime in seconds. Fig. 5.5 shows these daily data points, together with a fit to the data that accounts for the maser steers (dotted orange line) and an indication of the uptime of the optical clock during that period (green segments). The downtime correction is calculated from the fit data as the difference between the mean frequency of the maser during the uptime Δt_1 and the mean frequency during the entire measurement period Δt_2 (respectively the means of the green segments and dotted orange line in Fig. 5.5).

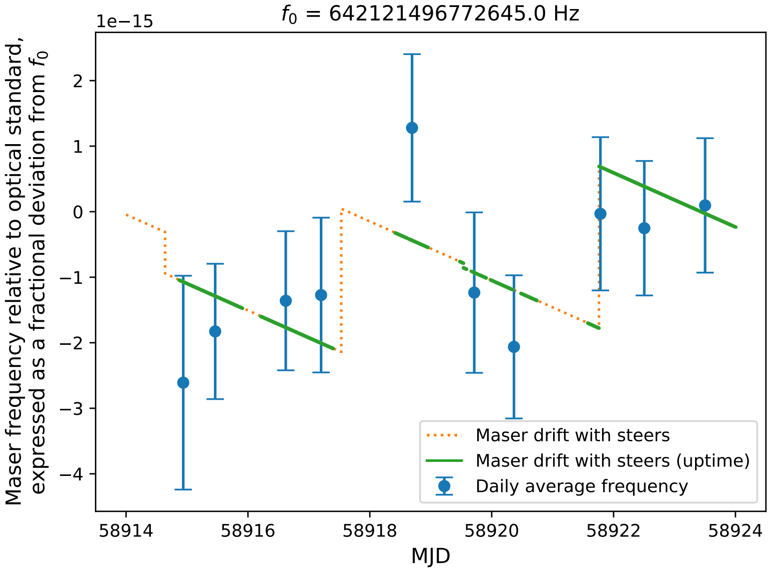

Figure 5.5: Maser frequency measured in March 2020 relative to $^{171}\text{Yb}^+$ offset from the BIPM reference frequency f_0. The blue points represent the daily average of the frequency. The dotted orange line is the fit to the maser frequency in which the steers have been accounted for. The green segments indicate the uptime of the measurement.

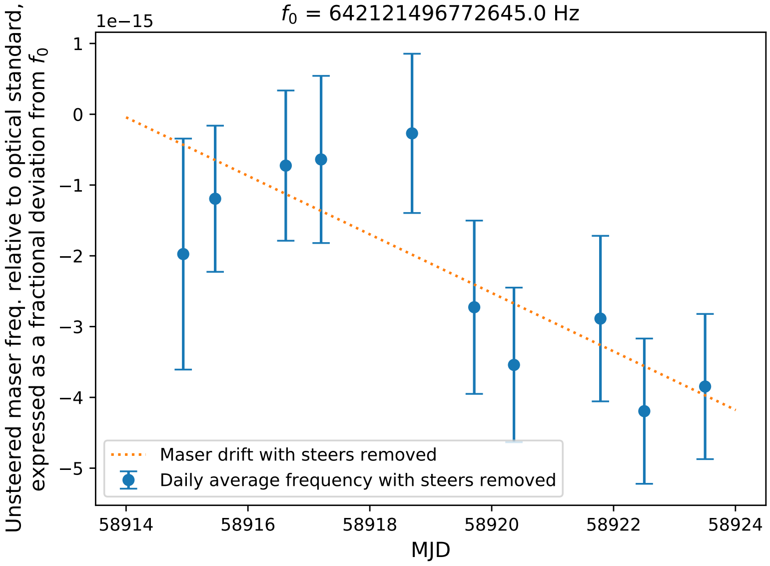

Figure 5.6: Maser frequency with steers removed measured relative to $^{171}\text{Yb}^+$ offset from the BIPM reference frequency f_0. The blue points represent the daily average of the frequency after the maser steers have been removed. The dotted orange line is the fit to the maser frequency, from which its linear drift can be extracted.

In order to produce the fit shown by the orange line, the value of each frequency steer is subtracted from the maser frequency measurements relative to the optical clock, revealing the maser's natural linear drift. The daily average unsteered maser frequency is calculated, and a weighted linear fit is performed on it to extract the maser drift rate, as seen in Fig. 5.6. The frequency steers are then re-applied where they had been subtracted previously, such that the fitted drift rate follows the real measured data accounting for the steers, as shown in Fig. 5.5.

5.2.3 Deviation of UTC(NPL) from TAI: $f_{\mathbf{UTC(NPL)};\Delta t_2}/f_{\mathbf{TAI};\Delta t_2}$

The *Circular T* bulletin by BIPM is a monthly publication that provides timing offsets between UTC and the local realisations of the time scale in the various contributing laboratories. The reason why the H maser that generates UTC(NPL) is regularly steered is for the minimisation of the timing offset from UTC, which would otherwise increase at the rate of the maser's linear drift. The timing offsets are reported in nanoseconds at 5-day intervals, which determine the time periods that the optical frequency measurements need to overlap with. The timing offsets are converted to a mean fractional frequency deviation of UTC(NPL) from TAI for the series of 5-day periods considered. This is done by calculating a mean accumulated timing offset over the duration of the measurement period, and dividing by the duration of a 5-day period:

$$-\frac{1}{N}\sum_{i=1}^{N}\frac{t_{i+1}-t_i}{T_0}\,, \tag{5.12}$$

where N is the number of 5-day periods, t_i is a timing offset reported at epoch i, and $T_0 = 4.32\times10^{14}$ ns, equivalent to 5 days. The uncertainty associated with the accumulated timing offset is calculated as [176]:

$$\left(\frac{\sqrt{u_A(\mathrm{NPL})_i^2 + u_A(\mathrm{NPL})_f^2}}{T_0}\right)\left(\frac{T_0}{T}\right)^{0.9}\,, \tag{5.13}$$

where $u_A(\mathrm{NPL})$ is the uncertainty in nanoseconds coming from the instability of NPL's link to TAI, i and f indicate respectively the initial and final 5-day reporting period considered, and $T = t_f - t_i$ is the total duration of the absolute frequency measurement. A single value for the uncertainty $u_A(k)$ for a laboratory k is reported for any given 1-month reporting period, so Eq. (5.13) effectively becomes:

$$\left(\frac{\sqrt{2}u_A(\mathrm{NPL})}{T_0}\right)\left(\frac{T_0}{T}\right)^{0.9} . \tag{5.14}$$

5.2.4 Deviation of TAI from the SI second: $f_{\mathbf{TAI};\Delta t_3}/f_{\mathbf{SI};\Delta t_3}$

TAI differs from the SI second on the rotating geoid by a fractional deviation known as a d value. BIPM computes d for each 1-month interval based on measurements from several primary frequency standards [177]. The d values are reported monthly in the *Circular T* bulletins; however, when the yearly timescale TT(BIPM) is computed, that year's monthly d values are recalculated in post-processing. Ref. [178] reports all the monthly d values between 2018 and 2020. The d value is directly added as a correction to the absolute frequency. If the time interval Δt_3 for which d is computed exactly matches up with Δt_2, then the only uncertainty on this offset comes from the computation of d.

EAL extrapolation: $f_{\mathbf{TAI};\Delta t_2}/f_{\mathbf{TAI};\Delta t_3}$ If $\Delta t_3 \neq \Delta t_2$, an additional uncertainty must be considered due to the extrapolation of the frequency of TAI to a different time period, indicated by the ratio $f_{\mathrm{TAI};\Delta t_2}/f_{\mathrm{TAI};\Delta t_3}$. This uncertainty is calculated based on a model for the instability of the free-running time scale EAL, whose relation to TAI is given in Ref. [179]. The method for the calculation is the same as for the stochastic downtime uncertainty outlined in section 5.2.2, relying on a Fourier transform of a temporal windowing function multiplied by the power spectral density of the noise model. In this case, the windowing function is defined for the duration Δt_3 (the computation period of d) as:

$$w(t) = \begin{cases} 1 & \text{for } t \in \Delta t_2 \\ 0 & \text{elsewhere.} \end{cases} \tag{5.15}$$

The noise model of EAL used to calculate the power spectral density is made up of white frequency noise, flicker frequency noise and random walk frequency noise components summed in quadrature. The values of these parameters are provided by BIPM for various years [178]; between 2018 and 2020 they take the following values:

- White frequency noise $\sigma_y^{WFN}(\tau) = 14 \times 10^{-16}/\sqrt{\tau}$
- Flicker frequency noise $\sigma_y^{FFN}(\tau) = 2 \times 10^{-16}$
- Random walk frequency noise $\sigma_y^{RWFN}(\tau) = 2 \times 10^{-17}\sqrt{\tau}$

5.2.5 Level of automation in the calculation

The ratios explained in the previous sections are finally multiplied together according to Eq. (5.2) and their fractional uncertainties are added up in quadrature. All these calculations are implemented in the framework that evaluates the absolute frequency of the transition frequency and its associated uncertainty. The program relies on a set of input data that needs to be provided by the user - this is the only manual part of the processing involved in the calculation.

For the calculation of the ratio $f_{\mathrm{Yb}^+;\Delta t_1}/f_{\mathrm{UTC(NPL)};\Delta t_1}$ and its uncertainty, data files containing second-by-second optical frequency measured by the comb relative to the maser are used, together with a systematic correction and uncertainty, and a statistical uncertainty. The dataset is masked by a validity array that is in most part determined by the uptimes of the optical clock and filtering of the comb measurement. This type of file has straightforward requirements and can be generated for any particular measurement period and optical clock transition measured.

In order to evaluate the correction and uncertainty related to the drift and instability of the hydrogen maser and the measurement downtime, the values of the three noise parameters need to be inputted, and a list of timestamped maser frequency steers needs to be provided. The remainder of the analysis relies on readily available data provided by BIPM, such as the *Circular T* bulletin for the relevant month which reports the time offsets between UTC and its local realisations, and the monthly d value. BIPM also provides the relationship between EAL and TAI and the noise parameters that define the instability of EAL. The framework also allows the calculation of the additional uncertainty coming from the EAL extrapolation to be bypassed if custom d values were to be provided by BIPM for a time interval of interest.

The program is then able to process these input data and outputs the results in a human-readable template, in which the contributions from each ratio are reported, and a total absolute frequency offset from the BIPM recommended frequency is produced. It is worth noting that all the systematic corrections and uncertainties for the $^{171}\mathrm{Yb}^{+}$ optical clock that contribute to the first ratio $f_{\mathrm{Yb}^{+};\Delta t_1}/f_{\mathrm{UTC(NPL)};\Delta t_1}$ are also computed in an automated manner, as explained in chapter 4.

5.3 Conclusion

This chapter outlined the different steps that need to be taken in order to reference an optical frequency measurement to the SI second via a link to TAI. It was shown that the main difficulty in the analysis arises from having to extrapolate the discontinuous optical clock measurement to the continuous one-month TAI evaluation period.

While part of this analysis framework was developed by another member of the team, I worked on generalising it to process any set of optical clock data; I implemented the consideration of maser steers in the evaluation of the deterministic downtime correction; and I included the uncertainty for extrapolating EAL when the measurement period does not exactly match the period for which the d value is reported by *CircularT*. Finally, I concentrated on the automation aspect of the framework, ensuring that an absolute frequency result could be produced for a particular measurement dataset with minimal manual input from the user.

With the full calculation of the absolute frequency via TAI now fully automated and generalised, this evaluation can now be easily and quickly performed on historical and future data. The following chapter will present the key results from the three clock measurement campaigns, including the absolute frequencies measured via TAI. In the future, in order for our optical clocks to be regularly contributing to TAI as secondary frequency standards, the automation of the calculation of their frequency relative to the H maser will become indispensable, as it will significantly ease the process of providing monthly results.

6 Clock measurement campaign results

6.1 Introduction

An essential requirement to demonstrate the level of performance of an optical clock is a measurement in which its frequency is compared to that of another optical clock. This measurement is ideally performed through an optical fibre link, such that the two clock frequencies can be directly compared using a frequency comb. When two optical frequencies are measured by the same frequency comb, the contribution from the maser which the comb is referenced to cancels out, such that the accuracy of the frequency ratio measurement is in principle only limited by the level of systematic uncertainty of both clocks. However, the measurement needs to also be carried out for a long enough duration in order for a high level of frequency stability to be achieved, and thus it is very important for the uptime of both optical clocks to be maximised throughout a measurement period.

Optical clock measurements require a significant amount of time for preparation and subsequent data analysis and systematic shift characterisation. In order to maximise the amount of data gathered during one measurement, and at the same time allowing for enough spare time for experimental upgrades, international measurement campaigns are carried out typically once a year in which multiple NMIs run their optical clocks for an agreed measurement period, which can range from a week to a month depending on the clock comparison technique.

As mentioned in section 1.5.2, a European optical fibre link network is currently in place connecting the NMIs in the United Kingdom, France, Germany and Italy, enabling the direct comparison of several optical clocks. It has been demonstrated that these intercontinental optical fibre links achieve an exceptional level of stability for frequency comparisons [153], and are in principle not a limiting factor in the measurement. Furthermore, local optical fibre links enable direct comparisons between different optical clocks within the same NMI. For laboratories outside of the fibre link network, optical clock frequencies can still be compared via satellite links, but with higher uncertainty, which is typically comparable to the uncertainty on the current realisation of the SI second.

Although frequency ratio measurements are important to set a baseline on the achievable accuracy of optical clocks, the SI second will eventually be redefined in terms of an absolute frequency of an optical transition. It is therefore crucial to measure absolute frequencies of optical transitions and they must be consistent within the uncertainty of the current realisation of the second in order to ensure continuity after the redefinition. Therefore, these campaigns are typically scheduled to align with TAI reporting periods in order to minimise the uncertainty in the link between the local time scale and TAI. Moreover, the optical clock frequency can also be compared to any local Cs fountain clock running at the same time, resulting in a different type of absolute frequency measurement that is expected to be consistent with the measurement via TAI.

The typical campaign operation of the $^{171}\mathrm{Yb}^{+}$ optical clock at NPL is the following. The campaign period consists of a series of dual-servo locks to the E3 transition which are interrupted typically once or twice a day to make a measurement of the magnetic fields and of the micromotion, and subsequently minimise their systematic effects for the following E3 lock. During the campaign period, PT100 sensors continuously measure the temperature around the vacuum chamber for the determination of the BBR shift. Both before and after the campaign period, a measurement of the E2 transition is carried out to determine the quadrupole shift, as explained in section 4.3. Finally, all other systematic shifts are measured and accounted for in post-processing.

Throughout my time at NPL, I have contributed to three measurement campaigns, each of which will be covered in this chapter. The experimental upgrades and changes between each campaign will be described, and the key results from each one will be presented. These will include systematic uncertainty budgets, measurements of the absolute frequency of the E3 transition, and local frequency ratios between the $^{171}\mathrm{Yb}^{+}$ and $^{87}\mathrm{Sr}$ optical clocks.

Remote frequency ratios between NPL ^{171}Yb$^+$ and optical clocks in other institutes will not be presented here as the results have not yet been released for publication by the other institutes. Thanks to the high level of experimental and analysis automation in the final campaign, an optically-steered prototype time scale was demonstrated for the first time at NPL. Finally, shortly after the end of the final campaign, an interleaved measurement of the E3 and E2 transitions was carried out in order to produce their frequency ratio.

6.2 2019 campaign

The 2019 international clock comparison campaign took place for two weeks between June and July and involved optical clocks from NPL, PTB and SYRTE connected via fibre links. During this campaign, the ^{171}Yb$^+$ optical clock experiment at NPL was still under the LabVIEW control system, and routine calibration measurements such as micromotion minimisation and magnetic field calibration involved a lot of manual intervention as mentioned in chapter 4. The analysis of the systematic shifts was also still performed manually, as the analysis automation had not been implemented yet. Moreover, the validation of the clock uptimes was also carried out manually and in post-processing, by qualitatively checking the fluorescence level and clock excitation fraction throughout a lock.

This campaign was carried out not only for metrological purposes, but also with the goal to detect common oscillations and transient variations of the fine structure constant caused by the presence of dark matter. This was an additional reason that motivated the development of the new quadrupole shift measurement method that would then allow the ^{171}Yb$^+$ E3 clock to run at a single frequency level in one magnetic field direction instead of three, such that the dark matter analysis could be carried out more straightforwardly. For this campaign's quadrupole shift measurement, the E2 frequency in five different magnetic fields was compared to the local ^{87}Sr clock frequency acting as a stable reference instead of a second interleaved E2 servo.

6.2.1 Uncertainty budget

The uncertainty budget from the 2019 E3 measurement is displayed in Table 6.1. The contribution from each individual systematic effect is presented, and the combination of all fractional shifts is calculated to be $-96.0 \pm 6.9 \times 10^{-18}$, where the uncertainty on the total is the result of adding in quadrature each uncertainty contribution.

The uncertainty budget is dominated by the quadrupole shift uncertainty. For this campaign, no search was carried out for the optimal values of the four trap-electrode voltages producing the electric field gradient, which might have contributed to the large uncertainty. Moreover, the quadrupole shift was measured once before and once after the E3 campaign, and the "before and after" values did not agree within their uncertainties. This was found to be due to an unknown hardware failure that occurred towards the end of the campaign, diagnosed from the detection of an unusually high spike in the micromotion

Systematic effect	$\Delta\nu/\nu_0 \times 10^{-18}$	$\sigma/\nu_0 \times 10^{-18}$
Electric quadrupole	1.7	6.2
Phase chirp of blue AOMs	0	2.2
Black-body radiation	-66.4	1.2
Servo offset	0	0.9
Collisions with background gas	0	0.6
Second-order Zeeman (DC)	-29.4	0.6
AC Stark from 467-nm beam	0	0.4
Second-order Doppler	-1.3	0.4
Second-order Zeeman (AC)	-0.3	0.1
AC Stark from 467-nm power overshoot	0	0.1
Trapping RF Stark	-0.31	0.09
AC Stark from leakage light	< 0.01	< 0.01
Trap-drive-induced AC Zeeman	N/A	N/A
Total	**-96.0**	**6.9**

Table 6.1: Uncertainty budget of the E3 clock transition frequency of ^{171}Yb^{+} during the 2019 measurement campaign (excluding the gravitational redshift). Note that the trap-drive-induced AC Zeeman shift has not yet been evaluated, but is expected to be consistent with zero within the uncertainty.

drift. Because the micromotion is also controlled by the trap electrodes, a large change in their optimum values targeting minimum micromotion meant that the resulting electric field gradient would also be different, making the "before and after" quadrupole shift measurements different. For this reason, the uncertainty was additionally inflated to account for this unknown effect.

6.2.2 Local optical frequency ratio results

The ratio between the $^{171}\mathrm{Yb}^{+}$ E3 and $^{87}\mathrm{Sr}$ optical clocks at NPL over the campaign measurement period is shown in Fig. 6.1a. The overlapping Allan deviation is shown in Fig. 6.1b, and was produced using the Python package *allantools*. For a conservative estimate of the stability of the ratio, the last point of the Allan deviation was removed, and a weighted linear fit was performed to the points from $\tau \geq 10^3$ s. The last point of the fit is then considered to be the statistical uncertainty on the ratio. The value of the ratio for this measurement is calculated as the simple unweighted average of all the data, leading to $r = 1.495\,991\,618\,544\,900\,531(25)$, where the uncertainty is the sum in quadrature of the systematic and statistical uncertainties on the ratio, shown in Table 6.2.

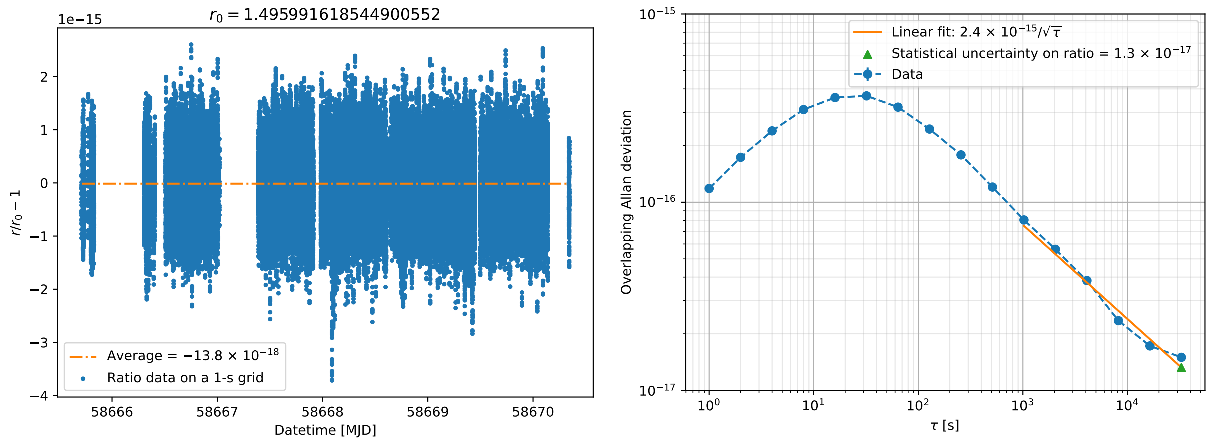

(a) Ratio offset from r_0.

(b) Overlapping Allan deviation.

Figure 6.1: NPL $^{171}\mathrm{Yb}^{+}$ E3 to $^{87}\mathrm{Sr}$ ratio results from the 2019 campaign.

Uncertainty contribution	$\sigma/r_0 \times 10^{-17}$
Statistical	1.3
Yb^+ E3 systematics	0.69
Sr systematics	0.82
Local height difference	0.12
Total	**1.69**

Table 6.2: Statistical and systematic fractional uncertainty contributions to the NPL $^{171}Yb^+$ E3 to ^{87}Sr ratio measured in July 2019, where $r_0 = 1.495\,991\,618\,544\,900\,552$.

6.2.3 Absolute frequency results

While this campaign did not represent an ideal measurement for the calculation of the absolute frequency of the E3 transition of $^{171}Yb^+$ via TAI due to its limited duration and a poor alignment with the 5-day reporting periods, it is still a valid measurement, even though the uncertainties are slightly higher. The uptime Δt_1 spans the period MJD 58665.714734 - 58670.340231, whereas the boundaries for the relevant 5-day TAI reporting periods are on MJD 58664, 58669 and 58674. The analysis is carried out for two time periods, spanning respectively one and two 5-day TAI intervals, in order to determine which one results in the lowest uncertainty.

During the 5-day period Δt_2 = MJD 58664 - 58669, the uptime is 56 %, compared to the 40 % uptime over the 10-day period Δt_2 = MJD 58664 - 58674 (see Fig. 6.2). A lower uptime in the measurement period means that the stochastic noise contribution from the maser will be larger, since it is inflated by the inverse of the fractional uptime. The fractional stochastic maser noise contribution associated with extrapolating the optical to maser ratio data to match TAI intervals is in fact 5.66×10^{-16} for the 10-day period, compared to 3.94×10^{-16} for the 5-day period.

On the other hand, the deterministic downtime correction from the linear drift of the maser can be calculated more accurately with more data points available to fit. Fig. 6.3 shows the maser frequency relative to $^{171}Yb^+$ with the fit to the drift for the two time periods. For the 5-day period, the fractional deterministic downtime correction is calculated to be $(-2.14 \pm 4.96) \times 10^{-16}$, as opposed to $(-5.88 \pm 2.74) \times 10^{-16}$ for the 10-day period.

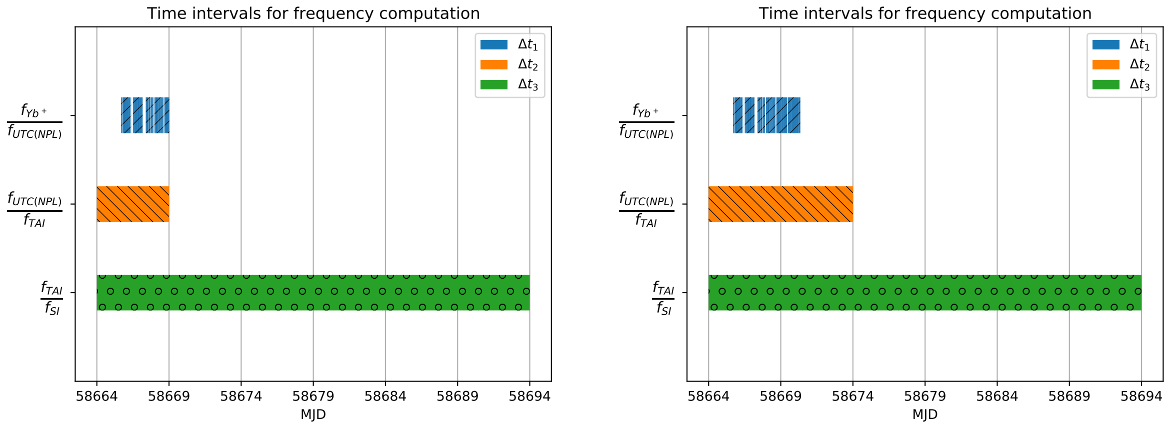

(a) Δt_2 = MJD 58664 - 58669 (5-day period).

(b) Δt_2 = MJD 58664 - 58674 (10-day period).

Figure 6.2: Time intervals for the computation of the corresponding frequency ratios for two different periods Δt_2. Δt_1 is the uptime of the ^{171}Yb$^+$ clock during the July 2019 measurement campaign, and is made up of a series of discontinuous time intervals. Δt_3 covers the 1-month TAI computation period (MJD 58864 - 58894).

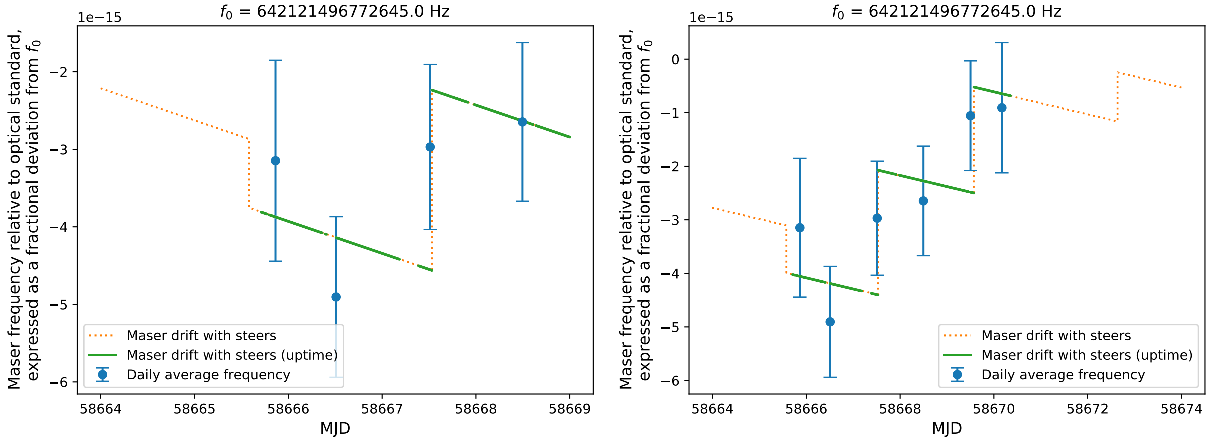

(a) Δt_2 = MJD 58664 - 58669 (5-day period).

(b) Δt_2 = MJD 58664 - 58674 (10-day period).

Figure 6.3: Maser frequency measured in July 2019 relative to ^{171}Yb$^+$ offset from the reference frequency f_0. The blue points represent the daily average of the frequency. The dotted orange line is the fit to the maser frequency in which the maser steers have been accounted for, showing the expected behaviour of the daily absolute frequency offset. The green segments indicate the uptime of the measurement.

The largest contribution to the uncertainty on the absolute frequency measurement for both time intervals comes from the deviation of UTC(NPL) from TAI. The uncertainty on this offset is inversely proportional to the duration of the computation period. The correction to the ratio $f_{\mathrm{UTC(NPL)};\Delta t_2}/f_{\mathrm{TAI};\Delta t_2}$ is $(-4.63 \pm 16.37) \times 10^{-16}$ for the 5-day period, while it is $(2.31 \pm 8.77) \times 10^{-16}$ for the 10-day period. Because this is the dominant uncertainty contribution, the absolute frequency measurement over MJD 58664 - 58674 is chosen rather than the 5-day period because of its higher accuracy, despite the lower fractional uptime.

The resulting absolute frequency is $f_{\mathrm{Yb}^+} = 642\,121\,496\,772\,645.39(70)$ Hz, which is in good agreement with the 2021 BIPM recommended frequency of 642 121 496 772 645.12(12) Hz. The results from each individual ratio in Eq. (5.2) are displayed in Table 6.3. Note that all the ratios in the table are expressed in terms of $(r/r_0 - 1)$, i.e. as a fractional offset from a nominal value r_0. This is common practice in metrology and removes the complexity of carrying around a large number of digits in calculations.

Ratio	**Contribution**	$\mathbf{r_0}$	$\left(\frac{\mathbf{r}}{\mathbf{r_0}} - \mathbf{1}\right) \times \mathbf{10^{18}}$	$\mathbf{u}\left(\frac{\mathbf{r}}{\mathbf{r_0}} - \mathbf{1}\right) \times \mathbf{10^{18}}$
$\frac{f_{\mathrm{Yb}^+;\Delta t_1}}{f_{\mathrm{UTC(NPL)};\Delta t_1}}$	Ratio at comb	642 121 496 772 645.0	2154	100
	$^{171}\mathrm{Yb}^+$ statistical		–	7
	$^{171}\mathrm{Yb}^+$ systematics		549	7
	Gravitational redshift		−1187	2
$\frac{f_{\mathrm{UTC(NPL)};\Delta t_1}}{f_{\mathrm{UTC(NPL)};\Delta t_2}}$	Maser noise	1	–	566
	Maser drift		−588	274
$\frac{f_{\mathrm{UTC(NPL)};\Delta t_2}}{f_{\mathrm{TAI};\Delta t_2}}$	UTC(NPL) to TAI	1	231	877
$\frac{f_{\mathrm{TAI};\Delta t_2}}{f_{\mathrm{TAI};\Delta t_3}}$	EAL extrapolation	1	–	42
$\frac{f_{\mathrm{TAI};\Delta t_3}}{f_{\mathrm{SI};\Delta t_3}}$	TAI to SI second	1	−550	160
$\frac{f_{\mathrm{Yb}^+}}{f_{\mathrm{SI}}}$	Total	642 121 496 772 645.0	610	1096

Table 6.3: Values and uncertainties associated to each ratio that contributes to the absolute frequency calculation of the E3 transition of $^{171}\mathrm{Yb}^+$ over the period MJD 58664 - 58674 (July 2019) according to Eq. (5.2). r_0 is equal to the recommended value of the frequency of the E3 approved by the International Committee for Weights and Measures (CIPM) in 2015.

6.3 2020 campaign

The two-week-long clock comparison campaign that took place in March 2020 involved a few additional optical clock laboratories relative to the previous campaign. However, many of the remote comparisons could not be completed as COVID-19 lockdowns terminated the measurements. The major improvement for the $^{171}\mathrm{Yb}^{+}$ clock that came with this campaign was the automation of the analysis and evaluation of most systematic shifts and uncertainties. In addition, some improvements were made to the ytterbium ion experiment, which was still under LabVIEW control. The H, U, D shutters and the wave plate rotation mounts were implemented in the 370-nm laser setup, such that they could be remote controlled by a separate LabVIEW program that would complement the micromotion minimisation routine.

Furthermore, the quadrupole shift measurement was performed this time against a second interleaved E2 servo as opposed to the local strontium lattice clock which would have had to run concurrently. Although performing a dual-servo measurement means that twice the amount of data is necessary to reach a comparable level of stability, this allows for more testing and preparation since there is no dependence on the uptime of the strontium clock. Moreover, the determination of an optimal configuration of electrode voltages to minimise the quadrupole shift and its uncertainty (as described in section 4.3.1) was done just before the start of this campaign.

Finally, soon after the end of the campaign, an automated uptime-validation software was designed, moving away from the manual qualitative selection of the clock-uptime periods and taking a step forward in the direction of automated analysis. This software allowed the entirety of the clock frequency data to be filtered by its uptime, with the fluorescence level and the excitation fraction as the main metrics to validate the data.

Months after the end of the measurement campaign, a further analysis was carried out which revealed that one of the digital frequency dividers in the frequency comb setup was exhibiting some signal dropouts that were not being detected. These frequency dividers were in place to bring the frequency of the beat between the frequency comb and the clock laser frequency down to the appropriate range for the K+K counters to measure. An experiment was set up to detect these dropouts, and it was determined that the dropouts observed over this 17-hour measurement could have contributed to a fractional systematic offset on the $^{171}\mathrm{Yb}^{+}$ frequency at the 2×10^{-16} level. Because it is not possible to exactly quantify the systematic offset caused by the undetected dropouts during the actual clock measurement period, the optical clock data had to be completely invalidated. Although this means that the $^{171}\mathrm{Yb}^{+}$ clock data could not be used for any frequency ratio measurement, the following subsections will cover some results that still remain valid.

6.3.1 Uncertainty budget

All the measurements of the systematic effects experienced by the $^{171}\mathrm{Yb}^{+}$ ion during the campaign period still remain valid, as they are all completely independent of the frequency comb. The resulting uncertainty budget is displayed in Table 6.4. Thanks to the improvements that were made to the quadrupole shift measurement, its contribution in the uncertainty budget was significantly reduced since the year before. This uncertainty budget was also useful in setting an expectation for future measurements on what is achievable on this system, and in understanding what aspects of the experiment could be improved.

In this measurement campaign, one of the leading uncertainties was on the probe-induced AC Stark shift. This was found to be due to the power servo electronics not being set up appropriately to work with particularly low voltage references, leading to an increased level of noise measured by the OOL photodiode. On the other hand, the uncertainty on the quadrupole shift was significantly lower than the previous year, reaching 2.5×10^{-18}.

Systematic effect	$\Delta\nu/\nu_0 \times 10^{-18}$	$\sigma/\nu_0 \times 10^{-18}$
Electric quadrupole	28.0	2.5
AC Stark from 467-nm beam	0	2.4
Phase chirp of blue AOMs	0	2.2
Black-body radiation	−66.7	1.2
Collisions with background gas	0	0.6
Second-order Zeeman (DC)	−29.1	0.6
Second-order Doppler	−1.2	0.4
AC Stark from 467-nm power overshoot	0	0.1
Servo offset	0	0.1
Trapping RF Stark	−0.28	0.09
Second-order Zeeman (AC)	−0.04	0.04
AC Stark from leakage light	< 0.01	< 0.01
Trap-drive-induced AC Zeeman	N/A	N/A
Total	**−69.2**	**4.4**

Table 6.4: Uncertainty budget of the E3 clock transition frequency of $^{171}\text{Yb}^+$ during the 2020 measurement campaign (excluding the gravitational redshift). Note that the trap-drive-induced AC Zeeman shift has not yet been evaluated, but is expected to be consistent with zero within the uncertainty.

6.3.2 Absolute frequency results

With the framework described in section 5.2, the absolute frequency of the E3 transition measured over the period MJD 58914 - 58924 was calculated, with the individual ratio contributions listed in Table 6.5. The largest uncertainty contribution arises from the deviation of UTC(NPL) from TAI. It is evident from Eq. (5.14) that this uncertainty is inversely proportional to the measurement period, which was 10 days for this measurement.

Due to the aforementioned undetected signal dropouts in the clock frequency measurement, the ratio $f_{\text{Yb}^+;\Delta t_1}/f_{\text{UTC(NPL)};\Delta t_1}$ and its associated uncertainty must be considered invalid. Had these dropouts been detected, the data would have been filtered out, and the uptime Δt_1 would have been reduced. This means that any quantity that relies on the uptime based on the validity of the data must also be invalidated. This includes the statistical uncertainty of $^{171}\text{Yb}^+$, which depends on the averaging time Δt_1, the maser noise whose

Ratio	**Contribution**	$\mathbf{r_0}$	$\left(\frac{\mathbf{r}}{\mathbf{r_0}} - \mathbf{1}\right) \times \mathbf{10^{18}}$	$\mathbf{u}\left(\frac{\mathbf{r}}{\mathbf{r_0}} - \mathbf{1}\right) \times \mathbf{10^{18}}$
$\frac{f_{\mathrm{Yb^+};\Delta t_1}}{f_{\mathrm{UTC(NPL)};\Delta t_1}}$*	Ratio at comb	642 121 496 772 645.0	-252	100
	^{171}Yb$^+$ statistics		–	6
	^{171}Yb$^+$ systematics		1036	4
	Gravitational redshift		-1187	2
$\frac{f_{\mathrm{UTC(NPL)};\Delta t_1}}{f_{\mathrm{UTC(NPL)};\Delta t_2}}$*	Maser noise	1	–	245
	Maser drift		20	76
$\frac{f_{\mathrm{UTC(NPL)};\Delta t_2}}{f_{\mathrm{TAI};\Delta t_2}}$	UTC(NPL) to TAI	1	1042	526
$\frac{f_{\mathrm{TAI};\Delta t_2}}{f_{\mathrm{TAI};\Delta t_3}}$	EAL extrapolation	1	–	42
$\frac{f_{\mathrm{TAI};\Delta t_3}}{f_{\mathrm{SI};\Delta t_3}}$	TAI to SI second	1	490	120
$\frac{f_{\mathrm{Yb^+}}}{f_{\mathrm{SI}}}$	Total	642 121 496 772 645.0	1149	607

Table 6.5: Values and uncertainties associated to each ratio that contributes to the absolute frequency calculation of the E3 transition of ^{171}Yb$^+$ over the period MJD 58914 - 58924 (March 2020) according to Eq. (5.2). *The results associated to the first two ratios are invalidated due to undetected dropouts, and hence the final result is also invalidated.

uncertainty relies on the validity array used to mask the data, and the offset and uncertainty from the maser drift extrapolation, since its calculation is based on the difference between the maser drift during the whole measurement period Δt_2 and the uptime Δt_1. The remaining ratios are independent of the effect of the dropouts as they do not rely on locally measured optical data, thus their values reported in Table 6.5 are reliable.

6.4 2022 campaign

In March 2022, the largest ever optical clock comparison campaign took place between 11 optical clocks in 7 different countries. The participating laboratories were NPL, PTB, SYRTE, INRIM, UMK, VTT and NMIJ, as shown in Fig. 6.4. While the optical fibre-link network was expanded to also include INRIM, the fibre link connecting NPL to the rest of the laboratories was not operational during this campaign. However, given the participation of several other laboratories outside of the fibre-link network, satellite links

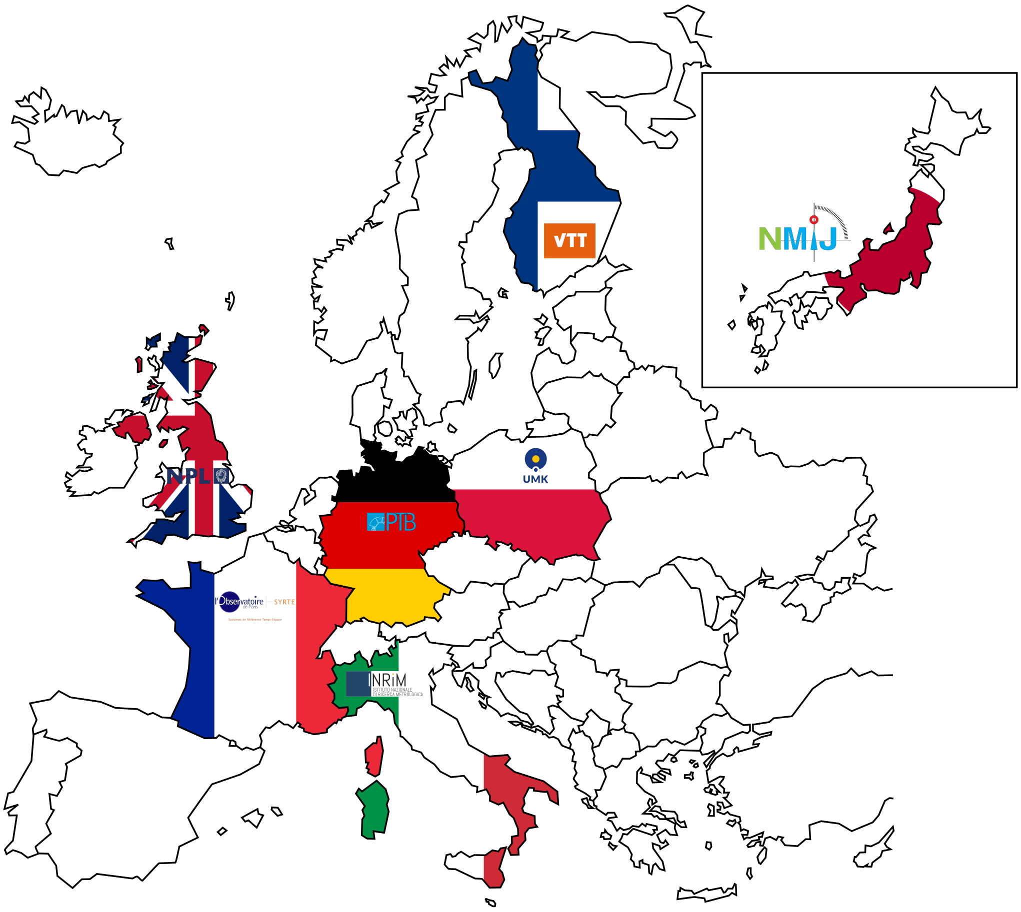

Figure 6.4: Map of the optical clock laboratories that participated in the 2022 measurement campaign: NPL in the United Kingdom, PTB in Germany, SYRTE in France, INRIM in Italy, VTT in Finland, UMK in Poland and NMIJ in Japan.

were also used for frequency transfer with the integer precise point positioning (IPPP) technique [180]. Because satellite links require longer averaging times to reach good levels of stability, the campaign was carried out for a whole month, planned to align with the majority of the TAI monthly reporting period MJD 59634-59669.

This was the first campaign in which the ARTIQ control system and database interface was used, enabling a higher level of automation of the experiment, and the possibility to monitor and send alerts upon several failure modes (as explained in chapter 3). For this campaign, the entire automatic systematic shift analysis was modified to be compatible for both the old data in text-file format and the new database data format.

Compared to the past two campaigns, several more objectives were achieved. The following subsections will outline each one of them, with the exception of the satellite link frequency comparison results, whose analysis is still in progress at the time of writing. First of all, an uncertainty budget was successfully produced with the automatic systematic shift analysis software. Secondly, a local frequency ratio between the ^{171}Yb^{+} E3 and the ^{87}Sr clock was measured. Thirdly, the absolute frequency of the E3 was measured both via TAI and compared to the local Cs fountain. Furthermore, a prototype time scale was steered for the first time at NPL by optical clocks. Finally, soon after the end of the campaign, an interleaved measurement of the E3 and E2 transitions was carried out.

6.4.1 Uncertainty budget

The uncertainty budget for this campaign is presented in Table 6.6. The reason why the BBR shift and second-order DC Zeeman shift are set to zero is because the dynamic corrections were chosen to be applied directly to the second-by-second clock frequency data in post-processing. For the BBR, this choice is motivated by the fact that this shift is evaluated as a result of a temperature measurement running continuously throughout the clock measurement period.

On the other hand, while the second-order DC Zeeman shift is usually constant throughout a campaign, and therefore an average shift would be appropriate, in the middle of the campaign it was discovered that an improper choice of the pre-probe-delay stage duration was causing the ion to experience a different magnetic field than what was requested. At the start of this stage, the large additional y-field used for cooling is turned off. However, if the delay is too short, there is not enough time for the eddy currents to dissipate before the start of the clock probe, thus skewing the direction and magnitude of the magnetic field experienced during the probe.

Systematic effect	$\Delta\nu/\nu_0 \times 10^{-18}$	$\sigma/\nu_0 \times 10^{-18}$
Electric quadrupole	22.2	2.8
Black-body radiation	0	1.2
Collisions with background gas	0	0.6
Second-order Zeeman (DC)	0	0.6
Second-order Doppler	-1.2	0.5
AC Stark from 467-nm beam	0	0.3
AC Stark from 467-nm power overshoot	0	0.1
Servo offset	0	0.1
Trapping RF Stark	-0.28	0.09
Second-order Zeeman (AC)	-0.07	0.04
AC Stark from leakage light	< 0.01	< 0.01
Phase chirp of blue AOMs	N/A	N/A
Trap-drive-induced AC Zeeman	N/A	N/A
Total	**20.6**	**3.2**

Table 6.6: Uncertainty budget of the E3 clock transition frequency of $^{171}\mathrm{Yb}^+$ during the 2022 measurement campaign (excluding the gravitational redshift). Note that the trap-drive-induced AC Zeeman shift and the blue AOM chirp shift have not yet been evaluated, but are expected to be consistent with zero within the uncertainty.

The actual magnetic field experienced by the ion was determined in post-processing, and if the resulting second-order DC Zeeman shift were to be calculated as an average throughout the whole campaign, in the middle of which the pre-probe delay was increased from 15 ms to 25 ms, its fractional uncertainty would be 2.4×10^{-18} due to the large standard deviation. By instead applying the corrections dynamically to the clock frequency in post-processing based on each measurement of $\mathbf{B}_y$ and the subsequent E3 lock(s) throughout the campaign period, the uncertainty on the shift is significantly reduced.

The dominating uncertainty is the electric quadrupole shift, which is fractionally 2.8×10^{-18}. This uncertainty is slightly higher compared to the 2020 result, even though the same configuration of electrode voltages creating the electric field gradient was maintained. Because the pre-campaign quadrupole shift was measured in the scenario with the insufficiently long pre-probe delay, its result was discarded, and only the post-campaign result was used. If the two measurements were averaged, the uncertainty would have been a factor of $\sqrt{2}$ lower. To justify the assumption that the post-campaign quadrupole shift would have been the same as the pre-campaign shift, a second post-campaign measurement was performed with the same pre-probe delay as the pre-campaign measurement, and it was verified that the two results agreed within their uncertainties.

Finally, the reason why the phase noise shift was not evaluated in this campaign is because it was expected for it to be cancelled out in real time with the PLS set up that is in place. However, while debugging the experiment for an unrelated issue, it was thought that the PLS was causing problems to the lock and it was therefore disengaged for the duration of the campaign. It is planned for this shift to be evaluated in the near future. Historically, this shift has been measured on the E3 to be at the low 10^{-18} level for typical clock AOM operating powers, while it is known to be negligible for the E2 given the extremely low AOM power required to probe the transition.

6.4.2 Local optical frequency ratio results

The ratio between the $^{171}\mathrm{Yb}^{+}$ E3 and $^{87}\mathrm{Sr}$ optical clocks at NPL was directly measured during this campaign. Fig. 6.5 shows the offset of the ratio from r_0 over the combined uptime of the two clocks. The measurement was divided into two periods, with the boundary at MJD 59659. In the middle of the campaign, it was discovered that the polarisation of the 467-nm beam used to probe the E3 was significantly unoptimised, meaning that higher optical powers were required to achieve a reasonable level of excitation. The largest gap in the data is indicative of the period in which this issue was being investigated. On MJD 59656, the polarisation of the beam was optimised, and up until MJD 59659 the same high powers were used (corresponding to 3 V and 1 V references for the high-power and low-power servos respectively). After MJD 59659, the two voltage references were reduced to 0.6 V and 0.2 V so as to not power-broaden the transition. Because two sets of power levels were used throughout the campaign, it was decided to split the measurement such that the two periods could be analysed separately.

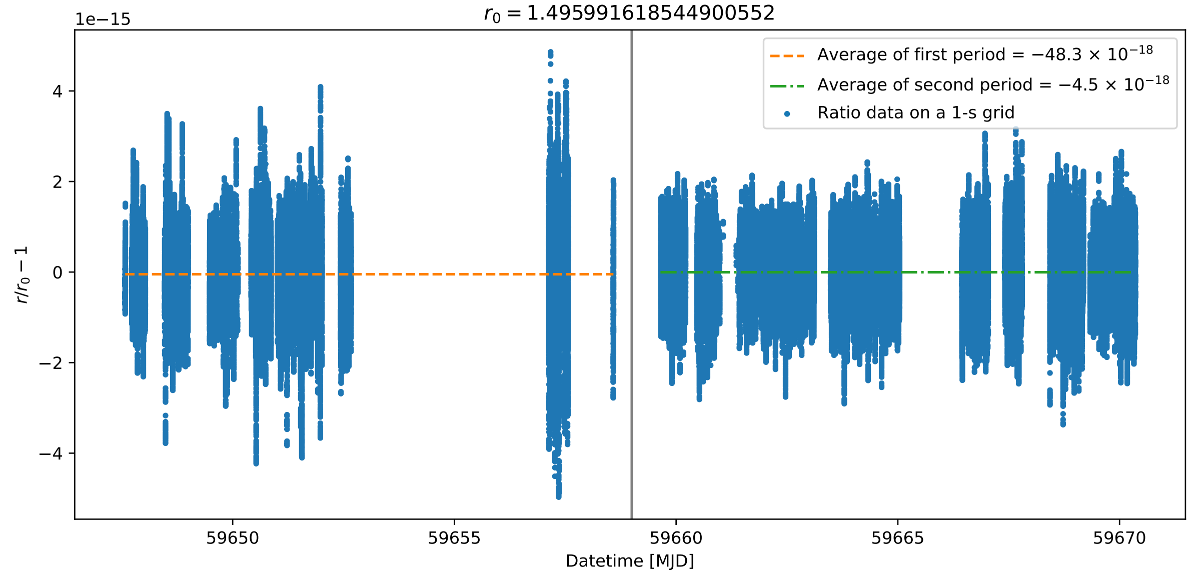

Figure 6.5: Offset from r_0 of the ratio between the ^{171}Yb$^+$ E3 and ^{87}Sr optical clocks at NPL during the 2022 campaign.

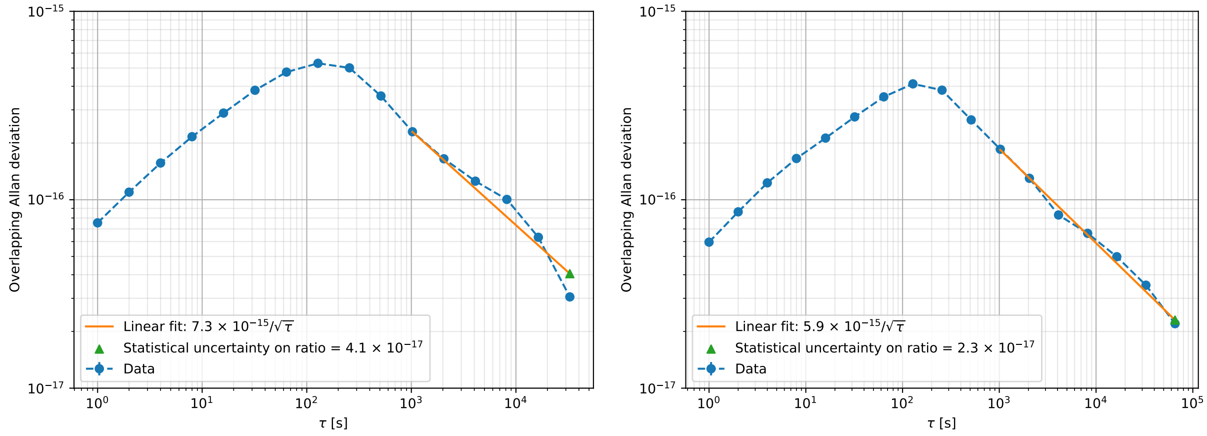

(a) First period.

(b) Second period.

Figure 6.6: Overlapping Allan deviations of the ^{171}Yb$^+$ E3 to ^{87}Sr ratio for the two periods of the 2022 campaign. The statistical uncertainty on the ratio for each period is taken as the last point of the fit to the Allan deviation.

The overlapping Allan deviations for the two periods are shown in Fig. 6.6. The Allan deviations and their fits were produced in the same way as for the 2019 ratio, as explained in section 6.2.2. Just like before, the last point of the fit is then considered to be the statistical uncertainty on the ratio. The fractional stability is seen to have improved in the second period after optimising the polarisation of the 467-nm beam, however $5.9 \times 10^{-15}/\sqrt{\tau}$ is still significantly higher than what has been achieved in the past. The high instability in the ratio, which is dominated by the $^{171}\mathrm{Yb}^{+}$ clock, is thought to be due to probing the E3 with 650-ms pulses which were too long for the achievable π-pulse at the requested beam powers, meaning that effectively there was a larger portion of deadtime in the clock cycle. If the beam powers had been even lower, then 650-ms pulses could have been more appropriate.

The $^{171}\mathrm{Yb}^{+}$ E3 to $^{87}\mathrm{Sr}$ ratio is calculated as a weighted average between the ratios measured in the two periods, leading to $r = 1.495\,991\,618\,544\,900\,529(44)$. The individual uncertainty contributions on the ratio are reported in Table 6.7. This result is shown to be consistent with the past two measurements of this ratio at NPL from the 2018 and the 2019 campaign (see Fig 6.7). From these three measurements, a weighted linear fit can be performed in order to estimate the temporal drift of the fine structure constant:

$$\frac{\dot{\alpha}}{\alpha} = \frac{1}{K_{\mathrm{E3}} - K_{\mathrm{Sr}}} \frac{\dot{r}}{r} , \tag{6.1}$$

resulting in a drift of $(-0.3 \pm 1.9) \times 10^{-18}$ year^{-1}. This is in good agreement with the best available estimate of the drift by Lange *et al.* [102] of $(1.0 \pm 1.1) \times 10^{-18}$ year^{-1}.

Uncertainty contribution	$\sigma/r_0 \times 10^{-17}$
Statistical	2.00
Yb^{+} E3 systematics	0.32
Sr systematics	2.15
Local height difference	0.12
Total	**2.96**

Table 6.7: Statistical and systematic fractional uncertainty contributions to the NPL $^{171}\mathrm{Yb}^{+}$ E3 to $^{87}\mathrm{Sr}$ ratio measured in March 2022, where $r_0 = 1.495\,991\,618\,544\,900\,552$.

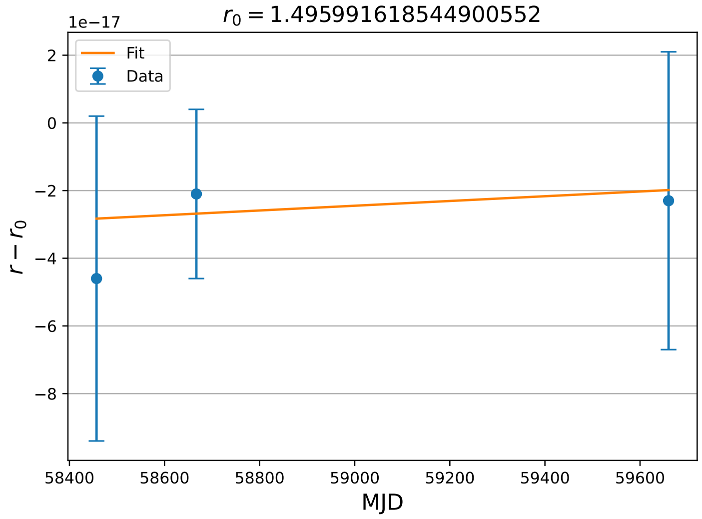

Figure 6.7: ^{171}Yb^{+} E3 to ^{87}Sr ratio throughout the years over three separate measurement campaigns.

6.4.3 Optical time scale steering

While the local time scales contributing to TAI can often be steered by either caesium primary standards or rubidium secondary standards, during this campaign it was demonstrated for the first time at NPL that a prototype time scale could be successfully steered by optical clocks. This was done by providing hourly corrections based on a weighted average of the ^{171}Yb^{+} and ^{87}Sr optical clock contributions.

While the local time scale UTC(NPL) is created by a maser with an offset generator that is steered by a local Cs fountain to minimise the offset with TAI, the signal from a second maser was used as the basis of the prototype timescale UTCx(NPL) steered by the optical clocks. The frequency comb and all the relevant frequency counters and synthesizers were clocked by the 10 MHz unsteered signal produced by the second maser.

Fig. 6.8 shows the hourly comparison between the two time scales. For the majority of the measurement period, the daily offset between UTCx(NPL) and UTCr is smaller than 0.5 ns, demonstrating how well the optically steered time scale followed UTCr over

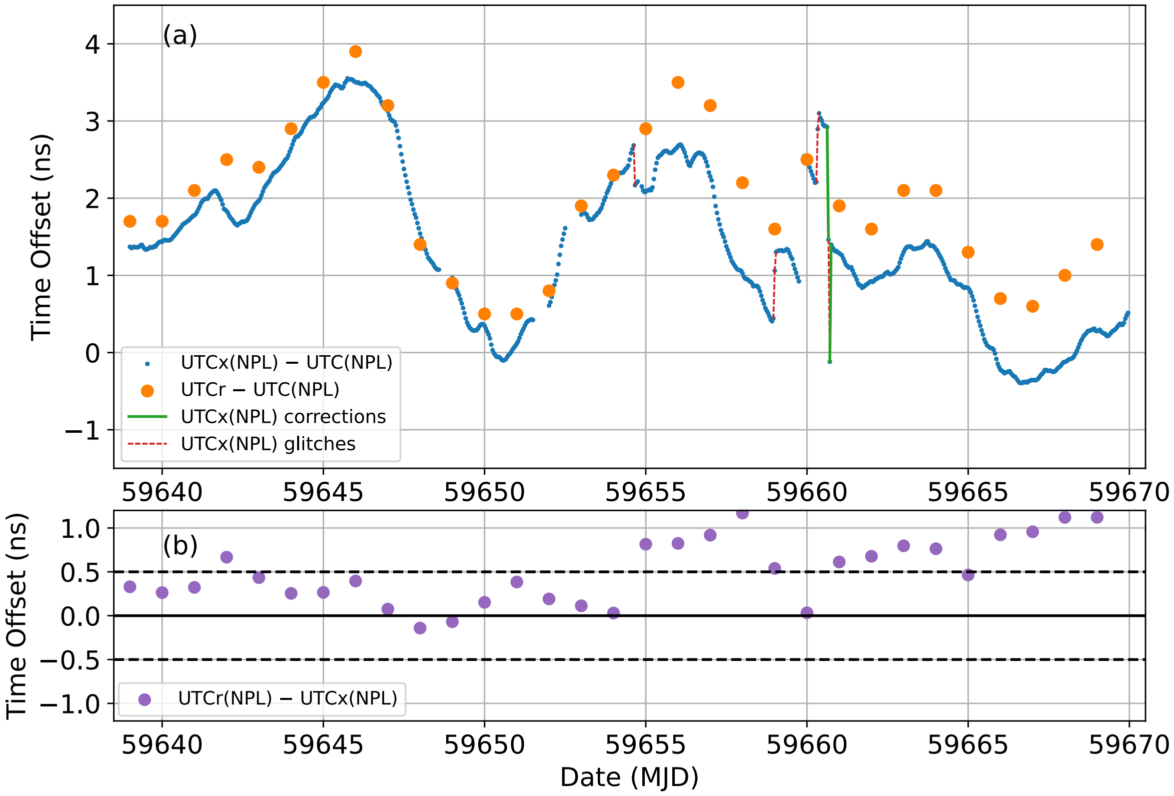

Figure 6.8: Optical time scale steering results showing the comparison between the hourly UTCx(NPL)−UTC(NPL) offset and the daily UTCr−UTC(NPL) offset. It is shown that for the majority of the measurement duration, UTCr and the optically steered UTCx(NPL) differ by less than 0.5 ns.

time. This is an extremely promising result which will pave the way towards the future in which time scales will be regularly steered by optical frequency standards.

6.4.4 On-the-fly clock uptime generation

In order to provide hourly corrections to steer the prototype time scale, the clock uptime validation was set up to run hourly, such that the clock frequency results could be generated on the fly. This also required all the systematic corrections to be applied on the fly. Because all systematic effects other than the probe-induced AC Stark shift are known in principle not to vary significantly over time, it was decided to apply a static correction to the hourly clock frequency results. Thanks to the automated systematics analysis framework in place, it was possible to generate a traceable preliminary uncertainty budget in time for the beginning of the campaign, as shown in Fig. 6.9. This involved using the pre-campaign measurement of the quadrupole shift, and using results from a series of micromotion and magnetic field measurements performed in the week leading up to the campaign start.

Because the system was not yet set up to provide on-the-fly residual probe-induced AC Stark corrections, care was taken to minimise this shift. As explained in section 4.4, this was achieved by acquiring a more accurate estimate of the true power ratio by either performing a 5-minute measurement prior to each E3 lock, or calculating the effective power ratio from the preceding E3 lock. In this way, the extrapolated frequency would require much smaller corrections in post-processing. The total uncertainty of all the corrections applied on the fly met the target level of being $< 10^{-16}$ throughout the campaign.

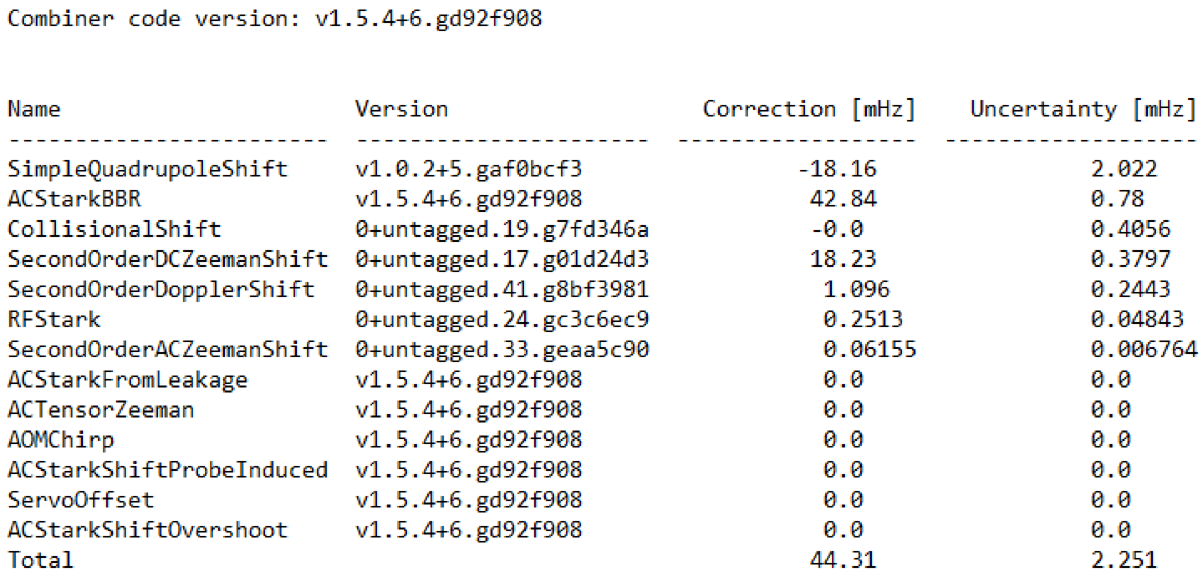

```
Combiner code version: v1.5.4+6.gd92f908


Name                      Version                   Correction [mHz]    Uncertainty [mHz]
------------------------  ----------------------  ------------------  -------------------
SimpleQuadrupoleShift     v1.0.2+5.gaf0bcf3                -18.16                2.022
ACStarkBBR                v1.5.4+6.gd92f908                 42.84                0.78
CollisionalShift          0+untagged.19.g7fd346a            -0.0                 0.4056
SecondOrderDCZeemanShift  0+untagged.17.g01d24d3            18.23                0.3797
SecondOrderDopplerShift   0+untagged.41.g8bf3981             1.096               0.2443
RFStark                   0+untagged.24.gc3c6ec9             0.2513              0.04843
SecondOrderACZeemanShift  0+untagged.33.geaa5c90             0.06155             0.006764
ACStarkFromLeakage        v1.5.4+6.gd92f908                  0.0                 0.0
ACTensorZeeman            v1.5.4+6.gd92f908                  0.0                 0.0
AOMChirp                  v1.5.4+6.gd92f908                  0.0                 0.0
ACStarkShiftProbeInduced  v1.5.4+6.gd92f908                  0.0                 0.0
ServoOffset               v1.5.4+6.gd92f908                  0.0                 0.0
ACStarkShiftOvershoot     v1.5.4+6.gd92f908                  0.0                 0.0
Total                                                       44.31                2.251
```

Figure 6.9: Copy of the terminal output of the software that evaluates all the systematic shifts and uncertainties with the respective code version tags. Shifts reported as 0 ± 0 mHz were not evaluated for the on-the-fly corrections; however, they are all expected to be significantly below the 10^{-16} level.

Even though the hourly clock frequency results were accurate enough to be used for the optical steering of the time scale, a second more finalised uncertainty budget was produced after the end of the campaign. These are the results described in section 6.4.1. In the future, instead of assuming an approximate static correction throughout a campaign measurement period, with only the AC Stark shift being compensated in real time, experimental routines will be implemented to correct most systematic shifts in real time.

6.4.5 Absolute frequency results

The uptime of the $^{171}\mathrm{Yb}^{+}$ optical clock during this campaign spans the period Δt_1 = MJD 59647.576076 - 59670.347211. The absolute frequency of the E3 transition was measured over the period Δt_2 = MJD 59649 - 59669 within the 1-month TAI computation period Δt_3 = MJD 59634 - 59669, as shown in Fig. 6.10. The overlap of Δt_1 and Δt_2 resulted in 43 % uptime. Because in this campaign the optical clock was measured against a different maser than the one that generates UTC(NPL), an additional step needed to be included in the analysis chain to link the two maser frequencies f_{maser} and $f_{\mathrm{UTC(NPL)}}$, which was enabled by the availability of phase-comparator data throughout the measurement period.

The evaluation of the stochastic and deterministic downtime corrections was done based on the unsteered-maser data. It is important to note that both the unsteered maser and the steered maser generating UTC(NPL) are different from the maser used in the previous two measurement campaigns, meaning that their noise parameters are slightly different. It was also found that both these new masers are more strongly affected by diurnal temperature fluctuations, which become apparent in an Allan deviation at long timescales. While this source of noise can be approximately modelled by a sinusoid, its contribution to the noise model would need to be determined by a series of Monte-Carlo simulations with random phases. Because this methodology is incompatible with the current analysis of the stochastic downtime uncertainty in the frequency domain (see section 5.2.2), a very conservative approach is taken by increasing the flicker floor level to

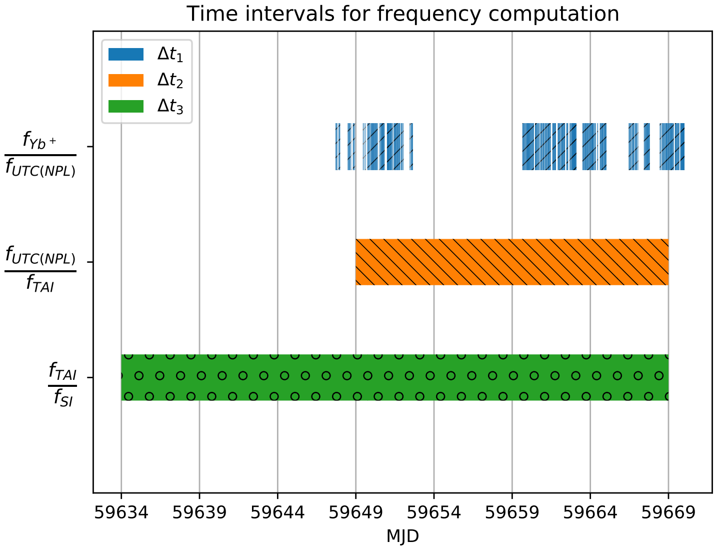

Figure 6.10: Time intervals for the computation of the corresponding frequency ratios. Δt_1 is the uptime of the ^{171}Yb$^+$ clock during the March 2022 measurement campaign, and is made up of a series of discontinuous time intervals. Δt_2 is made up of four 5-day TAI reporting periods (MJD 59649 - 59669), while Δt_3 covers the 1-month TAI computation period (MJD 59634 - 59669).

account for the bump in the Allan deviation introduced by the diurnal noise.

The linear drift of the maser during the measurement period is shown in Fig. 6.11, and because of the large number of data points available, the uncertainty on the resulting deterministic downtime correction is relatively low at 9.7×10^{-17}. On the other hand, the stochastic downtime uncertainty of 9.0×10^{-16} is the dominant contribution to the uncertainty on the absolute frequency, due to the conservative approach taken to estimate it. In the Allan deviation shown in Fig. 6.12, the effect of the diurnal fluctuations is not immediately apparent; however, this is due to the fact that the longest continuous period of optical clock data used to generate the plot was not long enough to include the effect of the diurnals. Results from the continuous measurement of the local caesium fountain against the maser over a whole month helped in choosing an upper bound of 2.5×10^{-15} for the flicker floor to account for this effect.

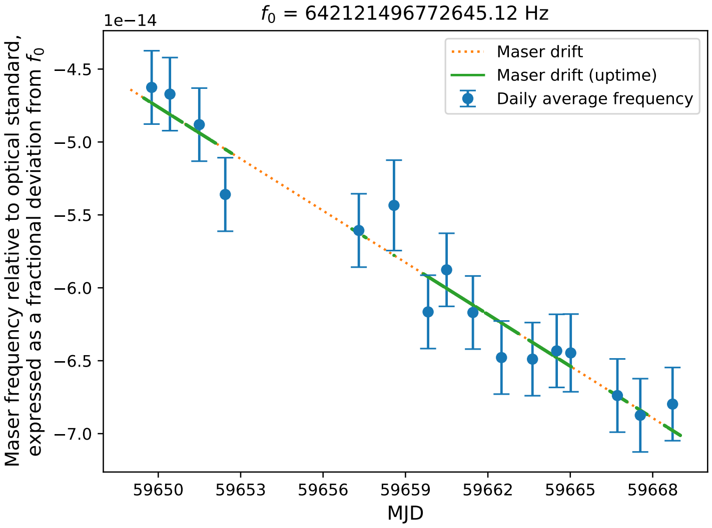

Figure 6.11: Frequency of the unsteered maser measured in March 2022 relative to ^{171}Yb$^+$ offset from the BIPM reference frequency f_0. The blue points represent the daily average of the frequency, fitted by the dotted orange line. The green segments indicate the uptime of the measurement.

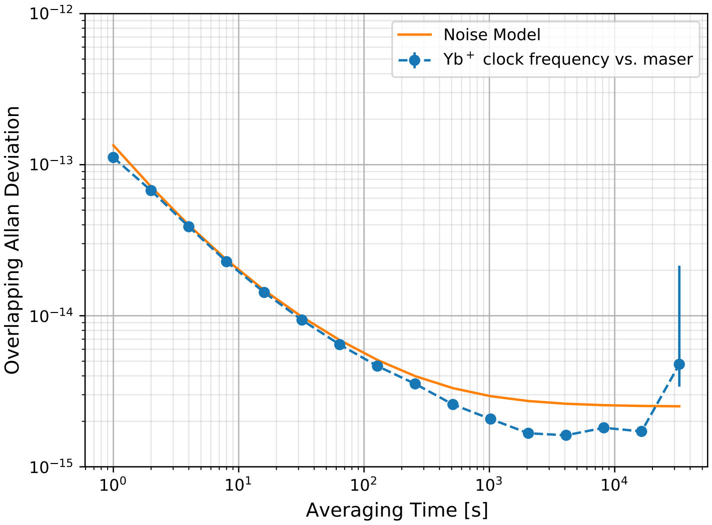

Figure 6.12: Noise model of the unsteered hydrogen maser used in the 2022 absolute frequency measurement, based on a combination of white phase noise, white frequency noise and flicker frequency noise. The latter was inflated to account for the effect of diurnal fluctuations at longer timescales.

The absolute frequency of the E3 is calculated to be 642 121 496 772 645.45(62) Hz, which is in good agreement with the 2021 BIPM recommended frequency of 642 121 496 772 645.12(12) Hz. The individual ratio contributions are displayed in Table 6.8. Note that because the measurement duration overlaps with four 5-day TAI periods, the uncertainty arising from the link between UTC(NPL) and TAI is significantly lower than for the previous two campaigns, in which it was the dominating uncertainty due to the shorter duration of the measurements. It is worth nothing that this result is also in good agreement with the absolute frequency measured relative to the local caesium fountain, which is equal to 642 121 496 772 645.11(56) Hz.

Ratio	**Contribution**	$\mathbf{r_0}$	$\left(\frac{\mathbf{r}}{\mathbf{r_0}}-\mathbf{1}\right)\times\mathbf{10^{18}}$	$\mathbf{u}\left(\frac{\mathbf{r}}{\mathbf{r_0}}-\mathbf{1}\right)\times\mathbf{10^{18}}$
$\frac{f_{\mathrm{Yb^+};\Delta t_1}}{f_{\mathrm{maser};\Delta t_1}}$	Ratio at comb	642 121 496 772 645.12	59328	100
	^{171}Yb$^+$ statistical		–	8
	^{171}Yb$^+$ systematics		71	3
	Gravitational redshift		−1187	2
$\frac{f_{\mathrm{maser};\Delta t_1}}{f_{\mathrm{maser};\Delta t_2}}$	Maser noise	1	–	897
	Maser drift		−1097	97
$\frac{f_{\mathrm{maser};\Delta t_2}}{f_{\mathrm{UTC(NPL)};\Delta t_2}}$	Maser to UTC(NPL)		−56654	44
$\frac{f_{\mathrm{UTC(NPL)};\Delta t_2}}{f_{\mathrm{TAI};\Delta t_2}}$	UTC(NPL) to TAI	1	−116	282
$\frac{f_{\mathrm{TAI};\Delta t_2}}{f_{\mathrm{TAI};\Delta t_3}}$	EAL extrapolation	1	–	25
$\frac{f_{\mathrm{TAI};\Delta t_3}}{f_{\mathrm{SI};\Delta t_3}}$	TAI to SI second	1	160	120
$\frac{f_{\mathrm{Yb^+}}}{f_{\mathrm{SI}}}$	Total	642 121 496 772 645.12	506	959

Table 6.8: Values and uncertainties associated to each ratio that contributes to the absolute frequency calculation of the E3 transition of ^{171}Yb$^+$ over the period MJD 59649 - 59669 (March 2022) according to Eq. (5.2). r_0 is equal to the recommended value of the frequency of the E3 approved by the CIPM in 2021.

6.4.6 E3/E2 ratio measurement

After the end of the one-month measurement campaign period, a new experimental routine was designed and implemented in ARTIQ for the interleaved measurement of the E3/E2 ratio. The servo sequence is designed similarly to what was shown in Fig. 2.15 with the additional inclusion of an E2 probe in the middle of each pair of high- and low-power E3 probes. Moreover, because the quadrupole shift experienced by the E2 is significantly larger, the E2 was probed in three orthogonal magnetic fields alternating every 30 minutes, as shown in Fig. 6.13, such that the shift can average out to zero [40]. Note that because the first 5 minutes of each 30-minute dataset must be discarded to ignore the effect of the servo pulling into the new frequency level, only 5/6 of the data is valid. On the other hand, the E3 was still probed in $\mathbf{B}_y$ using the second set of coil current supplies such that the same value for the quadrupole shift during the recent campaign could be used.

The uncertainty budget for the two clock transitions is shown in Table 6.9. The dominating uncertainty is still for the quadrupole shift in both transitions. Because this uncertainty is in most part based on statistics, the most straightforward way to reducing it would be to perform a longer measurement. However, it is worth noting that the instability of the ratio itself decreases more slowly over time than the uncertainty on the quadrupole

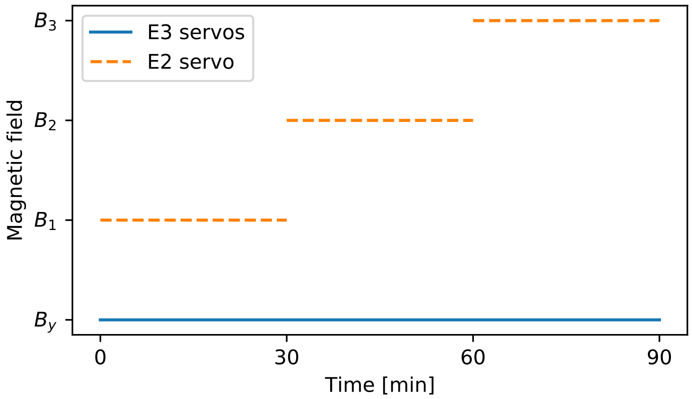

Figure 6.13: Time series of the interleaved E2 and E3 servos.

Systematic effect	$\frac{\Delta\nu_{\mathbf{E3}}}{\nu_{\mathbf{E3}}} \times 10^{-18}$	$\frac{\sigma_{\mathbf{E3}}}{\nu_{\mathbf{E3}}} \times 10^{-18}$	$\frac{\Delta\nu_{\mathbf{E2}}}{\nu_{\mathbf{E2}}} \times 10^{-18}$	$\frac{\sigma_{\mathbf{E2}}}{\nu_{\mathbf{E2}}} \times 10^{-18}$
Electric quadrupole	22.2	2.8	0	118
Black-body radiation	-66.5	1.2	-480	98
Second-order Zeeman (DC)	-70.4	1.0	683	15
Second-order Zeeman (AC)	-0.03	< 0.01	1.3	1.1
Collisions with background gas	0	0.6	0	0.6
Second-order Doppler	-1.3	0.5	-1.3	0.5
AC Stark from probe beam	0	0.7	< 0.3	< 0.3
AC Stark from probe power overshoot	0	0.1	0	0
Servo offset	0	0.1	0	< 0.1
Trapping RF Stark	-0.32	0.10	-2.0	0.6
AC Stark from leakage light	< 0.01	< 0.01	< 0.1	< 0.1
Phase chirp of blue AOMs	N/A	N/A	N/A	N/A
Trap-induced AC Zeeman	N/A	N/A	N/A	N/A
Total	**-116.4**	**3.4**	**198**	**154**

Table 6.9: Uncertainty budget from the interleaved E3/E2 ratio measurement for each of the two optical clock transitions (excluding the gravitational redshift).

shift. The second largest contribution to the uncertainty budget comes from the BBR, whose large uncertainty on the shift experienced by the E2 transition arises from the large uncertainty on the differential polarisability of the E2 given by Ref. [23].

The probe-induced AC Stark shift is extrapolated to zero for the E3. However, due to the lack of a power-servo set up in the 436-nm beam, the shift needs to be evaluated for the E2. The estimated[15] 436-nm probe power and the 467-nm power at 1 V reference, together with the differential polarisabilities $\Delta\alpha_{\mathrm{E2}} = 6.90 \pm 1.40 \times 10^{-40}\ \mathrm{Jm^2/V^2}$ [23] and $\Delta\alpha_{\mathrm{E3}} = 0.888 \pm 0.016 \times 10^{-40}\ \mathrm{Jm^2/V^2}$ [19], are used to scale the average AC Stark shift experienced by the E3 at 1 V reference to the E2.

The resulting E3/E2 ratio is calculated to be $0.932\,829\,404\,530\,965\,499(151)$, where the uncertainty is the sum in quadrature of the E3 and E2 systematic uncertainties and of the ratio's statistical uncertainty of 5×10^{-17}. For simplicity, it was assumed for this preliminary result that there is no correlation between the E3 and E2 uncertainties. The

---

[15] It is difficult to measure the optical power of the 436-nm beam accurately as it is of the order of nW.

lowest uncertainty value of this ratio was reported by Lange *et al.* [102], as a result of 11 measurements over 1500 days. However, the BBR shift in that paper is calculated using the non-peer-reviewed E2 differential polarisability from Ref. [181]. If this was used in the calculation of our ratio, the result would be 0.932 829 404 530 965 515(122), which is just over one standard deviation above the Lange *et al.* value. However, the agreement with Lange *et al.* is closer than the agreement with the last measurement of the ratio at NPL from 2014 [25], which currently appears to be a bit of an outlier at two standard deviations below the Lange *et al.* value.

6.5 Conclusion

This chapter described the key aspects of the experimental setup for three clock measurement campaigns, and the main results produced. Note that because the trap-drive-induced AC Zeeman shift has not yet been evaluated, and additionally in 2022 the phase noise shift was not measured, the uncertainty budgets presented must still be considered preliminary. However, the estimated sizes of these shifts and their uncertainties would have an almost negligible effect on the current ratio and absolute frequency results.

The results presented in this chapter have an important role in the context of international metrology. Once the uncertainty budgets have been completely finalised and published, the results for the absolute frequency of the ^{171}Yb^{+} E3, the ratio between ^{171}Yb^{+} E3 and ^{87}Sr , and the ratio between the ^{171}Yb^{+} E3 and E2 transitions will contribute to the next recalculation of the recommended values of these quantities performed by CCTF. These results represent significant progress towards the redefinition of the SI second, as they are contributing towards several of the required milestones set out by the CIPM. In particular, the measurements of the E3 relative to TAI during the 2019 and 2022 campaigns will be officially reported to the BIPM such that they can be used in the evaluation of TAI during the relevant reporting periods. Fig. 6.14 shows how the recent measurements of the absolute frequency of the E3 transition fit in with the literature.

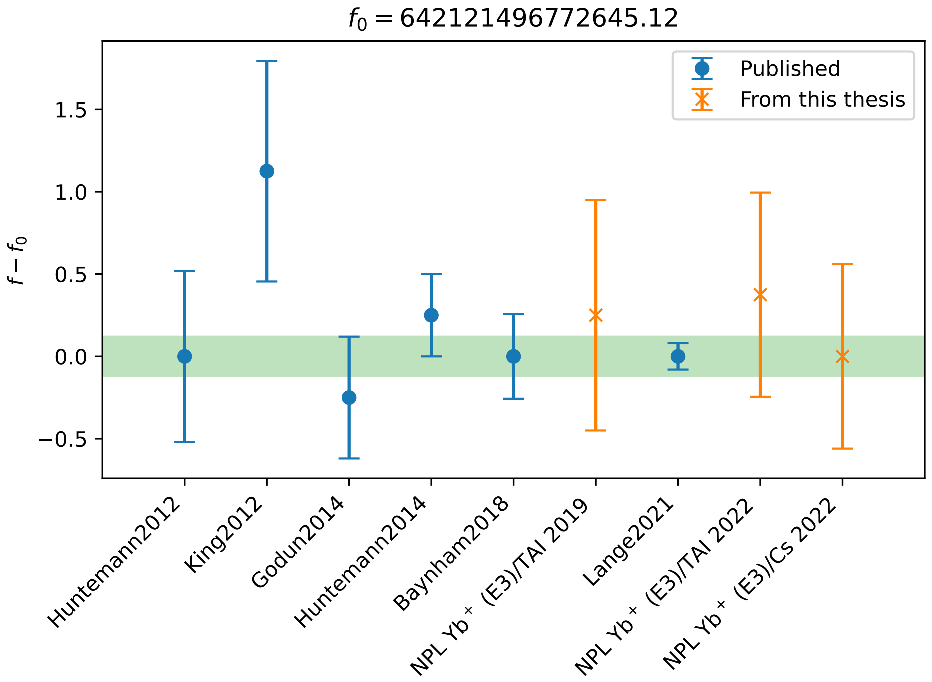

Figure 6.14: NPL measurements of the ^{171}Yb$^+$ E3 transition during the 2019 and 2022 campaigns compared to the literature [24, 25, 94, 102, 182, 183]. The green band represents the uncertainty on the recommended value f_0.

With regard to my level of participation in the three measurement campaigns, in 2019, while I was not involved on the experimental side, I made a notable contribution to the systematic shift analysis, particularly in the determination of the quadrupole shift. While the systematic uncertainty of the E3 ended up being higher than desired, the 2019 campaign still resulted in a valid frequency ratio between the local ^{171}Yb$^+$ and ^{87}Sr optical clocks, and an E3 absolute frequency via TAI, which was calculated with the automated framework that I worked on.

While all the frequency measurement results from the 2020 campaign had to be invalidated due to a technical issue, it was still possible to produce a valid uncertainty budget. Thanks to the improvements that I made to the quadrupole shift measurement and analysis method, its fractional uncertainty was reduced to 2.5×10^{-18}, setting a new baseline for what can be achieved in the future. During this campaign, my participation in operating the optical clock was more significant, and my largest overall contribution was in the development of the automatic systematics analysis framework.

Finally, the 2022 campaign measurement was particularly fruitful, as not only it produced valid absolute frequency and local ytterbium-to-strontium ratio results, but also demonstrated for the first time at NPL that a time scale could be successfully steered by optical clocks. In the preparation for the campaign, I had a major role in the experimental upgrade to ARTIQ control and in the automation of several experimental routines, together with the setup of monitors and alerts for clock failure modes. I also had an active role in the operation and maintenance of the optical clock throughout the campaign, and subsequently led the E3/E2 ratio measurement. Finally, in terms of data analysis, I worked on ensuring the compatibility of the automatic systematic shift analysis framework with the new database data format, I produced the uncertainty budget for both the E3 campaign and the E3/E2 ratio measurement, and I calculated the E3 absolute frequency via TAI.

7 Outlook and conclusion

This chapter will present some plans for future work on the ^{171}Yb^{+} optical clock experiment, and will conclude with a summary of the thesis. First, the improvements in the design of a next-generation ion trap will be described. Second, the plan for running the ^{171}Yb^{+} and ^{87}Sr systems at NPL in a hybrid clock configuration will be explained. Furthermore, the plan for the measurement of several more systematic shifts on the fly will be presented. The future goal for unattended clock operation using the "metacontroller" framework will be highlighted. Finally, the most important achievements from my PhD will be outlined.

7.1 Next-generation trap

A second ion trap (pictured in Fig. 7.1) has been developed and built for the purpose of performing direct clock-clock comparisons. While I was not involved in the general design of the ion trap, I contributed to its assembly. There are a few improvements in the design of the new trap compared to the first one. First of all, the supporting C-piece is made out of molybdenum in the new trap, as opposed to copper, as it has a lower coefficient of thermal expansion. A new RF feedthrough was designed with a larger separation between the RF and DC to reduce dielectric heating in the feedthrough which would cause a temperature rise in the electrodes. Furthermore, an additional pair of compensation electrodes was introduced for the minimisation of ion micromotion. Moreover, a baffle was designed to be positioned just after the oven in order to prevent neutral ytterbium from coating the electrodes during loading. Finally, the H, U, D beam fibres will be set up on piezo-controlled mounts which will enable the fibre alignment at the ion to be performed in a more automated way.

The new ion trap will also benefit from improved magnetic shielding. This will open up the possibility to probe the E3 on the magnetically-sensitive $m_F = \pm 2$ states, as these

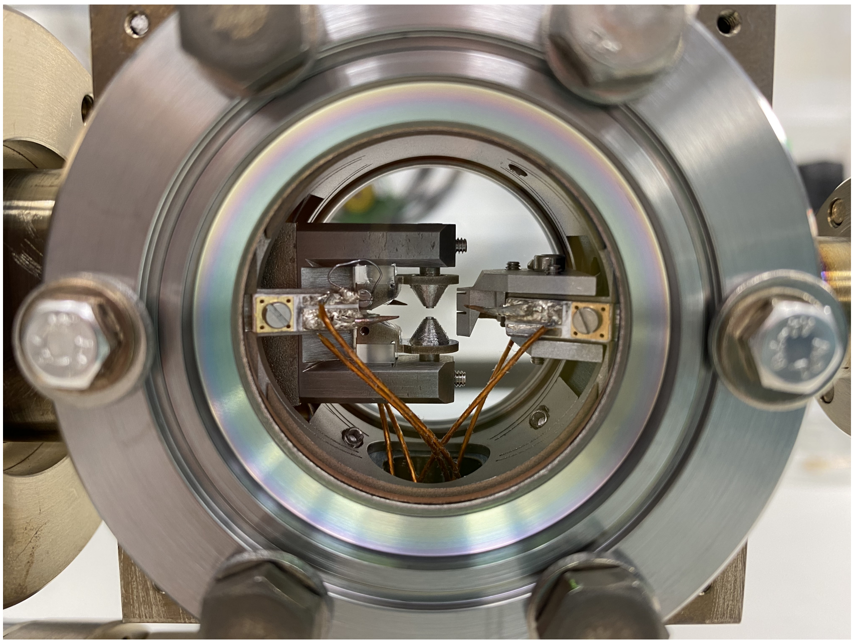

Figure 7.1: Picture of the next-generation ion trap.

transitions are free from tensor shifts. In the current trap setup, due to the lower level of magnetic shielding, these states are significantly broadened by magnetic field noise and would require a large amount of 467-nm power that is not available. With the improved magnetic shielding, it will be possible to operate the clock with zero quadrupole shift, with the additional benefit of measuring and cancelling out the Zeeman shift in real time.

A series of delays caused by faults with the bake-out station, turbo pumps and ion pumps meant that the trap, although fully assembled, could not be ready for testing and usage by the end of my PhD. Once the new ion trap is properly under vacuum and fully implemented in the system, it will be possible to make direct measurements of the frequency ratio between the two clocks and gain more confidence in their performance.

7.2 Hybrid clock operation

It is planned for the ytterbium and strontium systems at NPL to run in a hybrid clock configuration, such that the stability of the ^{87}Sr lattice clock can be used to enhance the stability of the ^{171}Yb^{+} ion clock. Two ^{87}Sr systems will be operated in a zero-deadtime mode such that phase corrections from the ^{87}Sr clocks can be continually fed to the ultrastable cavity used to stabilise all the clock lasers. In this way, the coherence time of the ^{171}Yb^{+} clock probing light can be significantly increased, allowing much longer probe times to be used.

7.3 On-the-fly systematic corrections

While in the 2022 measurement campaign it was possible to generate optical clock data on the fly thanks to the rapid uptime validation, this assumed that all systematic shifts except the AC Stark shift were static throughout the campaign and would vary significantly less than 1×10^{-16}, which was the level of precision needed for the time scale steering. However, in the future, it is planned for some of the systematic shifts to be evaluated and cancelled out in real time.

First of all, with the implementation of new faster-switching current supplies, it will be possible to cancel out the quadrupole shift in real time by alternating between the three orthogonal magnetic fields in each probe, and extrapolating the average frequency on the fly. At the moment, this is not achievable due to the slow communication time between the current supplies and the control computer. Furthermore, the second-order Zeeman shift can also be corrected in real time by probing the first-order Zeeman components of the E2 every specified number of E3 probes, such that the magnitude of the magnetic field can be monitored and the shift can be corrected on the fly. Moreover, because the BBR shift is already measured in real time at 30-s intervals and corrected in post-processing, it will be straightforward to apply the corrections on the fly. Finally, the micromotion, which is determined by the measurement of the ion's fluorescence signal in three directions, could be measured in real time by accumulating the fluorescence data from each readout stage.

7.4 Unattended clock operation

One of the most important goals for any optical clock to achieve is the ability to run unattended for a specified period of time, ideally for the full duration of a clock measurement campaign which would be typically two weeks. This would serve as a great demonstration of the robustness of the system, and as a significant timesaver for the scientists! In addition, for an optical frequency standard to be regularly contributing to TAI, it is important for its uptime to be maximised in order to reach the desirable level of uncertainty.

Many of the upgrades to the experiment and to the data analysis frameworks described throughout this thesis contributed towards this goal of full automation, and it can certainly be said that the $^{171}\mathrm{Yb}^{+}$ ion clock is now significantly more automated than three years ago. The implementation of the "metacontroller" for the automatic recovery from failure modes will represent a leap forward in the right direction.

7.5 Summary of achievements

This thesis has been focused on the progress in the $^{171}\mathrm{Yb}^{+}$ ion optical clock experiment at NPL during my PhD. It was shown that the implementation of the ARTIQ framework in the experimental setup was beneficial for a more cohesive control of the experiment and for the increased level of automation in the system, from different interleaved locking algorithms to systematic shift minimisation routines. Several monitors were set up for the detection of failure modes, and automated alerts were sent out for the issues to be resolved. A series of automated recovery algorithms was designed as part of a "metacontroller" framework, which is yet to be implemented and tested.

The analysis of almost all systematic frequency shifts was automated and unified into a framework designed to output an uncertainty budget for any given clock measurement with minimal manual input. Each analysis program is individually version-controlled, and the outputted uncertainty budget is accompanied by the code versions to provide full traceability. Furthermore, several systematic shifts also underwent an improvement and automation in their measurement. The most significant advancement lies in the measurement of the electric quadrupole shift, which can now be directly measured with an accuracy in the low parts in 10^{18}.

A framework for the automated evaluation of the absolute frequency of the optical clock via TAI was developed. This involves processing the optical frequency data measured against a H maser referenced to the local realisation of UTC, accounting for the regular frequency steers that the maser experiences, and for the fact that while the maser runs continuously, the optical clock does not achieve 100 % uptime. It is then necessary to link the local realisation of UTC back to the SI second. With this analysis now fully automated and generalised for any optical clock transition, it will become more straightforward for optical frequency standards to regularly contribute to TAI.

Throughout three clock measurement campaigns, several results were produced and milestones were achieved. In the 2019 campaign, the fractional systematic uncertainty on the E3 transition was measured to be 6.9×10^{-18}, strongly dominated by the quadrupole shift uncertainty. The local ^{171}Yb^{+} (E3) to ^{87}Sr ratio was measured with a fractional uncertainty of 1.7×10^{-17}. Finally, the absolute frequency via TAI was measured with a fractional uncertainty of 1.1×10^{-15}, whose relatively large size is due to the small amount of data and its poor overlap with the monthly TAI reporting period. In 2020, the fractional uncertainty of the ^{171}Yb^{+} (E3) systematic frequency shifts was reduced to 4.4×10^{-18} thanks to the improvements made to the quadrupole shift measurement and analysis.

Finally, the 2022 campaign, which was run entirely with the new ARTIQ control system, resulted in a fractional systematic uncertainty of 3.2×10^{-18}. The local ^{171}Yb^{+} (E3) to ^{87}Sr ratio was measured with a fractional uncertainty of 2.9×10^{-17}, and it was shown that the three latest measurements of this ratio at NPL are in very good agreement. With these data, the temporal drift of the fine structure constant was constrained with a fractional uncertainty of 1.9×10^{-18}. The absolute frequency of the E3 was measured via TAI with a fractional uncertainty of 9.6×10^{-16}, strongly dominated by the flicker noise in the H maser used in the measurement. This result was in good agreement with the absolute frequency measured relative to the local Cs fountain. The E3/E2 ratio was measured with an uncertainty of 1.5×10^{-16}, with the BBR and quadrupole shifts on the E2 as the leading uncertainties, and the result was shown to agree well with the literature. Finally, it was demonstrated for the first time at NPL that optical clocks could be used to successfully steer a time scale. In fact, a prototype time scale steered by both the ^{171}Yb^{+} and ^{87}Sr clocks at hourly intervals was within 0.5 ns from UTCr for the majority of the measurement duration of almost one month, which is better than the stability of UTC(NPL).

Appendices

A Laser setups

A.1 760-nm laser setup for repumping

The setup for the 760-nm laser system is shown in Fig. A.1. Two identical free-running diode lasers[16] are tuned to produce 760.0650-nm and 760.0750-nm light to repump the $^2\mathrm{F}_{7/2}(F=4)$ and $^2\mathrm{F}_{7/2}(F=3)$ states respectively. The wavelengths are tuned manually by varying the current; however, in the future, the two lasers will be locked to a new higher-resolution wavemeter. The two beams are combined in a fibre combiner, and then split by a 90:10 fibre splitter. The stronger beam is sent to the Beam Combiner, while the weaker beam is measured to the wavemeter.

A.2 935-nm laser setup for repumping

The diagram for the 935-nm laser system required for repumping the ion from the $^2\mathrm{D}_{3/2}$ level back into the cooling cycle is shown in Fig. A.2. A 935.19-nm ECDL[17] is locked to an external cavity (of the same design as the cavity from the 370-nm setup) via a PDH lock. While the PDH lock makes fast changes to the diode current, another slow lock is performed by the computer that adjusts the laser piezo voltage to account for the drift of the cavity. Furthermore, the computer monitors the cavity transmission and relocks the laser if it were to come unlocked. An additional piezo-controller (a second channel from the same piezo-controller used for the 370-nm system) is used for manual fine adjustment of the cavity length allowing the cavity mode to be tuned to the correct frequency for the atomic transition.

---

[16] Eagleyard LD-0760-0040-DFB-1.

[17] New Focus Vortex 6021 laser controlled by a Vortex 6000 laser controller.

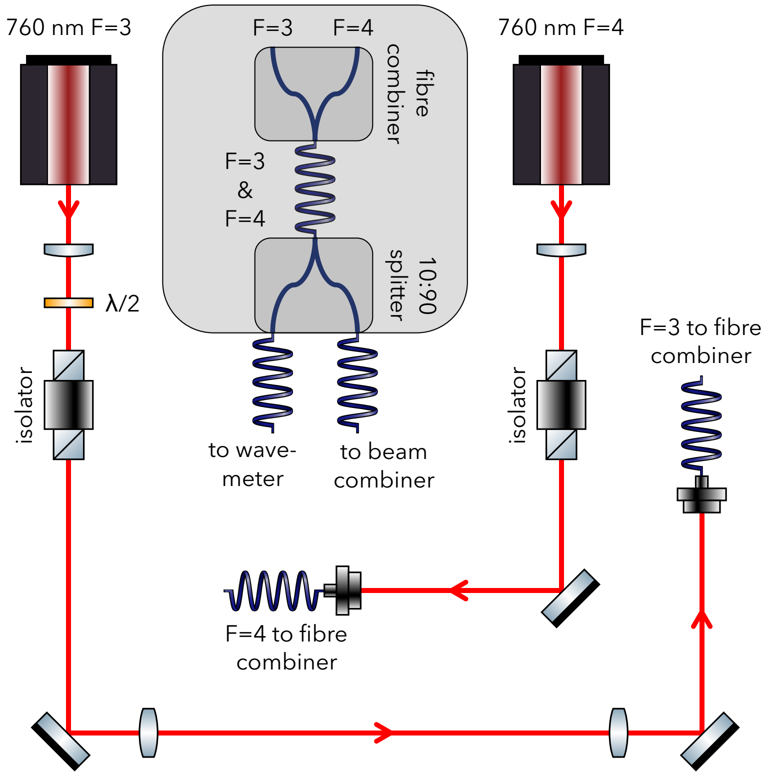

Figure A.1: Diagram of the 760-nm clock laser setup.

The 935-nm light is split into three beams. The first one is sent to the Wavelength Switcher; the second beam is used to lock to the cavity, and its transmission through the cavity is used to probe the ${}^2\mathrm{D}_{3/2}\,(F=1) \rightarrow {}^3[3/2]_{1/2}\,(F=0)$ transition, repumping the ion out of the $F=1$ state which it can populate during the cooling cycle, as shown by Fig. 2.1. Finally, the third beam passes through an EOM[18] which applies a -3.06 GHz sideband necessary to repump the ion out of the ${}^2\mathrm{D}_{3/2}\,(F=2)$ state, the upper state of the E2 transition, after a successful excitation.

---

[18] New Focus 4433.

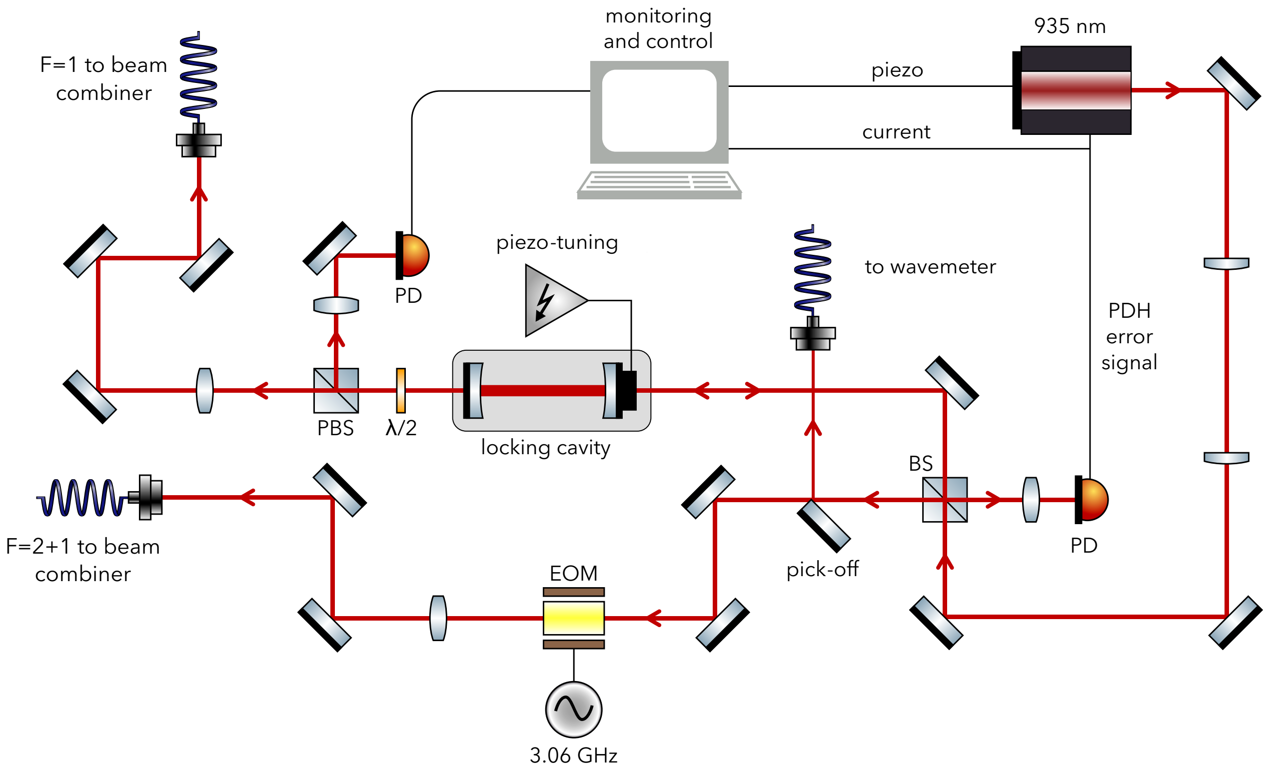

Figure A.2: Diagram of the 935-nm repump laser setup.

A.3 399-nm laser setup for photoionisation

The setup for the 399-nm system is shown in Fig. A.3. The laser is a free-running 399-nm high-power diode-laser[19]. The light is split by a 90:10 beam splitter. The stronger transmitted beam is slightly attenuated by a neutral-density filter (NDF) in order to attain the desired power of 399-nm light at the ion. This beam is then coupled into a PM fibre leading to the Beam Combiner setup. The weaker reflected 399-nm beam is coupled into a fibre that carries the light to the Wavelength Switcher.

---

[19] Toptica DL pro HP.

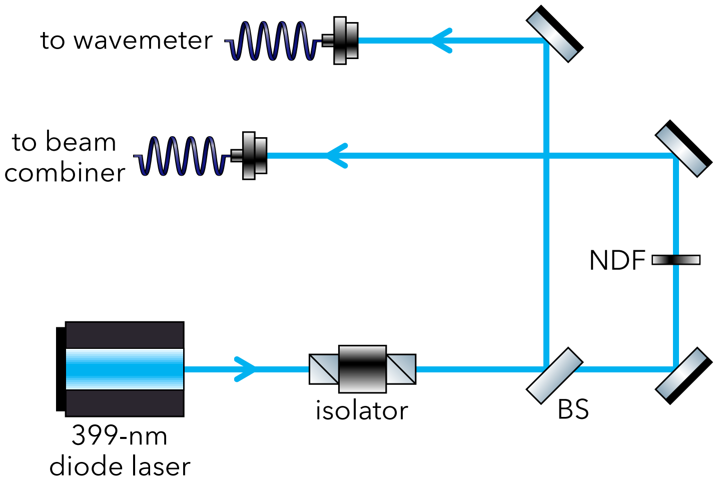

Figure A.3: Diagram of the 399-nm photoionisation laser setup.

A.4 871-nm clock laser setup

The setup for the 871-nm laser system is shown in Fig. A.4. A Toptica DL 110 pro ECDL outputs 871-nm light whose frequency is pre-stabilised via a PDH lock to a local ULE cavity kept under vacuum at a pressure of 5×10^{-7} mbar. The cavity's temperature is controlled by a home-made temperature controller (see Appendix C in Ref. [7]), and the whole laser system is enclosed in a wooden box with rubber and foam inner lining for thermal insulation. A water-cooled heat sink is inserted in the middle of the box lid, which when closed is located just above a heat sink inside the box connected to the Peltier coolers that keep the cavity at its temperature setpoint. PLS is applied to the fibre that carries the light to the frequency comb laboratory in order to cancel out any accumulated phase noise.

One beam of 871-nm light is sent to the second frequency comb in another nearby laboratory where its optical frequency is measured to double check the first comb's performance. Another beam is coupled towards the Wavelength Switcher setup for wavemeter measurements. Note that while the frequency is already measured to extreme accuracy by the frequency comb, the wavemeter is still required to help the user lock the

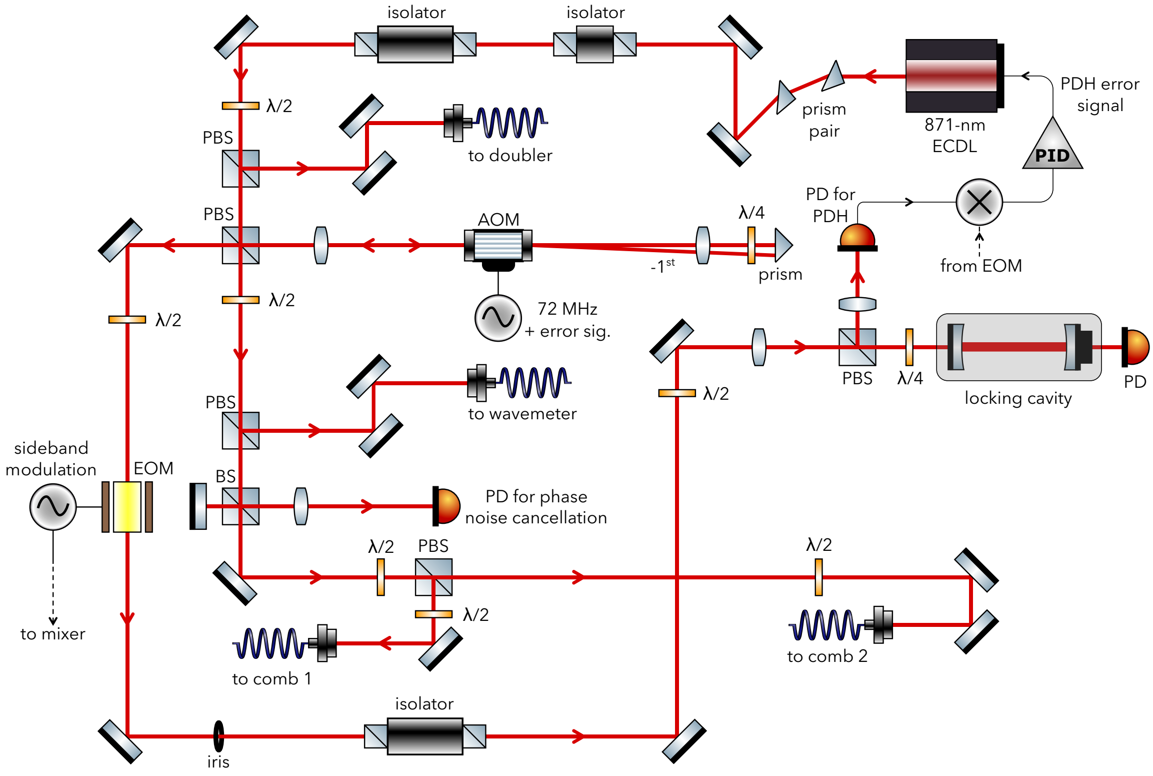

Figure A.4: Diagram of the 871-nm clock laser setup.

laser to the right cavity mode. Finally, 871-nm light is also coupled to a fibre connected to a frequency doubler.

A.5 934-nm laser setup

The setup for the 934-nm laser system is shown in Fig. A.5. The system consists in a Toptica TA Pro 940 system that outputs 934-nm light amplified by a tapered amplifier. The light is then fibre-coupled to a frequency doubler[20]. Just like the 871-nm system, The 934-nm system is also enclosed in a wooden box with inner rubber and foam lining. The local pre-stabilisation cavity is kept under vacuum at a pressure of 5×10^{-8} mbar and it is temperature controlled and water cooled, similarly to the 871-nm cavity.

---

[20] NNT Electronics WH-0467-000-A-B-C.

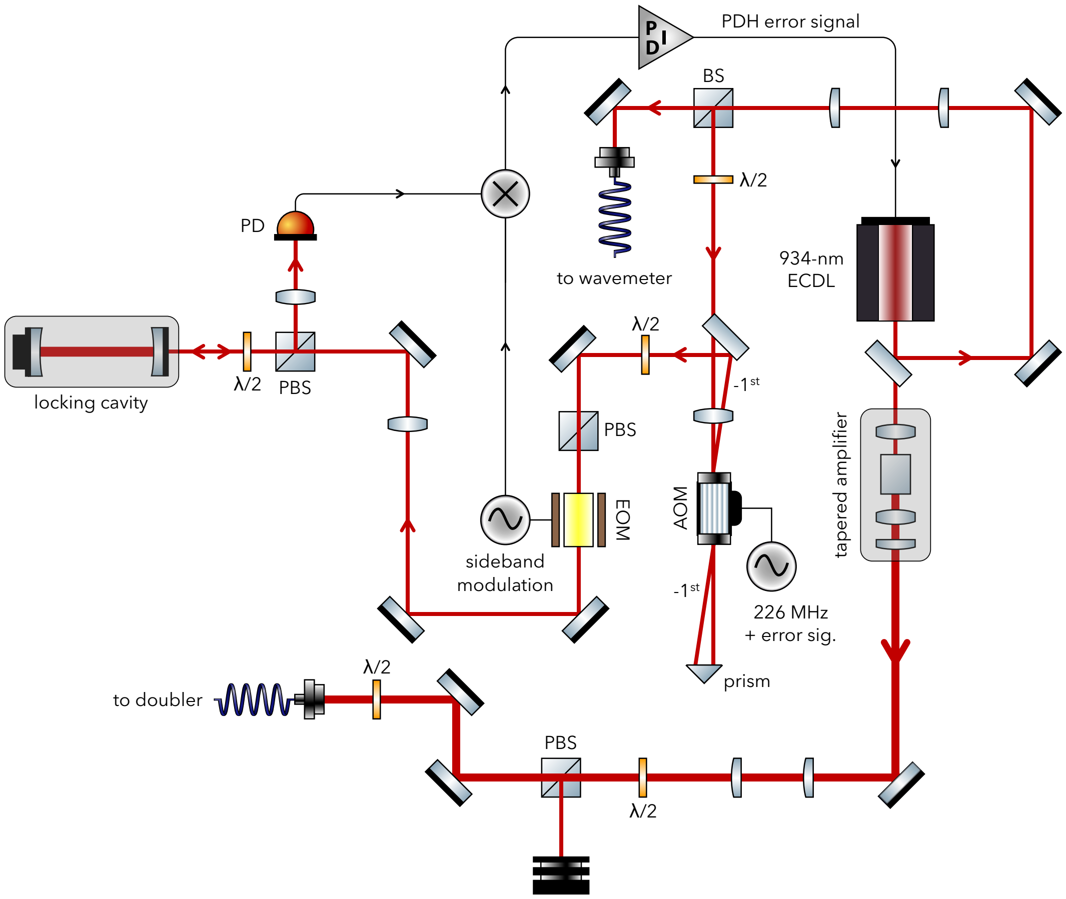

Figure A.5: Diagram of the 934-nm laser setup.

A.6 436-nm setup for probing the E2

The 436-nm setup is shown in Fig. A.6. A frequency doubler[21] outputs both 436-nm and 871-nm light, and a filter is used to block the IR and allow through the blue light. The doubling efficiency strongly depends on the temperature of the doubler, which is controlled by a Thorlabs T-cube[22] temperature controller. The 436-nm beam passes through an AOM[23] and is then coupled into a fibre that leads to the Beam Combiner.

---

[21] NNT Electronics WH-0435-000-A-B-C.

[22] TTC001.

[23] Isomet 1205C-2.

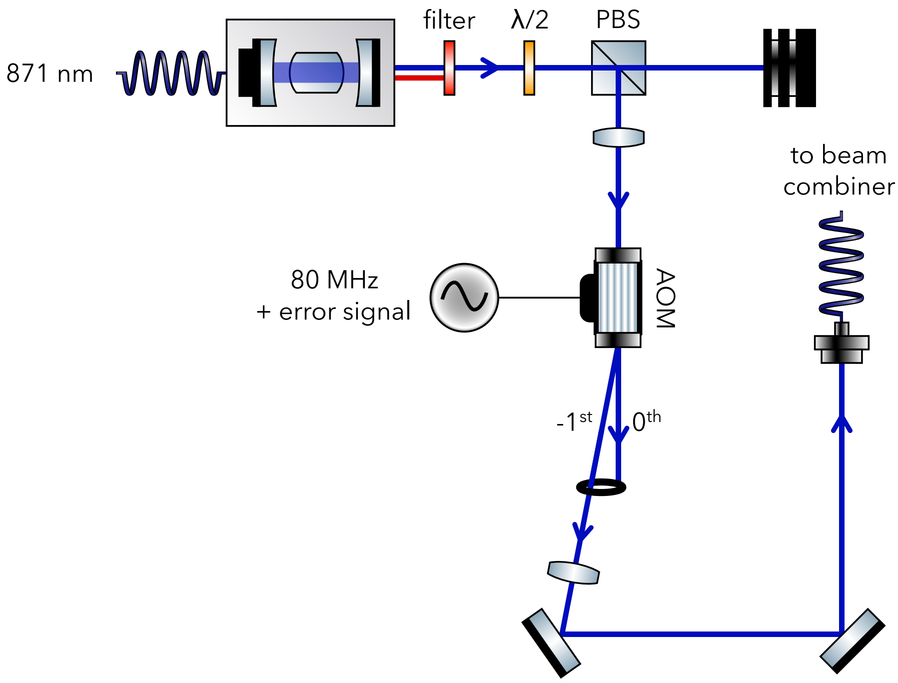

Figure A.6: Diagram of the 436-nm setup for probing the E2 transition.

Bibliography

[1] L. Essen and J. V. L. Parry. An atomic standard of frequency and time interval: a cæsium resonator. *Nature*, 176:280–282, 1955.

[2] Comptes Rendus de la 13^{e} CGPM (1967), 1969.

[3] A. Clairon, S. Ghezali, G. Santarelli, Ph. Laurent, S. N. Lea, M. Bahoura, E. Simon, S. Weyers, and K. Szymaniec. Preliminary accuracy evaluation of a cesium fountain frequency standard. *Proc. 5th Symp. Frequency Standards and Metrology, World Scientific (Singapore)*, page 45–59, 1996.

[4] R. Wynands and S. Weyers. Atomic fountain clocks. *Metrologia*, 42(3):S64–S79, 2005.

[5] H. G. Dehmelt. Monoion oscillator as potential ultimate laser frequency standard. *IEEE Transactions on Instrumentation and Measurement*, IM-31(2):83–87, 1982.

[6] S. M. Brewer, J.-S. Chen, A. M. Hankin, E. R. Clements, C. W. Chou, D. J. Wineland, D. B. Hume, and D. R. Leibrandt. $^{27}\mathrm{Al}^{+}$ quantum-logic clock with a systematic uncertainty below 10^{-18}. *Phys. Rev. Lett.*, 123:033201, 2019.

[7] C. F. A. Baynham. *Frequency metrology at the* 10^{-18} *level with an ytterbium ion optical clock*. PhD thesis, University of Oxford, 2019.

[8] D. W. Allan. Statistics of atomic frequency standards. *Proceedings of IEEE*, 54(2), 1966.

[9] W. Riley and D. Howe. Handbook of frequency stability analysis, 2008.

[10] W. M. Itano, J. C. Bergquist, J. J. Bollinger, J. M. Gilligan, D. J. Heinzen, F. L. Moore, M. G. Raizen, and D. J. Wineland. Quantum projection noise: Population fluctuations in two-level systems. *Phys. Rev. A*, 47:3554–3570, 1993.

[11] C. J. Foot. *Atomic Physics*. Oxford University Press, 2005.

[12] G. J. Dick. Local oscillator induced instabilities in trapped ion frequency standards. In *Proceedings of the 19th Annual Precise Time and Time Interval Systems and Applications Meeting*, pages 133–147, Redondo Beach, California, December 1987.

[13] Th. Udem, J. Reichert, R. Holzwarth, and T. W. Hänsch. Accurate measurement of large optical frequency differences with a mode-locked laser. *Opt. Lett.*, 24(13):881–883, 1999.

[14] S. A. Diddams, Th. Udem, J. C. Bergquist, E. A. Curtis, R. E. Drullinger, L. Hollberg, W. M. Itano, W. D. Lee, C. W. Oates, K. R. Vogel, and D. J. Wineland. An optical clock based on a single trapped $^{199}\text{Hg}^{+}$ ion. *Science*, 293:825–828, 2001.

[15] D. J. Jones, S. A. Diddams, J. K. Ranka, A. Stentz, R. S. Windeler, J. L. Hall, and S. T. Cundiff. Carrier-envelope phase control of femtosecond mode-locked lasers and direct optical frequency synthesis. *Science*, 288:635–640, 2000.

[16] R. Holzwarth, Th. Udem, and T. W. Hänsch. Optical frequency synthesizer for precision spectroscopy. *Physical Review Letters*, 85:2264–2267, 2000.

[17] H. S. Margolis. Lattice clocks embrace ytterbium. *Nature Photonics*, 3(10):557–558, 2009.

[18] W. Paul. Electromagnetic traps for charged and neutral particles. *Reviews of Modern Physics*, 62(3):531–540, 1990.

[19] N. Huntemann, C. Sanner, B. Lipphardt, Chr. Tamm, and E. Peik. Single-ion atomic clock with 3×10^{-18} systematic uncertainty. *Phys. Rev. Lett.*, 116:063001, 2016.

[20] K. Hosaka, S. A. Webster, P. J. Blythe, A. Stannard, D. Beaton, H. S. Margolis, S. N. Lea, and P. Gill. An optical frequency standard based on the electric octupole transition in $^{171}\text{Yb}^{+}$. *IEEE Transactions on Instrumentation and Measurement*, 54(2):759–762, 2005.

[21] S. A. Webster, P. Taylor, M. Roberts, G. P. Barwood, and P. Gill. Kilohertz-resolution spectroscopy of the $^{2}\text{S}_{1/2} - {}^{2}\text{F}_{7/2}$ electric octupole transition in a single $^{171}\text{Yb}^{+}$ ion. *Phys. Rev. A*, 65:052501, 2002.

[22] R. Lange, A. A. Peshkov, N. Huntemann, Chr. Tamm, A. Surzhykov, and E. Peik. Lifetime of the $^{2}\text{F}_{7/2}$ level in Yb^{+} for spontaneous emission of electric octupole radiation. *Phys. Rev. Lett.*, 127:213001, Nov 2021.

[23] T. Schneider, E. Peik, and Chr. Tamm. Sub-hertz optical frequency comparisons between two trapped $^{171}\text{Yb}^{+}$ ions. *Phys. Rev. Lett.*, 94:230801, 2005.

[24] N. Huntemann, B. Lipphardt, Chr. Tamm, V. Gerginov, S. Weyers, and E. Peik. Improved limit on a temporal variation of $m_{\mathrm{p}}/m_{\mathrm{e}}$ from comparisons of Yb^+ and Cs atomic clocks. *Phys. Rev. Lett.*, 113:210802, 2014.

[25] R. M. Godun, P. B. R. Nisbet-Jones, J. M. Jones, S. A. King, L. A. M. Johnson, H. S. Margolis, K. Szymaniec, S. N. Lea, K. Bongs, and P. Gill. Frequency ratio of two optical clock transitions in $^{171}\mathrm{Yb}^+$ and constraints on the time variation of fundamental constants. *Phys. Rev. Lett.*, 113:210801, 2014.

[26] C. Sanner, N. Huntemann, R. Lange, C. Tamm, E. Peik, M. S. Safronova, and S. G. Porsev. Optical clock comparison for Lorentz symmetry testing. *Nature*, 567(7747):204–208, 2019.

[27] H. S. Margolis. Hertz-level measurement of the optical clock frequency in a single $^{88}\mathrm{Sr}^+$ ion. *Science*, 306(5700):1355–1358, 2004.

[28] G. Barwood, G. Huang, H.A. Klein, L. Johnson, S. King, H. S. Margolis, K. Szymaniec, and P. Gill. Agreement between two $^{88}\mathrm{Sr}^+$ optical clocks to 4 parts in 10^{17}. *Physical Review A*, 89:050501(R), 2014.

[29] P. Dubé, A. A. Madej, A. Shiner, and B. Jian. $^{88}\mathrm{Sr}^+$ single-ion optical clock with a stability approaching the quantum projection noise limit. *Phys. Rev. A*, 92:042119, Oct 2015.

[30] P. Dubé, B. Jian, and A. C. Vutha. Advances in the uncertainty evaluation of a $^{88}\mathrm{Sr}^+$ single ion optical clock. In *2018 European Frequency and Time Forum (EFTF)*, pages 315–317, 2018.

[31] G. P. Barwood, C. S. Edwards, P. Gill, H. A. Klein, and W. R. C. Rowley. Observation of the $5s^2\mathrm{S}_{1/2} - 4d^2\mathrm{D}_{5/2}$ transition in a single laser-cooled trapped Sr^+ ion by using an all-solid-state system of lasers. *Opt. Lett.*, 18(9):732–734, 1993.

[32] K. Matsubara, H. Hachisu, Y. Li, S. Nagano, C. Locke, A. Nogami, M. Kajita, K. Hayasaka, T. Ido, and M. Hosokawa. Direct comparison of a Ca^+ single-ion clock against a Sr lattice clock to verify the absolute frequency measurement. *Opt. Express*, 20(20):22034–22041, Sep 2012.

[33] Y. Huang, H. Guan, M. Zeng, L. Tang, and K. Gao. $^{40}\mathrm{Ca}^{+}$ ion optical clock with micromotion-induced shifts below 1×10^{-18}. *Phys. Rev. A*, 99:011401, Jan 2019.

[34] C. Champenois, M. Houssin, C. Lisowski, M. Knoop, G. Hagel, M. Vedel, and F. Vedel. Evaluation of the ultimate performances of a Ca^{+} single-ion frequency standard. *Physics Letters A*, 331(5):298–311, 2004.

[35] Y. Huang, J. Cao, P. Liu, K. Liang, B. Ou, H. Guan, X. Huang, T. Li, and K. Gao. Hertz-level measurement of the $^{40}\mathrm{Ca}^{+}$ $4s^2\mathrm{S}_{1/2} - 3d^2\mathrm{D}_{5/2}$ clock transition frequency with respect to the SI second through the Global Positioning System. *Physical Review A*, 85(3), 2012.

[36] J. Cao, P. Zhang, J. Shang, K. Cui, J. Yuan, S. Chao, S. Wang, H. Shu, and X. Huang. A compact, transportable single-ion optical clock with 7.8×10^{-17} systematic uncertainty. *Applied Physics B*, 123(4), 2017.

[37] Th. Udem, S. A. Diddams, K. R. Vogel, C. W. Oates, E. A. Curtis, W. D. Lee, W. M. Itano, R. E. Drullinger, J. C. Bergquist, and L. Hollberg. Absolute frequency measurements of the Hg^{+} and Ca optical clock transitions with a femtosecond laser. *Phys. Rev. Lett.*, 86:4996–4999, 2001.

[38] W. H. Oskay, S. A. Diddams, E. A. Donley, T. M. Fortier, T. P. Heavner, L. Hollberg, W. M. Itano, S. R. Jefferts, M. J. Delaney, K. Kim, F. Levi, T. E. Parker, and J. C. Bergquist. Single-atom optical clock with high accuracy. *Phys. Rev. Lett.*, 97:020801, 2006.

[39] T. Rosenband, D. B. Hume, P. O. Schmidt, C. W. Chou, A. Brusch, L. Lorini, W. H. Oskay, R. E. Drullinger, T. M. Fortier, J. E. Stalnaker, S. A. Diddams, W. C. Swann, N. R. Newbury, W. M. Itano, D. J. Wineland, and J. C. Bergquist. Frequency ratio of Al^{+} and Hg^{+} single-ion optical clocks; metrology at the 17th decimal place. *Science*, 319(5871):1808–1812, 2008.

[40] W. M. Itano. External-field shifts of the $^{199}\mathrm{Hg}^{+}$ optical frequency standard. *J. Res. Natl. Inst. Stand. Technol.*, 105(6):829–837, 2000.

[41] H. S. Margolis. Optical frequency standards and clocks. *Contemporary Physics*, 51(1):37–58, 2010.

[42] M. S. Safronova, M. G. Kozlov, and Charles W. Clark. Precision calculation of blackbody radiation shifts for optical frequency metrology. *Phys. Rev. Lett.*, 107:143006, 2011.

[43] T. Rosenband, W. M. Itano, P. O. Schmidt, D. B. Hume, J. C. J. Koelemeij, J. C. Bergquist, and D. J. Wineland. Blackbody radiation shift of the $^{27}\mathrm{Al}^{+}\ {}^{1}\mathrm{S}_{0} - {}^{3}\mathrm{P}_{0}$ transition. In *Proceedings of the 20th European Frequency and Time Forum*, pages 289–292, 2006.

[44] P. O. Schmidt, T. Rosenband, C. Langer, W. M. Itano, J. C. Bergquist, and D. J. Wineland. Spectroscopy using quantum logic. *Science*, 309(5735):749–752, 2005.

[45] C. W. Chou, D. B. Hume, J. C. J. Koelemeij, D. J. Wineland, and T. Rosenband. Frequency comparison of two high-accuracy Al^{+} optical clocks. *Phys. Rev. Lett.*, 104:070802, 2010.

[46] S. Hannig, L. Pelzer, N. Scharnhorst, J. Kramer, M. Stepanova, Z. T. Xu, N. Spethmann, I. D. Leroux, T. E. Mehlstäubler, P. O. Schmidt, et al. Towards a transportable aluminium ion quantum logic optical clock. *Review of Scientific Instruments*, 90(5):053204, 2019.

[47] H. Häffner, C. Roos, and R. Blatt. Quantum computing with trapped ions. *Physics Reports*, 469(4):155–203, 2008.

[48] N. Ohtsubo, Y. Li, K. Matsubara, T. Ido, and K. Hayasaka. Frequency measurement of the clock transition of an indium ion sympathetically-cooled in a linear trap. *Opt. Express*, 25(10):11725–11735, May 2017.

[49] N. Ohtsubo, Y. Li, K. Matsubara, N. Nemitz, H. Hachisu, T. Ido, and K. Hayasaka. Optical clock based on a sympathetically-cooled indium ion. *Hyperfine Interactions*, 240(39), 2019.

[50] H. Katori. *Spectroscopy of strontium atoms in the Lamb-Dicke confinement*, pages 323–330. World Scientific, 2002.

[51] P. S. Jessen and I. H. Deutsch. Optical lattices. In *Advances In Atomic, Molecular, and Optical Physics*, volume 37, pages 95 – 138. Academic Press, 1996.

[52] H. Katori, M. Takamoto, V. G. Pal'chikov, and V. D. Ovsiannikov. Ultrastable optical clock with neutral atoms in an engineered light shift trap. *Phys. Rev. Lett.*, 91:173005, Oct 2003.

[53] M. Takamoto and H. Katori. Spectroscopy of the $^1\mathrm{S}_0 - {}^3\mathrm{P}_0$ clock transition of $^{87}\mathrm{Sr}$ in an optical lattice. *Phys. Rev. Lett.*, 91:223001, Nov 2003.

[54] A. D. Ludlow, T. Zelevinsky, G. K. Campbell, S. Blatt, M. M. Boyd, M. H. G. De Miranda, M. J. Martin, J. W. Thomsen, S. M. Foreman, J. Ye, et al. Sr lattice clock at 1×10^{-16} fractional uncertainty by remote optical evaluation with a Ca clock. *Science*, 319(5871):1805–1808, 2008.

[55] R. Le Targat, L. Lorini, Y. Le Coq, M. Zawada, J. Guéna, M. Abgrall, M. Gurov, P. Rosenbusch, D. G. Rovera, B. Nagórny, et al. Experimental realization of an optical second with strontium lattice clocks. *Nature Communications*, 4(1), 2013.

[56] S. Falke, N. Lemke, C. Grebing, B. Lipphardt, S. Weyers, V. Gerginov, N. Huntemann, C. Hagemann, A. Al-Masoudi, S. Häfner, S. Vogt, U. Sterr, and C. Lisdat. A strontium lattice clock with 3×10^{-17} inaccuracy and its frequency. *New Journal of Physics*, 16(7):073023, 2014.

[57] T. Bothwell, D. Kedar, E. Oelker, J. M. Robinson, S. L. Bromley, W. L. Tew, J. Ye, and C. J. Kennedy. JILA SrI optical lattice clock with uncertainty of 2×10^{-18}. *Metrologia*, 56(6):065004, Oct 2019.

[58] R. Hobson, W. Bowden, A. Vianello, A. Silva, C. F. A. Baynham, H. S. Margolis, P. E. G Baird, P. Gill, and I. R. Hill. A strontium optical lattice clock with 1×10^{-17} uncertainty and measurement of its absolute frequency. *Metrologia*, 57(6):065026, Oct 2020.

[59] C. W. Hoyt, Z. W. Barber, C. W. Oates, T. M. Fortier, S. A. Diddams, and L. Hollberg. Observation and absolute frequency measurements of the $^1\mathrm{S}_0 - {}^3\mathrm{P}_0$ optical clock transition in neutral ytterbium. *Phys. Rev. Lett.*, 95:083003, Aug 2005.

[60] M. Pizzocaro, G. A. Costanzo, A. Godone, F. Levi, A. Mura, M. Zoppi, and D. Calonico. Realization of an ultrastable 578-nm laser for an Yb lattice clock. *IEEE Transactions on Ultrasonics Ferroelectrics and Frequency Control*, 59(3):426–431, 2012.

[61] W. F. McGrew, X. Zhang, R. J. Fasano, S. A. Schäffer, K. Beloy, D. Nicolodi, R. C. Brown, N. Hinkley, G. Milani, M. Schioppo, T. H. Yoon, and A. D. Ludlow. Atomic clock performance enabling geodesy below the centimetre level. *Nature*, 564:87–90, 2018.

[62] Q. Gao, M. Zhou, C. Han, S. Li, S. Zhang, Y. Yao, B. Li, H. Qiao, D. Ai, G. Lou, et al. Systematic evaluation of a ^{171}Yb optical clock by synchronous comparison between two lattice systems. *Scientific Reports*, 8(1), 2018.

[63] T. Kobayashi, D. Akamatsu, Y. Hisai, T. Tanabe, H. Inaba, T. Suzuyama, F. Hong, K. Hosaka, and M. Yasuda. Uncertainty evaluation of an ^{171}yb optical lattice clock at NMIJ. *IEEE Transactions on Ultrasonics, Ferroelectrics, and Frequency Control*, 65(12):2449–2458, 2018.

[64] M. Takamoto, I. Ushijima, M. Das, N. Nemitz, T. Ohkubo, K. Yamanaka, N. Ohmae, T. Takano, T. Akatsuka, A. Yamaguchi, et al. Frequency ratios of Sr, Yb, and Hg based optical lattice clocks and their applications. *Comptes Rendus Physique*, 16(5):489–498, 2015.

[65] R. Tyumenev, M. Favier, S. Bilicki, E. Bookjans, R. Le Targat, J. Lodewyck, D. Nicolodi, Y. Le Coq, M. Abgrall, J. Guéna, et al. Comparing a mercury optical lattice clock with microwave and optical frequency standards. *New Journal of Physics*, 18(11):113002, 2016.

[66] C. Guo, M. Favier, J. Calvert, V. Cambier, N. Galland, L. De Sarlo, and S. Bize. A mercury optical lattice clock with improved magic wavelength control. In *2017 Joint Conference of the European Frequency and Time Forum and IEEE International Frequency Control Symposium (EFTF/IFCS)*, pages 498–499, 2017.

[67] X. Baillard, M. Fouché, R. Le Targat, P. G. Westergaard, A. Lecallier, Y. Le Coq, G. D. Rovera, S. Bize, and P. Lemonde. Accuracy evaluation of an optical lattice clock with bosonic atoms. *Optics Letters*, 32(13):1812, 2007.

[68] Ch. Lisdat, J. S. R. Vellore Winfred, T. Middelmann, F. Riehle, and U. Sterr. Collisional losses, decoherence, and frequency shifts in optical lattice clocks with bosons. *Phys. Rev. Lett.*, 103:090801, Aug 2009.

[69] T. Akatsuka, M. Takamoto, and H. Katori. Three-dimensional optical lattice clock with bosonic ^{88}Sr atoms. *Phys. Rev. A*, 81:023402, Feb 2010.

[70] Z. W. Barber, C. W. Hoyt, C. W. Oates, L. Hollberg, A. V. Taichenachev, and V. I. Yudin. Direct excitation of the forbidden clock transition in neutral ^{174}Yb atoms confined to an optical lattice. *Phys. Rev. Lett.*, 96:083002, Mar 2006.

[71] N. Poli, Z. W. Barber, N. D. Lemke, C. W. Oates, L. S. Ma, J. E. Stalnaker, T. M. Fortier, S. A. Diddams, L. Hollberg, J. C. Bergquist, et al. Frequency evaluation of the doubly forbidden $^1\mathrm{S}_0 - {}^3\mathrm{P}_0$ transition in bosonic ^{174}Yb. *Physical Review A*, 77(5):050501, May 2008.

[72] Y. B. Band and A. Vardi. Collisional shifts in optical-lattice atom clocks. *Phys. Rev. A*, 74:033807, Sep 2006.

[73] J. C. Berengut, V. A. Dzuba, and V. V. Flambaum. Enhanced laboratory sensitivity to variation of the fine-structure constant using highly charged ions. *Phys. Rev. Lett.*, 105:120801, 2010.

[74] V. A. Dzuba and V. V. Flambaum. Highly charged ions for atomic clocks and search for variation of the fine structure constant. In *TCP 2014*, pages 79–86. Springer International Publishing, Mar 2015.

[75] M. G. Kozlov, M. S. Safronova, J. R. Crespo López-Urrutia, and P. O. Schmidt. Highly charged ions: Optical clocks and applications in fundamental physics. *Rev. Mod. Phys.*, 90:045005, 2018.

[76] S. A. King, L. J. Spieß, P. Micke, A. Wilzewski, T. Leopold, E. Benkler, R. Lange, N. Huntemann, A. Surzhykov, V. A. Yerokhin, J. R. C. López-Urrutia, and P. O. Schmidt. An optical atomic clock based on a highly charged ion. *arXiv*, 2022.

[77] G. Barontini, L. Blackburn, V. Boyer, et al. Measuring the stability of fundamental constants with a network of clocks. *EPJ Quantum Technology*, 9(12), May 2022.

[78] V. V. Flambaum. Enhanced effect of temporal variation of the fine structure constant and the strong interaction in ^{229}Th. *Phys. Rev. Lett.*, 97:092502, 2006.

[79] A. Hayes, J. Friar, and P. Moeller. Splitting sensitivity of the ground and 7.6 eV isomeric states of ^{229}Th. *Physical Review C - PHYS REV C*, 78:024311–024311, 2008.

[80] L. Von Der Wense and B. Seiferle. The ^{229}Th isomer: prospects for a nuclear optical clock. *The European Physical Journal A*, 56(11), 2020.

[81] E. Peik, T. Schumm, M. S. Safronova, A. Pálffy, J. Weitenberg, and P. G. Thirolf. Nuclear clocks for testing fundamental physics. *Quantum Science and Technology*, 6(3):034002, Apr 2021.

[82] A. Yamaguchi, M. Kolbe, H. Kaser, T. Reichel, A. Gottwald, and E. Peik. Experimental search for the low-energy nuclear transition in ^{229}Th with undulator radiation. *New Journal of Physics*, 17(5):053053, 2015.

[83] E. Peik and M. Okhapkin. Nuclear clocks based on resonant excitation of γ-transitions. *Comptes Rendus Physique*, 16(5):516–523, 2015.

[84] M. E. Kim, W. F. McGrew, N. V. Nardelli, E. R. Clements, Y. S. Hassan, X. Zhang, J. L. Valencia, H. Leopardi, D. B. Hume, T. M. Fortier, A. D. Ludlow, and D. R. Leibrandt. Optical coherence between atomic species at the second scale: improved clock comparisons via differential spectroscopy, 2021.

[85] D. B. Hume and D. R. Leibrandt. Probing beyond the laser coherence time in optical clock comparisons. *Phys. Rev. A*, 93:032138, Mar 2016.

[86] P. Gill. When should we change the definition of the second? *Phil. Trans. R. Soc. A*, 369:4109–4130, 2011.

[87] F. Riehle, P. Gill, F. Arias, and L. Robertsson. The CIPM list of recommended frequency standard values: guidelines and procedures. *Metrologia*, 55(2):188–200, 2018.

[88] Microsemi. *MHM 2010 Active Hydrogen Maser Datasheet.*

[89] M. Pizzocaro, P. Thoumany, B. Rauf, F. Bregolin, G. Milani, C. Clivati, G. A Costanzo, F. Levi, and D. Calonico. Absolute frequency measurement of the $^1S_0 - {}^3P_0$ transition of ^{171}Yb. *Metrologia*, 54(1):102–112, Jan 2017.

[90] W. F. McGrew, X. Zhang, H. Leopardi, R. J. Fasano, D. Nicolodi, K. Beloy, J. Yao, J. A. Sherman, S. A. Schäffer, J. Savory, et al. Towards the optical second: verifying optical clocks at the SI limit. *Optica*, 6(4):448, 2019.

[91] J. Lodewyck, S. Bilicki, E. Bookjans, J. Robyr, C. Shi, G. Vallet, R. Le Targat, D. Nicolodi, Y. Le Coq, J. Guéna, M. Abgrall, P. Rosenbusch, and S. Bize. Optical to microwave clock frequency ratios with a nearly continuous strontium optical lattice clock. *Metrologia*, 53(4):1123–1130, 2016.

[92] H. Kim, M.-S. Heo, W.-K. Lee, C. Y. Park, H.-G. Hong, S.-W. Hwang, and D.-H. Yu. Improved absolute frequency measurement of the ^{171}Yb optical lattice clock at KRISS relative to the SI second. *Japanese Journal of Applied Physics*, 56(5):050302, 2017.

[93] H. Hachisu, G. Petit, F. Nakagawa, Y. Hanado, and T. Ido. SI-traceable measurement of an optical frequency at the low 10^{-16} level without a local primary standard. *Optics Express*, 25(8):8511, 2017.

[94] C. F. A. Baynham, R. M. Godun, J. M. Jones, S. A. King, P. B. R. Nisbet-Jones, F. Baynes, A. Rolland, P. E. G. Baird, K. Bongs, P. Gill, and H. S. Margolis. Absolute frequency measurement of the optical clock transition $^2S_{1/2} - {}^2F_{7/2}$ in $^{171}Yb^+$ with an uncertainty of 4×10^{-16} using a frequency link to international atomic time. *Journal of Modern Optics*, 65(5-6):585–591, 2018.

[95] R. M. Godun, C. F. A. Baynham, J. M. Jones, S. A. King, P. B. R. Nisbet-Jones, F. Baynes, A. Rolland, P. E. G. Baird, K. Bongs, P. Gill, G. Petit, and H. S. Margolis. Absolute frequency measurement of the ytterbium ion E3 optical clock transition using international atomic time. In *2018 European Frequency and Time Forum (EFTF)*, pages 312–314, 2018.

[96] M. Pizzocaro, F. Bregolin, P. Barbieri, B. Rauf, F. Levi, and D. Calonico. Absolute frequency measurement of the $^1S_0 - {}^3P_0$ transition of ^{171}Yb with a link to international atomic time. *Metrologia*, 57(3):035007, 2020.

[97] H. S. Margolis and P. Gill. Least-squares analysis of clock frequency comparison data to deduce optimized frequency and frequency ratio values. *Metrologia*, 52(5):628–634, 2015.

[98] N. Hinkley, J. A. Sherman, N. B. Phillips, M. Schioppo, N. D. Lemke, K. Beloy, M. Pizzocaro, C. W. Oates, and A. D. Ludlow. An atomic clock with 10^{-18} instability. *Science*, 341(6151):1215–1218, 2013.

[99] D. Akamatsu, M. Yasuda, H. Inaba, K. Hosaka, T. Tanabe, A. Onae, and F.-L. Hong. Frequency ratio measurement of ^{171}Yb^{+} and ^{87}Sr optical lattice clocks. *Optics Express*, 22(7):7898, 2014.

[100] N. Ohtsubo, Y. Li, N. Nemitz, H. Hachisu, K. Matsubara, T. Ido, and K. Hayasaka. Frequency ratio of an ^{115}In^{+} ion clock and a ^{87}Sr optical lattice clock. *Opt. Lett.*, 45(21):5950–5953, Nov 2020.

[101] S. Dörscher, N. Huntemann, R. Schwarz, R. Lange, E. Benkler, B. Lipphardt, U. Sterr, E. Peik, and C. Lisdat. Optical frequency ratio of a ^{171}Yb^{+} single-ion clock and a ^{87}Sr lattice clock. *Metrologia*, 58(1):015005, Jan 2021.

[102] R. Lange, N. Huntemann, J. M. Rahm, C. Sanner, H. Shao, B. Lipphardt, Chr. Tamm, S. Weyers, and E. Peik. Improved limits for violations of local position invariance from atomic clock comparisons. *Phys. Rev. Lett.*, 126:011102, Jan 2021.

[103] F. Riehle. Optical clock networks. *Nature Photonics*, 11(1):25–31, 2017.

[104] W. R. Milner, J. M. Robinson, C. J. Kennedy, T. Bothwell, D. Kedar, D. G. Matei, T. Legero, U. Sterr, F. Riehle, H. Leopardi, T. M. Fortier, J. A. Sherman, J. Levine, J. Yao, J. Ye, and E. Oelker. Demonstration of a timescale based on a stable optical carrier. *Phys. Rev. Lett.*, 123:173201, Oct 2019.

[105] M. Fujieda, M. Kumagai, S. Nagano, A. Yamaguchi, H. Hachisu, and T. Ido. All-optical link for direct comparison of distant optical clocks. *Optics Express*, 19(17):16498, 2011.

[106] C. Lisdat, G. Grosche, N. Quintin, C. Shi, S.M.F. Raupach, C. Grebing, D. Nicolodi, F. Stefani, A. Al-Masoudi, S. Dörscher, et al. A clock network for geodesy and fundamental science. *Nature Communications*, 7(1):12443, 2016.

[107] P. Delva, J. Lodewyck, S. Bilicki, E. Bookjans, G. Vallet, R. Le Targat, P.-E. Pottie, C. Guerlin, F. Meynadier, C. Le Poncin-Lafitte, O. Lopez, A. Amy-Klein, W.-K. Lee,

N. Quintin, C. Lisdat, A. Al-Masoudi, S. Dörscher, et al. Test of special relativity using a fiber network of optical clocks. *Phys. Rev. Lett.*, 118:221102, 2017.

[108] B. M. Roberts, P. Delva, et al. Search for transient variations of the fine structure constant and dark matter using fiber-linked optical atomic clocks. *New Journal of Physics*, 22(9):093010, Sep 2020.

[109] K. Yamanaka, N. Ohmae, I. Ushijima, M. Takamoto, and H. Katori. Frequency ratio of ^{199}Hg and ^{87}Sr optical lattice clocks beyond the SI limit. *Phys. Rev. Lett.*, 114:230801, Jun 2015.

[110] N. Nemitz, T. Ohkubo, M. Takamoto, I. Ushijima, M. Das, N. Ohmae, and H. Katori. Frequency ratio of Yb and Sr clocks with 5×10^{-17} uncertainty at 150 seconds averaging time. *Nature Photonics*, 10(4):258–261, 2016.

[111] N. Ohmae, F. Bregolin, N. Nemitz, and H. Katori. Direct measurement of the frequency ratio for Hg and Yb optical lattice clocks and closure of the Hg/Yb/Sr loop. *Opt. Express*, 28(10):15112–15121, May 2020.

[112] S. N. Lea. Limits to time variation of fundamental constants from comparisons of atomic frequency standards. *Reports on Progress in Physics*, 70(9):1473–1523, 2007.

[113] E. J. Angstmann, V. A. Dzuba, and V. V. Flambaum. Atomic clocks and the search for variation of the fine structure constant. *arXiv e-prints*, 2004.

[114] V. V. Flambaum and V. A. Dzuba. Search for variation of the fundamental constants in atomic, molecular and nuclear spectra. *Canadian Journal of Physics*, 87(1):25–33, 2009.

[115] M. S. Safronova. The search for variation of fundamental constants with clocks. *Annalen der Physik*, 531(5):1800364, 2019.

[116] P. Wcisło, P. Ablewski, K. Beloy, S. Bilicki, M. Bober, R. Brown, R. Fasano, R. Ciuryło, H. Hachisu, T. Ido, J. Lodewyck, A. Ludlow, W. McGrew, P. Morzyński, D. Nicolodi, M. Schioppo, M. Sekido, R. Le Targat, P. Wolf, X. Zhang, B. Zjawin, and M. Zawada. New bounds on dark matter coupling from a global network of optical atomic clocks. *Science Advances*, 4(12):eaau4869, 2018.

[117] A. Derevianko and M. Pospelov. Hunting for topological dark matter with atomic clocks. *Nature Physics*, 10(12):933–936, 2014.

[118] B. M. Roberts, G. Blewitt, C. Dailey, et al. Search for domain wall dark matter with atomic clocks on board global positioning system satellites. *Nature Communications*, 8(1195), 2017.

[119] P. Wcisło, P. Morzyński, M. Bober, A. Cygan, D. Lisak, R. Ciuryło, and M. Zawada. Experimental constraint on dark matter detection with optical atomic clocks. *Nature Publishing Group*, 1(9):1–6, 2016.

[120] R. F. C. Vessot, M. W. Levine, E. M. Mattison, E. L. Blomberg, T. E. Hoffman, G. U. Nystrom, B. F. Farrel, R. Decher, P. B. Eby, C. R. Baugher, J. W. Watts, D. L. Teuber, and F. D. Wills. Test of relativistic gravitation with a space-borne hydrogen maser. *Phys. Rev. Lett.*, 45:2081–2084, 1980.

[121] P. Vanicek, R. O. Castle, and E. I. Balazs. Geodetic leveling and its applications. *Reviews of Geophysics*, 18(2):505–524, 1980.

[122] H. Denker, L. Timmen, C. Voigt, S. Weyers, E. Peik, H. S. Margolis, P. Delva, P. Wolf, and G. Petit. Geodetic methods to determine the relativistic redshift at the level of 10^{-18} in the context of international timescales: a review and practical results. *Journal of Geodesy*, 92:487—516, 2018.

[123] T. E. Mehlstäubler, G. Grosche, C. Lisdat, P. O. Schmidt, and H. Denker. Atomic clocks for geodesy. *Reports on Progress in Physics*, 81(6):064401, 2018.

[124] J. Grotti, S. Koller, S. Vogt, et al. Geodesy and metrology with a transportable optical clock. *Nature Physics*, 14, 2018.

[125] S. B. Koller, J. Grotti, St. Vogt, A. Al-Masoudi, S. Dörscher, S. Häfner, U. Sterr, and Ch. Lisdat. Transportable optical lattice clock with 7×10^{-17} uncertainty. *Phys. Rev. Lett.*, 118:073601, 2017.

[126] M. Takamoto, I. Ushijima, N. Ohmae, T. Yahagi, K. Kokado, H. Shinkai, and H. Katori. Test of general relativity by a pair of transportable optical lattice clocks. *Nature Photonics*, 14(7):411–415, 2020.

[127] N. Ohmae, M. Takamoto, Y. Takahashi, M. Kokubun, K. Araki, A. Hinton, I. Ushijima, T. Muramatsu, T. Furumiya, Y. Sakai, et al. Transportable strontium optical lattice clocks operated outside laboratory at the level of 10^{-18} uncertainty. *Advanced Quantum Technologies*, 4(8):2100015, 2021.

[128] R. Bondarescu, M. Bondarescu, G. Hetényi, L. Boschi, P. Jetzer, and J. Balakrishna. Geophysical applicability of atomic clocks: direct continental geoid mapping. *Geophysical Journal International*, 191(1):78–82, 2012.

[129] R. Bondarescu, A. Schärer, A. Lundgren, G. Hetényi, N. Houlié, P. Jetzer, and M. Bondarescu. Ground-based optical atomic clocks as a tool to monitor vertical surface motion. *Geophysical Journal International*, 202(3):1770–1774, 2015.

[130] H. Hachisu, M. Fujieda, S. Nagano, T. Gotoh, A. Nogami, T. Ido, St. Falke, N. Huntemann, C. Grebing, B. Lipphardt, et al. Direct comparison of optical lattice clocks with an intercontinental baseline of 9000 km. *Optics Letters*, 39(14):4072, 2014.

[131] P. A. Williams, W. C. Swann, and N. R. Newbury. High-stability transfer of an optical frequency over long fiber-optic links. *J. Opt. Soc. Am. B*, 25(8):1284–1293, 2008.

[132] N. R. Newbury, P. A. Williams, and W. C. Swann. Coherent transfer of an optical carrier over 251 km. *Opt. Lett.*, 32(21):3056–3058, 2007.

[133] S. Origlia, M. S. Pramod, S. Schiller, Y. Singh, K. Bongs, R. Schwarz, A. Al-Masoudi, S. Dörscher, S. Herbers, S. Häfner, U. Sterr, and Ch. Lisdat. Towards an optical clock for space: Compact, high-performance optical lattice clock based on bosonic atoms. *Phys. Rev. A*, 98:053443, 2018.

[134] N. Poli, M. Schioppo, S. Vogt, St. Falke, U. Sterr, Ch. Lisdat, and G. M. Tino. A transportable strontium optical lattice clock. *Applied Physics B*, 117(4):1107–1116, 2014.

[135] J. Cao, J. Yuan, S. Wang, P. Zhang, Y. Yuan, D. Liu, K. Cui, S. Chao, H. Shu, Y. Lin, S. Cao, Y. Wang, Z. Fang, F. Fang, T. Li, and X. Huang. A compact, transportable optical clock with 1×10^{-17} uncertainty and its absolute frequency measurement. *Applied Physics Letters*, 120(5):054003, 2022.

[136] M. Lezius, T. Wilken, C. Deutsch, M. Giunta, O. Mandel, A. Thaller, V. Schkolnik, M. Schiemangk, A. Dinkelaker, A. Kohfeldt, A. Wicht, M. Krutzik, A. Peters, O. Hellmig, H. Duncker, K. Sengstock, P. Windpassinger, K. Lampmann, T. Hülsing, T. W. Hänsch, and R. Holzwarth. Space-borne frequency comb metrology. *Optica*, 3(12):1381–1387, 2016.

[137] J. R. de Laeter, J. K. Böhlke, P. De Bièvre, H. Hidaka, H. S. Peiser, K. J. R. Rosman, and P. D. P. Taylor. Atomic weights of the elements. review 2000 (IUPAC Technical Report). *Pure and Applied Chemistry*, 75(6):683–800, 2003.

[138] S. Olmschenk, D. Hayes, D. N. Matsukevich, P. Maunz, D. L. Moehring, K. C. Younge, and C. Monroe. Measurement of the lifetime of the $6p\ ^2\mathrm{P}^o_{1/2}$ level of Yb^+. *Phys. Rev. A*, 80:022502, Aug 2009.

[139] S. Olmschenk, K. C. Younge, D. L. Moehring, D. N. Matsukevich, P. Maunz, and C. Monroe. Manipulation and detection of a trapped Yb^+ hyperfine qubit. *Phys. Rev. A*, 76:052314, 2007.

[140] R. W. Berends, E. H. Pinnington, B. Guo, and Q. Ji. Beam-laser lifetime measurements for four resonance levels of Yb II. *Journal of Physics B: Atomic, Molecular and Optical Physics*, 26(20):L701–L704, Oct 1993.

[141] E. H. Pinnington, R. W. Berends, and Q. Ji. Beam-laser lifetime measurements of Yb II energy levels. *Phys. Rev. A*, 50:2758–2760, Sep 1994.

[142] M. Kleinert, M. E. Gold Dahl, and S. Bergeson. Measurement of the Yb I $^1\mathrm{S}_0-^1\mathrm{P}_1$ transition frequency at 399 nm using an optical frequency comb. *Phys. Rev. A*, 94:052511, Nov 2016.

[143] Alexander Franzen. ComponentLibrary. `http://www.gwoptics.org/ComponentLibrary/`.

[144] P. B. R. Nisbet-Jones, S. A. King, J. M. Jones, R. M. Godun, C. F. A. Baynham, K. Bongs, M. Doležal, P. Balling, and P. Gill. A single-ion trap with minimized ion-environment interactions. *Applied Physics B*, 122(3):57, 2016.

[145] C. A. Schrama, E. Peik, W. W. Smith, and H. Walther. Novel miniature ion traps. *Optics communications*, 101:32–36, 1993.

[146] D. J. Wineland and H. Dehmelt. Proposed 10^{14} $\delta\nu < \nu$ laser fluorescence spectroscopy on Tl^+ mono-ion oscillator III. *Bulletin of the American Physical Society*, 20(637), 1975.

[147] D. J. Wineland and W. M. Itano. Laser cooling of atoms. *Phys. Rev. A*, 20:1521–1540, Oct 1979.

[148] T. W. Hänsch and A. L. Schawlow. Cooling of gases by laser radiation. *Optics Communications*, 13(1):68–69, 1975.

[149] D. J. Berkeland and M. G. Boshier. Destabilization of dark states and optical spectroscopy in Zeeman-degenerate atomic systems. *Phys. Rev. A*, 65:033413, Feb 2002.

[150] V. Letchumanan, P. Gill, E. Riis, and A. G. Sinclair. Optical ramsey spectroscopy of a single trapped $^{88}Sr^+$ ion. *Phys. Rev. A*, 70:033419, Sep 2004.

[151] J. Schat. Using the Thue-Morse sequence to cancel low-frequency fluctuations. In *2007 IEEE Instrumentation & Measurement Technology Conference IMTC 2007*, pages 1–6, 2007.

[152] E. D. Black. An introduction to Pound–Drever–Hall laser frequency stabilization. *American Journal of Physics*, 69(1):79–87, 2001.

[153] M. Schioppo, J. Kronjäger, A. Silva, R. Ilieva, J. W. Paterson, C. F. A. Baynham, W. Bowden, I. R. Hill, R. Hobson, A. Vianello, et al. Comparing ultrastable lasers at 7×10^{-17} fractional frequency instability through a 2220 km optical fibre network. *Nature Communications*, 13(1), 2022.

[154] H. R. Telle, B. Lipphardt, and J. Stenger. Kerr-lens, mode-locked lasers as transfer oscillators for optical frequency measurements. *Applied Physics B*, 74(1):1–6, 2002.

[155] Artiq experimental control description. `https://m-labs.hk/experiment-control/artiq/`.

[156] InfluxDB homepage. `https://www.influxdata.com`.

[157] Grafana homepage. `https://grafana.com`.

[158] J. Keller, H. L. Partner, T. Burgermeister, and T. E. Mehlstäubler. Precise determination of micromotion for trapped-ion optical clocks. *Journal of Applied Physics*, 118(10):104501, 2015.

[159] I. Lizuain, J. G. Muga, and J. Eschner. Motional frequency shifts of trapped ions in the Lamb-Dicke regime. *Phys. Rev. A*, 76:033808, Sep 2007.

[160] P. Dubé, A. A. Madej, Z. Zhou, and J. E. Bernard. Evaluation of systematic shifts of the $^{88}\mathrm{Sr}^{+}$ single-ion optical frequency standard at the 10^{-17} level. *Phys. Rev. A*, 87:023806, Feb 2013.

[161] G. K. Woodgate. *Elementary Atomic Structure*, page 189. Oxford University Press, USA, second edition, 1980.

[162] R. Lange, N. Huntemann, C. Sanner, H. Shao, B. Lipphardt, Chr. Tamm, and E. Peik. Coherent suppression of tensor frequency shifts through magnetic field rotation. *Phys. Rev. Lett.*, 125:143201, Sep 2020.

[163] R. Storn and K. Price. Differential evolution – a simple and efficient heuristic for global optimization over continuous spaces. *Journal of Global Optimization*, 11:341–359, 1997.

[164] J. Tellinghuisen. Statistical error propagation. *The Journal of Physical Chemistry A*, 105(15):3917–3921, 2001.

[165] H. C. J. Gan, G. Maslennikov, K.-W. Tseng, T. R. Tan, R. Kaewuam, K. J. Arnold, D. Matsukevich, and M. D. Barrett. Oscillating-magnetic-field effects in high-precision metrology. *Phys. Rev. A*, 98:032514, 2018.

[166] B. R. Eichelberger, T. P. Snow, and V. M. Bierbaum. Collision rate constants for polarizable ions. *Journal of the American Society for Mass Spectrometry*, 14(5):501–505, 2003.

[167] E. Oelker, R. B. Hutson, C. J. Kennedy, L. Sonderhouse, T. Bothwell, A. Goban, D. Kedar, C. Sanner, J. M. Robinson, G. E. Marti, et al. Demonstration of 4.8×10^{-17} stability at 1 s for two independent optical clocks. *Nature Photonics*, 13(10):714–719, 2019.

[168] G. Petit, F. Arias, and G. Panfilo. International atomic time: Status and future challenges. *Comptes Rendus Physique*, 16(5):480–488, 2015.

[169] G. Panfilo and F. Arias. The Coordinated Universal Time (UTC). *Metrologia*, 56(4):042001, 2019.

[170] BIPM Circular T. `https://www.bipm.org/en/bipm-services/timescales/time-ftp/Circular-T.html`.

[171] IERS Bulletin C (leap second announcements). `https://datacenter.iers.org/data/latestVersion/16_BULLETIN_C16.txt`.

[172] G. Petit. A new realisation of terrestrial time. *Proc. 35th Precise Time and Interval (PTTI) Meeting*, pages 307–316, 2003.

[173] P. Wolf, G. Petit, E. Peik, C. Tamm, H. Schnatz, B. Lipphardt, S. Weyers, R. Wynands, J-Y. Richard, S. Bize, F. Chapelet, F. Pereira dos Santos, and A. Clairon. Comparing high accuracy frequency standards via TAI. In *Proceedings of the 20th European Frequency and Time Forum*, pages 476–485, 2006.

[174] C. E. Shannon. Communication in the presence of noise. *Proceedings of the IRE*, 37(1):10–21, 1949.

[175] C. Grebing, A. Al-Masoudi, S. Dörscher, S. Häfner, V. Gerginov, S. Weyers, B. Lipphardt, F. Riehle, U. Sterr, and C. Lisdat. Realization of a timescale with an accurate optical lattice clock. *Optica*, 3(6):563–569, Jun 2016.

[176] G. Panfilo and T. E. Parker. A theoretical and experimental analysis of frequency transfer uncertainty, including frequency transfer into TAI. *Metrologia*, 47(5):552–560, 2010.

[177] J. Azoubib, M. Granveaud, and B. Guinot. Estimation of the scale unit duration of time scales. *Metrologia*, 13(3):87–93, 1977.

[178] Mean fractional deviation of the TAI scale interval from that of TT. `https://webtai.bipm.org/ftp/pub/tai/other-products/sitai/sitai2020.pdf`. Accessed: 2021-09-07.

[179] Relationship between EAL and TAI. `https://webtai.bipm.org/ftp/pub/tai/other-products/ealtai/feal-ftai`. Accessed: 2021-09-07.

[180] G. Petit, A. Kanj, S. Loyer, J. Delporte, F. Mercier, and F. Perosanz. 1×10^{-16} frequency transfer by GPS PPP with integer ambiguity resolution. *Metrologia*, 52(2):301–309, Mar 2015.

[181] C. F. A. Baynham, E. A. Curtis, R. M. Godun, J. M. Jones, P. B. R. Nisbet-Jones, P. E. G. Baird, K. Bongs, P. Gill, T. Fordell, T. Hieta, T. Lindvall, M. T. Spidell, and J. H. Lehman. Measurement of differential polarizabilities at a mid-infrared wavelength in $^{171}\mathrm{Yb}^{+}$. *arXiv*, 2018.

[182] N. Huntemann, M. Okhapkin, B. Lipphardt, S. Weyers, Chr. Tamm, and E. Peik. High-accuracy optical clock based on the octupole transition in $^{171}\mathrm{Yb}^{+}$. *Phys. Rev. Lett.*, 108:090801, 2012.

[183] S. A. King, R. M. Godun, S. A. Webster, H. S. Margolis, L. A. M. Johnson, K. Szymaniec, P. E. G. Baird, and P. Gill. Absolute frequency measurement of the $^{2}\mathrm{S}_{1/2} -^{2}\mathrm{F}_{7/2}$ electric octupole transition in a single ion of $^{171}\mathrm{Yb}^{+}$ with 10^{-15} fractional uncertainty. *New Journal of Physics*, 14(1):013045, 2012.